TWO-PROTON AND TWO-NEUTRON CORRELATION FUNCTIONS IN INTERMEDIATE-ENERGY HEAVY-ION REACTIONS

By

Sally Janine Gaff

A DISSERTATION

Submitted to
Michigan State University
in partial fulfillment of the requirements
for the degree of

DOCTOR OF PHILOSOPHY

Department of Physics and Astronomy

1997

ABSTRACT

TWO-PROTON AND TWO-NEUTRON CORRELATION FUNCTIONS FOR INTERMEDIATE-ENERGY HEAVY-ION REACTIONS

By

Sally Janine Gaff

Two-particle intensity interferometry is used to study the space-time characteristics of the reaction zone formed in intermediate-energy heavy ion reactions. The results are compared to appropriate models.

Because of the recently reported discrepancies between BUU calculations and measured two-proton correlation functions at beam energies E/A>100 MeV, a two-proton correlation function has been measured for the reaction $^{16}O + ^{197}Au$ at E/A=200 MeV. The measured total correlation function agrees with the BUU predictions, but the dependence of the correlation function on the total momentum predicted by the BUU model is larger than the data show.

In the evaporative regime, questions arise in interpreting charged particle correlations because of the Coulomb field of the heavy residue. Therefore, in this energy region two-neutron correlation functions were measured. Two-neutron correlation functions for the reaction $^{40}Ar + ^{165}Ho$ at E/A=25 MeV are presented and comparisons made to models. Corrections and event selection are made for the coincident neutrons to eliminate the effects of crosstalk and background scattering. These corrections are compared to two independent simulations. The experimental results show a strong

correlation at q = 0, which is comparable to emission from the surface of a sphere with a radius of 7 fm and an exponential lifetime of 700 fm/c. An evaporative model with and without preequilibrium corrections was compared to the data. The measured lifetime is within a factor of two of the lifetime the evaporative model predicts. This comparison provides a useful test of the statistical models used for fission lifetime measurements.

To the glory of God

ACKNOWLEDGMENTS

I would first like to thank my research advisor, Konrad Gelbke. He has provided invaluable guidance and motivation. Every time I talked to him my work seemed more valuable and more interesting.

I would also like to thank the members of my guidance committee: Aaron Galonsky for many conversations about the Neutron Walls, Wolfgang Bauer for running BUU calculations for me, and Bernard Pope and S.D. Mahanti for their input and for adding breadth to the committee.

Other professors at the Cyclotron have provided helpful information and ideas about my research and what it means to be a research scientist. I would like to mention Thomas Glasmacher, Betty Tsang, Bill Lynch, Ed Kashy, Sam Austin, Mike Thoennessen, Dave Morrissey, and Paul Mantica. I especially want to thank Scott Pratt for explaining the finer points of correlation functions.

The people whose hard work made the two experiments included in this thesis possible deserves special recognition. The two-proton experiment involved T. Glasmacher, E. Gualtieri, D.O. Handzy, S. Hannuschke, R. Lacey, L. Martin, C.P. Montoya, R. Pak, N. Stone, A.M. Vandermolen, G.D. Westfall, and J. Yee along with theoretical help from W. Bauer, F. Daffin, and K. Haglin. The two-neutron experiment involved A. Galonsky, C.K. Gelbke, T. Glasmacher, M.J. Huang, J. Kruse, G.J. Kunde,

R. Lemmon, W.J. Lynch, S. Pratt, M.B. Tsang, J. Wang, P. Zecher, F. Deak, A. Kiss, A. Horvath, Z. Seres, K. Ieki, and Y. Iwata.

Many students at the Cyclotron have been good friends. I would like to thank my officemates who kept my life interesting: Mathias who was always interested in my newest car adventures and was willing to help even though my car never broke in the ordinary ways, Mike for his attempts to help me see how bad life really is and his ever helpful critiques of my data, Jing for helping me with Neutron Wall questions, Don who provided stories for my file, and also David for reminding me what it is like to start graduate school. I would also like to thank Raman Pfaff, Chris Powell, Jac Caggiano, Jon Kruse, Phil Zecher, Damain Handzy, Dave Brown, Gerd Kortemeyer, and Bettina Huebner for various interesting conversations in the office, at conferences and at the Peanut Barrel. I would especially like to thank Njema Frazier for being a great roommate and for being around when I was sick of talking about cars and football.

Other people at the Cyclotron were essential in my finishing this dissertation. Gerd Kunde provided a lot of assistance in analysis and with PAW questions. Razvan Popescu was also helpful in answering PAW questions and making the research group meetings more interesting. I would like to thank Rich for help with technical questions and organizing breakfasts. I am also indebted to Craig Snow and Christine O'Conner and the rest of the staff at the Cycltron. I also appreciate being included as a LOL.

I would also like to thank those who helped with the actual preparation of my thesis. This help includes the writing group, initiated by Betty Tsang, organized by

Sharon Thomas, with participants Kim Kessler, Ray and Xi. I especially want to thank Amy Hirshman for reading the whole manuscript and finding many grammar mistakes.

I want to thank my other friends who made my stay at Michigan State University more fun, including friends from University Reformed Church and Graduate InterVarsity. If I started to list them all, I would need to add many more pages to these acknowledgments. I thank them all.

My family deserves special thanks for their support. My Mom and Dad for thinking graduate school is a worthwhile thing to do. And my sister for her confidence in me expressed in her frequent question, " Did you fail out of grad school yet?" I also thank her for taking a little longer to finish so my little sister would not graduate before me.

Last I would like to thank Misha for his input on both my thesis and my practice talks. His friendship made my life much better during these last few stressful months.

TABLE OF CONTENTS

LIST OF TABLES

LIST OF FIGURES

Chapter 1 - Introduction

1 .1 Intermediate-Energy Heavy-Ion Collisions

Since the beginning of this century, understanding the atom, which is the basic building block of matter, has been a topic of interest. In 1906, Rutherford began a series of experiments which showed that most of the atomic mass is found in a nucleus which fills only 10^{-15} of the atom's volume. Since this experiment, other scientists have been trying to understand the nucleus and the forces that hold it together.

With the advent of modern accelerators, it is now possible to study nuclear matter in conditions, such as extreme temperatures and densities, that do not occur in ordinary terrestrial settings but may exist in the cosmos, e.g., in supernovae explosions or neutron stars. Current heavy-ion accelerators probe a broad range of nuclear properties including high-spin states, high excitation energy, and unusual isospin configurations. By varying the initial collision conditions, different aspects of the nuclear interactions can be explored. As an example, with different bombarding energies collisions are produced which are sensitive to different properties of the nucleus.

At low bombarding energies (E/A $\leq$ 10 MeV), the collision is dominated by mean field effects and one-body dissipation. The colliding nuclei can form a long-lived equilibrated source which decays statistically over a long time (100,000 fm/c = 3×10^{-19} sec). Often these reactions are modeled by assuming fusion of the two nuclei and total equilibration of the energy among the nucleons. In this model, particles are then emitted

statistically over a long lifetime. Topics that can be studied at low energies include nuclear rotation, particle evaporation, fission mechanisms and the viscosity of the nucleus.

At relativistic energies (E/A $\geq$ 1 GeV), the individual nucleon-nucleon interactions become dominant. These systems form and decay in a short period of time (10 fm/c), and the nucleus-nucleus collision is often pictured with a fireball model, where the energy deposited in the overlap between projectile and target is equilibrated and released in an explosive expansion. The particles are produced and emitted on a very short time scale (less than a few tens of fm/c). One topic studied in the ultrarelativistic energy range is under what conditions nucleons are merged to form a plasma of the constituent quarks and gluons.

Another important region for understanding the reaction dynamics of nuclear collisions is the intermediate energy region. In this region both the mean field and the individual nucleon-nucleon interactions determine the dynamics, so several processes can occur. A heavy residue can be formed after emission of initial particles, or the composite source can fragment into many small clusters. Statistical mechanics suggests a description of nuclear matter as having various states: liquid at normal temperatures and pressures, and gas when the nucleus is heated so much that it breaks up into individual nucleons. This phase transition is currently being studied [Naya 92]. In general these studies try to provide an understanding of the equation-of-state of nuclear matter, the relationship of pressure, volume, and temperature.

At all energies, interpretation of nuclear reactions requires understanding the dynamics, size, and time scale of the reaction. The focus in any one experiment is usually on understanding one part of the reaction process by applying a certain technique. For example, information about the space-time characteristics of the source can be obtained by analyzing coincident particles using particle intensity interferometry.

1 .2 Particle Intensity Interferometry

The first interferometer measured the fringe patterns produced when light from a coherent source travels along two different paths and interferes, e.g., the two-slit experiment. The interferometer is sensitive to the differences in phase between the two signals when they reach a detector. In one early interferometry experiment, Michelson tried to measure the earth's motion relative to the ether with an improved interferometer, and his null result provided evidence of wave propagation without the ether. Since that interferometry measurement, many improvements and applications have been made for interferometers.

One astronomy application uses an interferometer to measure star diameters [Hari 85]. The star emits light from points on its surface, as illustrated in Figure 1.1a. The photons from points S1 and S2 pass through slits at P1 and P2, and interfere either constructively or destructively at the detector. The visibility of an interference pattern, or coherence, can be shown to depend on the angular diameter, 2α, of the star [Stee 83]. If the first zero of the interference pattern is found, it can be translated into angular diameter

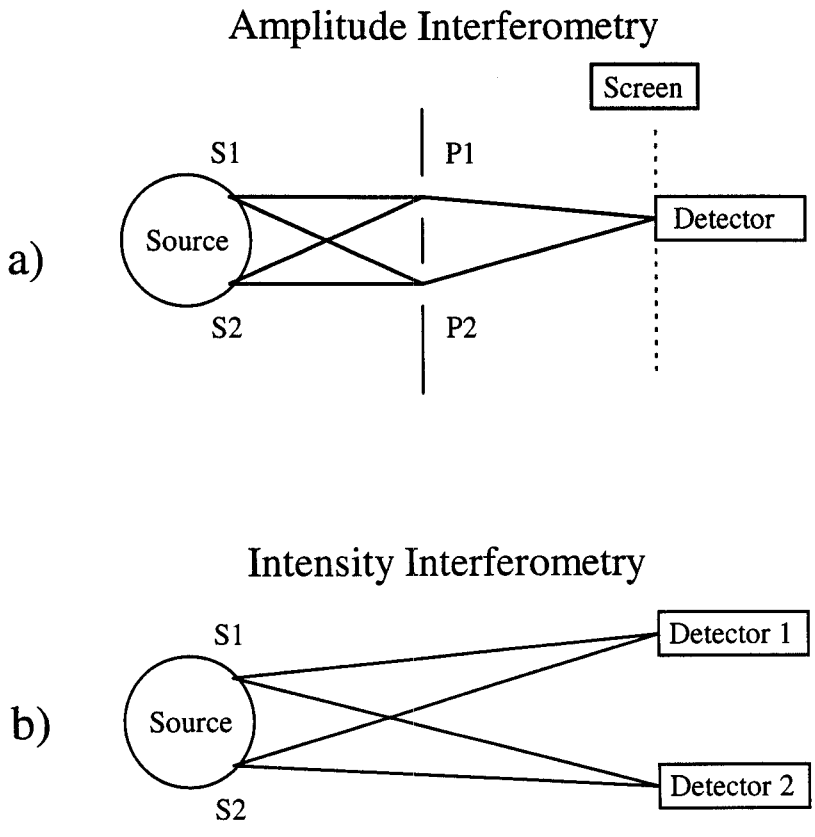

Figure 1.1. Comparison of amplitude and intensity interferometry. a) An amplitude interferometer measures light intensity after the interference of two signals from a source. b) An intensity interferometer measures single and coincident yields from a single source.

by the formula: $2\alpha = 1.22\frac{\lambda}{s}$, where s is the separation of the detectors, and λ is the wavelength. Only a few stars with large angular extent can be measured by this technique. To increase the resolving power, signals must be selected by slits that are further apart. As the slits are moved further apart, differences in the paths caused by mechanical instability and atmospheric fluctuations become important and can destroy the signal. These limitations in amplitude interferometry inspired the development of a new technique.

In the mid fifties, Hanbury-Brown and Twiss introduced intensity interferometry to overcome these limitations in measuring star diameters [Hanb 56]. Instead of measuring fringes of light and darkness caused by relative phase differences, the intensities of light at two points are compared. In Figure 1.1b intensity interferometry is illustrated by a source emitting particles from S1 and S2. The yields at the detectors, n_1, n_2, and the coincidence yield, n_{12}, are measured, and the correlation function is constructed by the relation: $C(\vec{p}_1, \vec{p}_2) = 1 + R(\vec{p}_1, \vec{p}_2) = \frac{\langle n_{12} \rangle}{\langle n_1 \rangle \langle n_2 \rangle}$. The coincident yields averaged over some time are compared for photons measured simultaneously and for photons measured at different times. Because the photon's wave function is symmetrized, the coincidence yield is enhanced compared to that for photons with non-overlapping wave-packets.

Within a few years, applications of intensity interferometry extended beyond astronomy to nuclear physics. In nuclear physics, interferometry has been applied to

studying the size characteristics of the reaction region. While the astronomy experiments detected photons, in nuclear physics many other particles can be detected, and correlation functions can be constructed with all of these particles. With particles the interactions include not only quantum statistics but also nuclear or Coulomb forces. The first nuclear results were published by Goldhaber, Goldhaber, Lee and Pais, who applied this technique to study pion correlations in proton-antiproton annihilation at 1 GeV [Gold 59, Gold 60]. Since that experiment, many other nuclear systems have been studied with intensity interferometry. In this dissertation two proton and two neutron coincidence measurements will be used to construct correlation functions.

1.3 Motivation

1.3.1 Two-Proton Intensity Interferometry

Two-proton correlations have been studied extensively at intermediate energies [Lync 83, Poch 86, Chen 87, Awes 88, Gong 90, 91a, 91b, Lisa 93, Hand 95b]. These studies have shown that the correlation function depends on other reaction variables such as the total energy of the proton pair and the impact parameter, or overlap, in the collision. By comparing these results to simple geometric models, progress has been made in understanding the evolution of the source. For example, changes in the correlation function with total energy may be attributed to cooling effects from particle emission, and changes with the impact parameter reflect different geometries of the reaction zone [Lisa 93].

Because the actual time evolution is expected to be more intricate, experimental results have been compared with transport models which include reaction dynamics. Calculations with the Boltzmann-Uehling-Uhlenbeck (BUU) transport equations have been rather successful in reproducing inclusive two-proton correlation functions at beam energies below approximately E/A ≈ 100 MeV with reactions such as $^{14}N + ^{27}Al$ and $^{14}N + ^{197}Au$ at E/A = 75 MeV [Gong 90b, 91a, 91b]. At higher energies (200A MeV), Kunde et al. found that the BUU model significantly overpredicted the correlation function for the $^{40}Ar + ^{197}Au$ reaction [Kund 93]. A similar over prediction in the proton correlation function was seen for the reaction $^{36}Ar + ^{45}Sc$ at E/A = 120 and 160 MeV [Hand 95b, 95c], but not at E/A = 80 MeV [Lisa 93]

In order to further investigate correlation functions in this energy domain, the reaction $^{16}O + ^{197}Au$ at E/A = 200 MeV was studied. The results of this investigation are described in the second chapter of this thesis.

1 .3 .2 Two-Neutron Intensity Interferometry

To complement the information available from two-proton correlation functions, two-neutron correlation functions can also be measured. Two-neutron correlation functions are especially useful for avoiding final-state Coulomb interactions with the residual nucleus and the resulting distortion of the correlation function. These distortions should be largest in the case of evaporation from a compound nucleus. An experimental study of the reaction $^{129}Xe + ^{27}Al$ at E/A = 31 MeV found that the direction-selected correlation functions (directional cuts are discussed in Section 4.1) were best fit using a

hard sphere of radius r = 3.5 fm and an exponential lifetime τ = 1300 fm/c [Lisa 94]. This source size is much smaller than the geometric compound nucleus size ($r = 1.2\ A^{1/3} = 6.5$ fm). This discrepancy is difficult to understand, unless one allows that the heavy residue is distorting the outgoing particle trajectories and thus the correlation function. When interpreting correlation functions, one usually assumes that the particles being studied only interact with each other and not with the rest of the system. This assumption fails when measuring charged particles, especially when they move slowly away from the emitting heavy residue. The Coulomb forces may distort the proton correlation function and thus must be considered when interpreting the two-proton correlation functions [Gong 92]. Unfortunately, the three-body problem has not been solved exactly for this quantum-mechanical system. Experimentally it is possible to eliminate this Coulomb force by constructing a correlation function using neutrons.

Two-neutron correlation functions have not been extensively measured because of the challenges involved in measuring coincident neutrons [Ghet 93, Colo 95]. Neutrons are scattered both by the detectors and by other materials in the experimental area. They do not stop in a detector, so the same neutron can be measured in two detectors and make a false coincidence. Also, many neutrons can be scattered into the detector after they have interacted with other material, such as the walls of the vacuum chamber, or the concrete floor or ceiling. These background neutrons can come in coincidence with a direct neutron and distort the correlation function. Corrections for these effects must be made before the correlation function can be interpreted.

To measure a two-neutron correlation function for a compound nucleus formed in a low-energy reaction, the system $^{40}Ar + ^{165}Ho$ at E/A = 25 MeV was chosen. Lifetimes for these low energy evaporation reactions are important, since neutron evaporation "clocks" have been used to obtain information about the time-scale of nuclear fission [Hind 84]. Two-neutron correlation functions can provide a calibration for these "clocks." This system was chosen because it has a high neutron multiplicity [Schw 94], and since many neutrons are emitted from the system, the chance of measuring two within a limited angular range is enhanced. Also, a similar system was measured to have a significant compound-nucleus cross section with most neutrons emitted after equilibrium had been reached [Benr 93].

The second experiment discussed in this thesis involves neutron-neutron correlation functions for the reaction $^{40}Ar + ^{165}Ho$ at E/A = 25 MeV. This experiment was designed to measure the two-neutron correlation function which contains information about the source size and lifetime of an evaporative collision. The results of this experiment are described in Chapters 3-6

Chapter 2 - Two-Proton Intensity Interferometry: ^{16}O + ^{197}Au at E/A=200 MeV

2.1 Motivation

Calculations with the Boltzmann-Uehling-Uhlenbeck (BUU) transport equation have been rather successful in reproducing inclusive two-proton correlation functions at E/A ≤ 100 MeV [Gong 90b, 91a, 91b, Lisa 93, Hand 95b]. At higher energies, the BUU model was expected to be more appropriate. The model includes approximations, representing the Pauli blocking, which should become more accurate at higher energies where more states are available and the time scale becomes shorter. Therefore, it was surprising that BUU calculations failed to reproduce the results from the ^{40}Ar + ^{197}Au reaction at E/A = 200 MeV [Kund 93]. These results differed from lower-energy data in at least two ways. First, the data showed an unusually small dependence of the measured correlation function on the energy of the emitted protons, much in contrast to the strong dependence observed at lower energies [Lync 83, Chen, 87, Awes 88, Gong 90b, 91b, Lisa 93]. Second, the data did not show the expected minimum at q ≈ 0 MeV/c (Figure 2.1). These rather surprising results left questions about the generality of the BUU failure and a need to verify the anomalous shape of the observed correlation function.

In this chapter, the results of two-proton correlation measurements for ^{16}O + ^{197}Au collisions at E/A = 200 MeV are presented [Gaff 95]. These measurements were

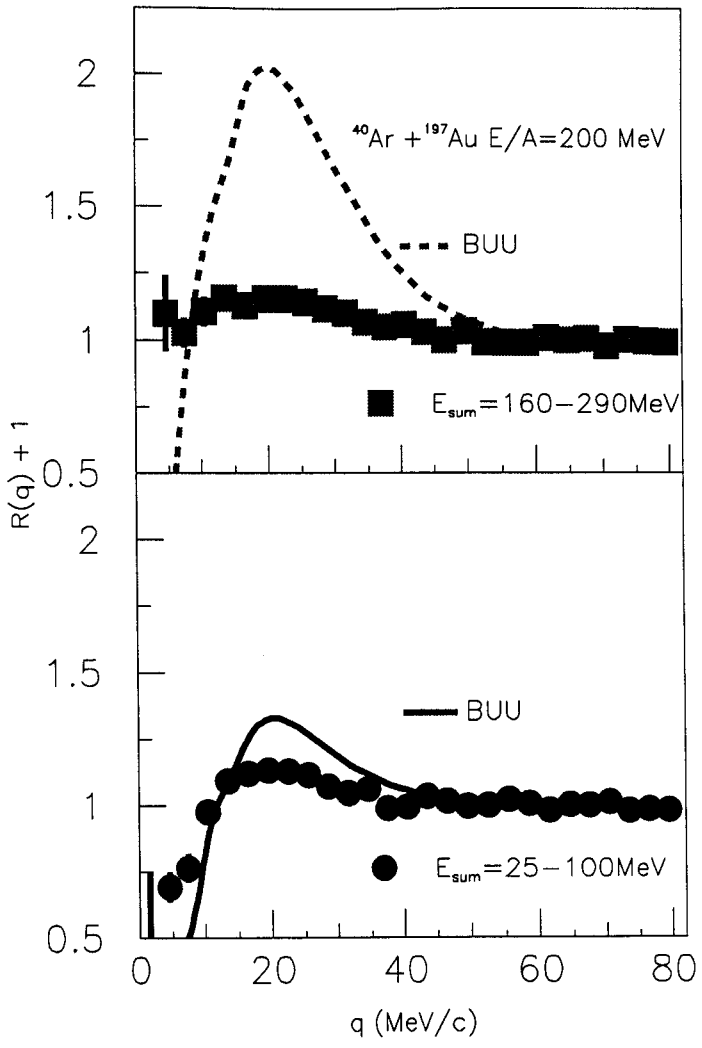

Figure 2.1 Proton correlation function for ^{40}Ar + ^{197}Au reaction at E/A = 200 MeV [Kund 93].

performed to explore whether the anomalous trends observed for the ^{40}Ar + ^{197}Au reaction at E/A = 200 MeV [Kund 93] persist for a lighter projectile.

2.2 Setup

The experiment was performed at the National Superconducting Cyclotron Laboratory using a beam of ^{16}O ions at E/A = 200 MeV, the highest energy per nucleon possible from the K1200 cyclotron. The ^{197}Au target had an areal density of 60 mg/cm^2, and the typical beam intensity was $1.5x10^8$ particles/sec. Coincident protons were detected by a 56-element high-resolution hodoscope [Gong 88, Gong 90a] attached to the MSU 4π Array [West 85] at $\langle \theta_{lab} \rangle = 38°$ (Figure 2.2). Each element of the hodoscope consisted of a 300 or 400 μm-thick Si detector backed by a 10 cm-long CsI(Tl) detector, allowing measurement of protons with energies between 10 and 200 MeV. The telescopes each subtended a solid angle of $\Delta\Omega \approx 0.37$ msr. The nearest-neighbor spacing between telescopes was $\Delta\Theta = 2.6°$, and the energy resolution for each telescope was about 1% for 50 MeV protons. Events were written on tape when they satisfied the trigger condition of at least two detectors of the 56-element hodoscope and at least three detectors of the 4π-Array firing. This trigger eliminated the most peripheral collisions, but otherwise accepted a broad range of impact parameters. Due to a major power outage, the experiment had to be ended prematurely, and the statistics collected were insufficient to allow narrow cuts on impact parameter. Thus we can only present inclusive two-proton correlation functions.

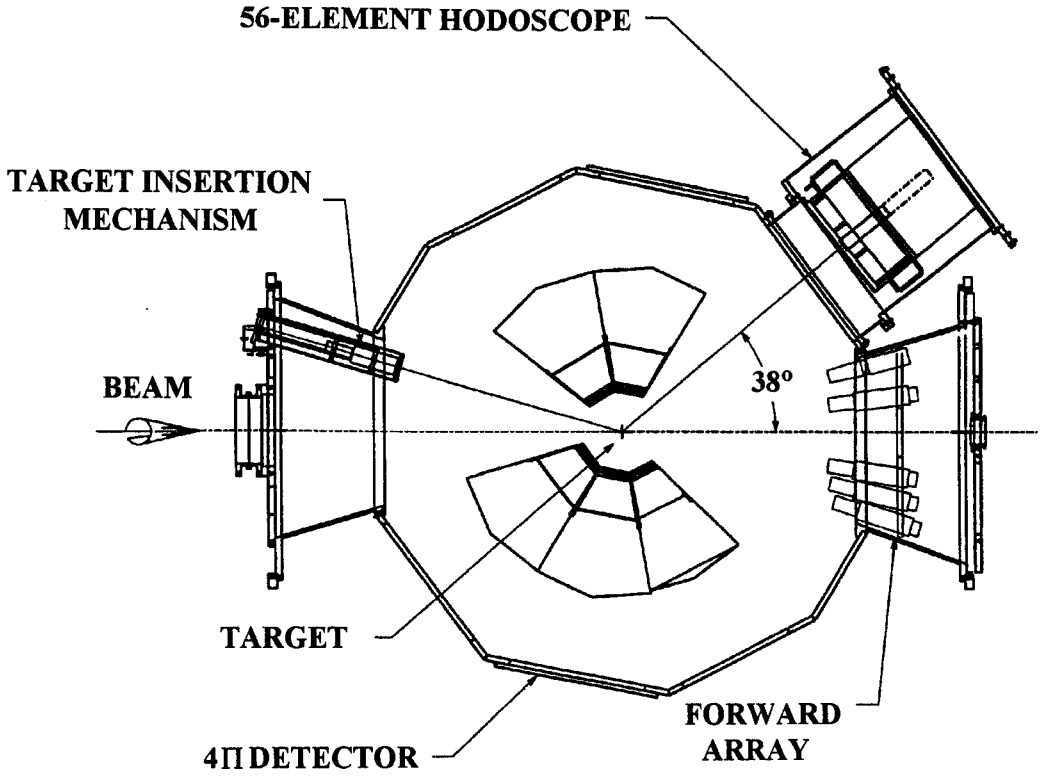

Figure 2.2 Schematic drawing of the experimental setup: the 56-element hodoscope attached to the MSU 4π array.

2.3 Results

The solid points in Figure 2.3 show the measured energy spectrum of protons emitted at polar angles θ_{lab} = 30° - 45°. The solid curve represents the corresponding energy spectrum predicted by the BUU calculations [Baue 87, 92, Li 91a, 91b]. In these calculations, a hard equation of state (K = 380 MeV) and an in-medium nucleon-nucleon cross section set to its free value were used. The calculations were filtered for the experimental acceptance and energy thresholds. A proton was considered emitted if it was located in a region of local mass density less than one-eighth normal nuclear density [Gong 91a, 91b]. At energies near the Coulomb barrier BUU calculations overpredict the proton yield. Such an overprediction of the proton yields at low energies has been noted previously and attributed to the neglect of light cluster formation [Hand 95b, 95c, Gong 93]. Light clusters are expected to be predominantly formed in densely-populated regions of phase space, thus reducing the flux of free nucleons at low energies.

In order to investigate the influence of light cluster production on the calculated two-proton correlation functions, the single-particle phase-space distribution of emitted particles was subjected to a coalescence analysis. When adjusting the coalescence parameters to the observed p/d/t ratio, the calculated singles yield of protons below 50 MeV was reduced by a factor of two relative to the high-energy protons in accordance with naive expectations. Despite this change of energy distribution in the singles spectra, the calculated two-particle correlation functions remained virtually unchanged. (This effect was noted before [Gong 91a, Baue 92] and attributed to the division procedure

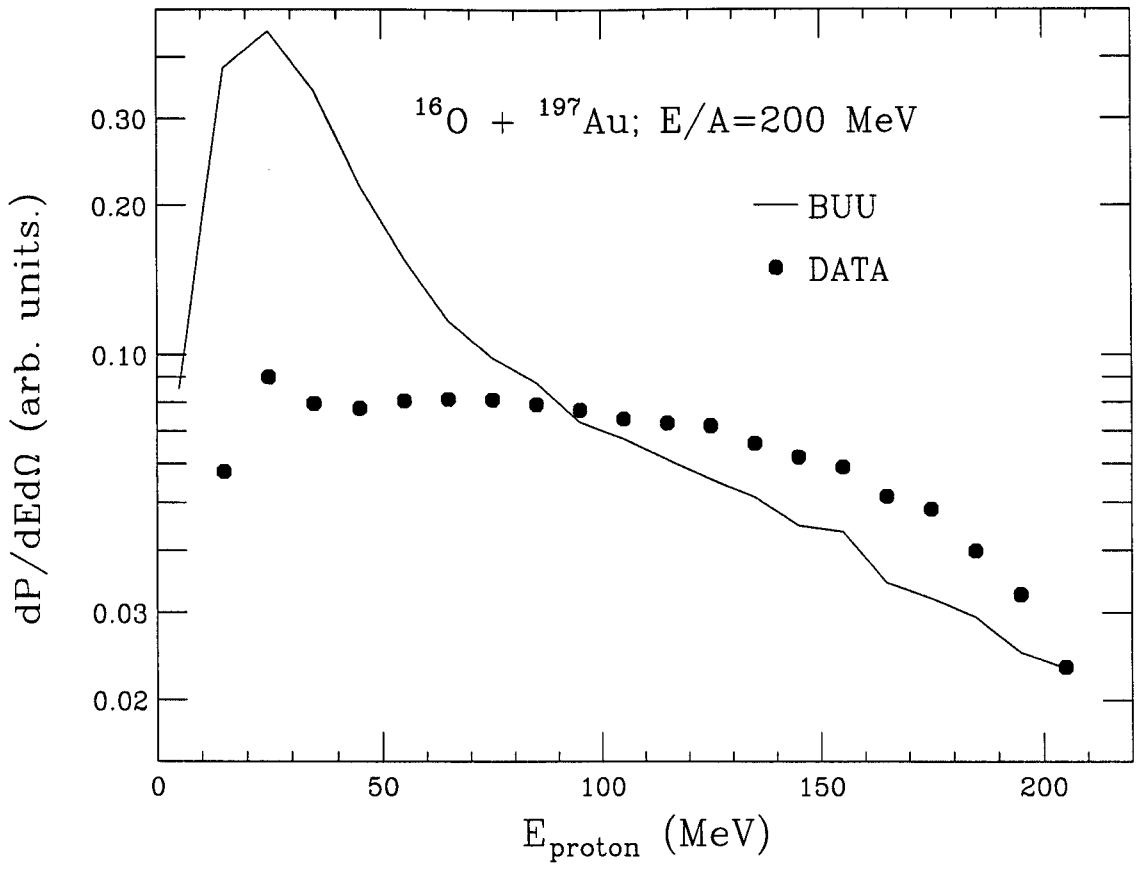

Figure 2.3 Energy distribution of protons measured in the laboratory rest frame at θ_{lab} = 30°- 45° for collisions of ^{16}O + ^{197}Au at E/A = 200 MeV (solid points) and predicted by BUU (solid line). To allow a comparison of shapes, the relative normalization between experimental and theoretical energy spectra was chosen to give equal areas for E_{proton} > 50 MeV.

employed to arrive at the correlation function as a ratio of the two-particle cross section and the square of the singles cross section. Since coalescence changes only the density of particles emitted but does not change the volume into which the particles are emitted, the shape of the correlation function should not change.) Even after the coalescence step, the predicted singles spectra were still somewhat steeper than the data. This is at least partially due to the fact that the coalescence was applied to particles that had been emitted, i.e. that came from a region of low density ($\rho \leq 1/8$), and the cluster formation may be determined at somewhat higher densities. In light of the insensitivity discussed above, the model parameters were not adjusted to produce a perfect fit to the data. Instead the singles spectrum shown is that produced by BUU and not corrected by a coalescence step.

Two-proton correlation functions, 1 + R(q), are presented in Figure 2.4. The experimental two-proton correlation function, shown by points, was defined in terms of the two-proton coincidence yield, $Y_2(p_1, p_2)$, and a background yield, $Y_{back}(p_1, p_2)$, obtained by the event-mixing technique [Lisa 91].

$$\sum Y_2(p_1, p_2) = C[1 + R(q)]\sum Y_{back}(p_1, p_2).$$

Here q is the (invariant) magnitude of the relative momentum four-vector, given non-relativistically as $q = \frac{1}{2}|\vec{p}_1 - \vec{p}_2| = \mu v_{rel}$. For a given experimental gating condition, the sums of each side of the equation above extend over all proton energies and detector combinations of the 56-element hodoscope corresponding to each q-bin. The normalization constant C is determined by the requirement that R(q) vanish for large q,

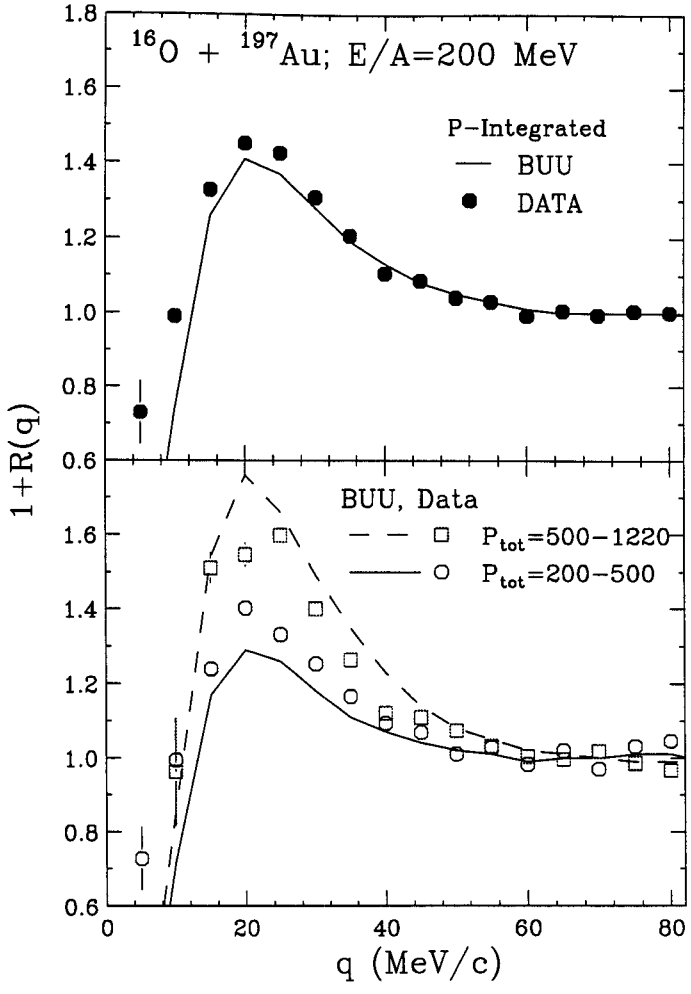

Figure 2.4 Two-proton correlation functions for collisions of ^{16}O + ^{197}Au at E/A = 200 MeV. The top panel shows the energy-integrated correlation function, and the bottom panel shows correlation functions for proton pairs selected by the indicated cuts on their total momentum.

where final-state interactions between the emitted protons are negligible. Specifically, both the experimental and theoretical correlation functions were normalized such that $\langle R(q) \rangle = 0$ for 60 MeV/c $\leq q \leq$ 80 MeV/c.

Theoretical two-proton correlation functions (shown by curves in Figure 2.4) were calculated with the Koonin-Pratt formalism which relates the one-body phase-space distribution with the correlation function [Koon 77, Prat 87, Gong 91a, 91b]. Specifically, the theoretical correlation function was calculated by convoluting the one-body phase-space distribution predicted by the BUU calculations described above with the two-proton relative wave function [Gong 91a, 91b].

The upper panel of Figure 2.4 presents the energy-integrated correlation function for all protons detected by the 56-element hodoscope with laboratory energy above 10 MeV and below 200 MeV. The lower panel shows correlation functions selected by two different cuts on $P_{tot} = |\vec{p}_1 - \vec{p}_2|$, the total momentum of the detected proton pair in the center-of-momentum frame of projectile and target. The peak values, $1 + R_{max} \approx 1.4 - 1.6$, of the measured correlation functions are larger than the values, $1 + R_{max} \approx 1.2$, reported for the $^{40}Ar + ^{197}Au$ reaction at E/A = 200 MeV [Kund 93]. Further, the magnitude of the correlation function for the present reaction exhibits a clear dependence on total momentum, P_{tot}, of the detected proton pair as compared to the negligible dependence on proton energy observed for the Ar-induced reaction [Kund 93]. Within the resolution of the present experiment, no evidence for a disappearance of the minimum at q = 0 was found.

The BUU calculations reproduce the magnitude of the energy-integrated correlation function (Figure 2.4 upper panel), but they predict too strong a dependence on the total momentum, P_{tot} (Figure 2.4 lower panel). The calculations underpredict the magnitude of the correlation functions measured for the low-momentum gate, 200 MeV/c $\leq P_{tot} \leq$ 500 MeV/c, and they overpredict it for the high-momentum gate, 500 MeV/c $\leq P_{tot} \leq$ 1220 MeV/c.

A couple of differences may explain why the experimental correlation function for the ^{16}O + ^{197}Au reaction at E/A = 200 MeV differs from the ^{40}Ar + ^{197}Au reaction with the same energy per nucleon [Kund 93]. One difference is in the total energy in the system. Since the oxygen is lighter, the total amount of energy deposited in the system is a factor-of-two smaller, and the reaction might produce a residue not present with a heavier projectile. Another difference in these experiments is the lack of an external centrality filter in the [Kund 93] experiment.

In summary, proton energy spectra and two-proton correlation functions were measured at $\langle\theta_{lab}\rangle = 38°$ for ^{16}O + ^{197}Au collisions at E/A = 200 MeV. The single-particle yield for the low-energy protons has a flat slope that is not reproduced well by the BUU transport model, even with a simple coalescence step added. The momentum-integrated correlation function agrees well with the BUU calculations, and the momentum-gated correlation functions show a dependence on the momentum of the proton pair in both experiment and theory. However, the BUU theory overpredicts the magnitude of the observed energy dependence. The correlation functions look significantly different from

those for the $^{40}Ar + ^{197}Au$ reaction at E/A = 200 MeV [Kund 93] in both total height and momentum dependence.

Chapter 3 - Two-Neutron Intensity Interferometry: Experimental Setup and Data Reduction

In the two-neutron intensity interferometry experiment, the intent was to measure the size and lifetime of a compound source formed in the reaction $^{40}Ar + ^{165}Ho$ at E/A = 25 MeV. During a collision many different types of reactions can occur. Thus, it is important to select a specific type of reaction to simplify the interpretation of the correlation functions. Nuclear reactions are often characterized by an impact parameter, defined as the distance between the centers of the particles perpendicular to the direction of motion, before any interaction. Events with small impact parameters were selected in this reaction. These "central events" are those where most of the beam energy is transferred into internal energy. In these events a few preequilibrium particles may be emitted and then a compound nucleus is expected to form.

The experimental setup was designed to select neutrons from a compound nucleus, both by choosing central events and by minimizing the contributions from preequilibrium neutrons. The detectors, used as a trigger, selected central events while providing the zero time for measuring the neutron time-of-flight. These silicon telescopes triggered the electronics when a charged particle with $Z > 2$ was measured at 30° - 40° in the laboratory, a condition shown to favor compound nucleus formation [Kim 89]. Coincident neutrons were measured in detectors placed at 90° in the center of mass. The coincidence requirement biases the data toward more central collisions, and a neutron detection angle of 90° was chosen to reduce the number of preequilibrium neutrons,

which are preferentially emitted in the forward direction. In this chapter the details of the experimental setup, electronics, and data reduction are described.

3.1 Experimental Setup

3.1.1 Fragment Telescopes

Charged particles, used to trigger the experiment, were measured with silicon ΔE-E telescopes. Each telescope was constructed of two elements, a 75 μm planar Si ΔE-detector and a 5 mm Si(Li) E-detector. To improve the resolution of the Si(Li) detectors, the detectors were cooled to 0° Celsius. Each telescope was covered by a collimator with a diameter of 12.7 mm, assuring that only the active area of the detectors was exposed to particles. Onto these collimators was glued a thin Ta foil to suppress electrons. Thirteen of these telescopes were arranged on two circles around the beam axis with polar angles of 30° and 45° (Figure 3.1), much larger than the grazing angle of 9°. The telescopes were located 15 cm from the target. This distance was chosen to maximize the solid angle coverage, while still providing access to the detectors and space for the mounting ring. The whole assembly was placed inside a vacuum chamber. The chamber has a diameter of 91.4 cm and walls made of steel that is only 3 mm thick, to minimize neutron scattering. The detector mount was located so that it did not shadow any part of the Neutron Walls (Figure 3.2).

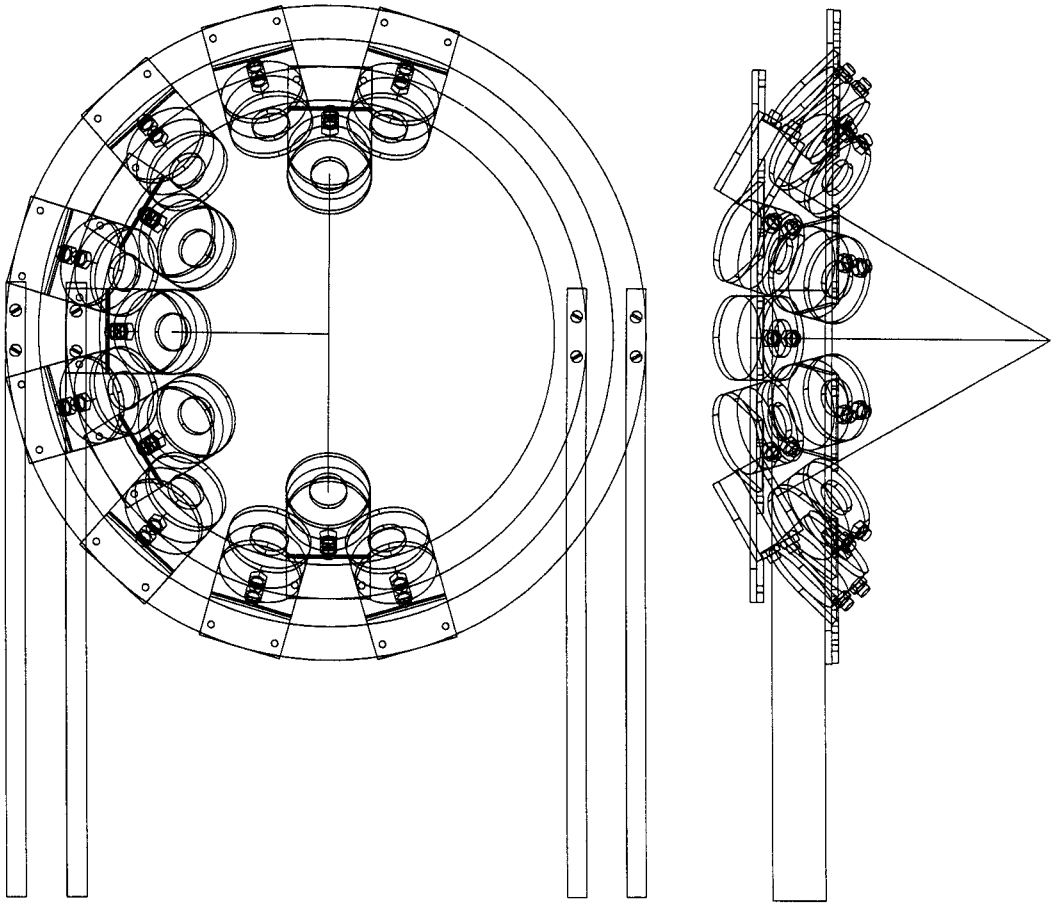

Figure 3.1 Arrangement of silicon telescopes around the target at angles of 30° and 45° and a distance of 15 cm.

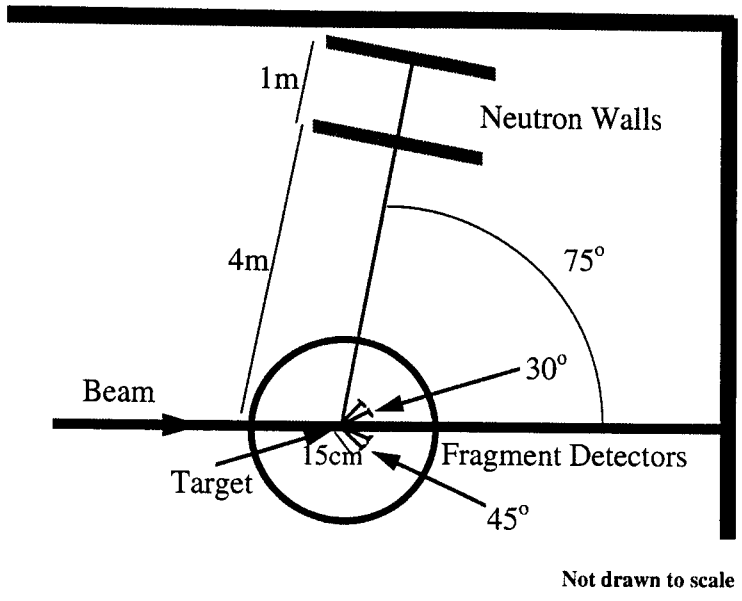

Figure 3.2 Schematic drawing of the setup. The fragment telescopes were used for event selection and the neutron detectors measured coincident neutrons.

3.1.2 Neutron Walls

Neutrons were measured with the Neutron Walls, which were designed and built at the National Superconducting Cyclotron Laboratory (NSCL) [Zech 97]. This detector provides good angular coverage without much dead space. The Neutron Walls are made up of glass cells that are two meters long with a height of 7.62 cm and a depth of 6.35 cm (Figure 3.3). Each cell is filled with NE-213, a liquid scintillator commonly used to detect neutrons. Each end of the rectangular shaped cells was tapered and sealed to a Pyrex circle with a diameter 7.5 cm. On this circular surface a 7.5 cm diameter photomultiplier tube (PMT) is attached with optical epoxy. Each wall is made up of 25 of these cells, of which 24 were used in this experiment (Figure 3.4). The cells are placed as close together as possible and the distance between the centers of adjacent cells is 8.55 cm. The cells are mounted inside an aluminum box which provides mechanical stability and keeps ambient light from reaching the detectors.

During this experiment, the Neutron Walls were positioned at 75° in the laboratory, which corresponds to approximately 90° in the center-of-mass system. The first wall was four meters from the target, and the second wall was placed one meter behind the first (Figure 3.2). Unfortunately, the experiment was performed in an experimental room where the concrete floor and ceiling are about one meter from the detectors. Also, behind the second wall is a concrete wall about 1 meter away. This surrounding concrete scatters neutrons into the detectors.

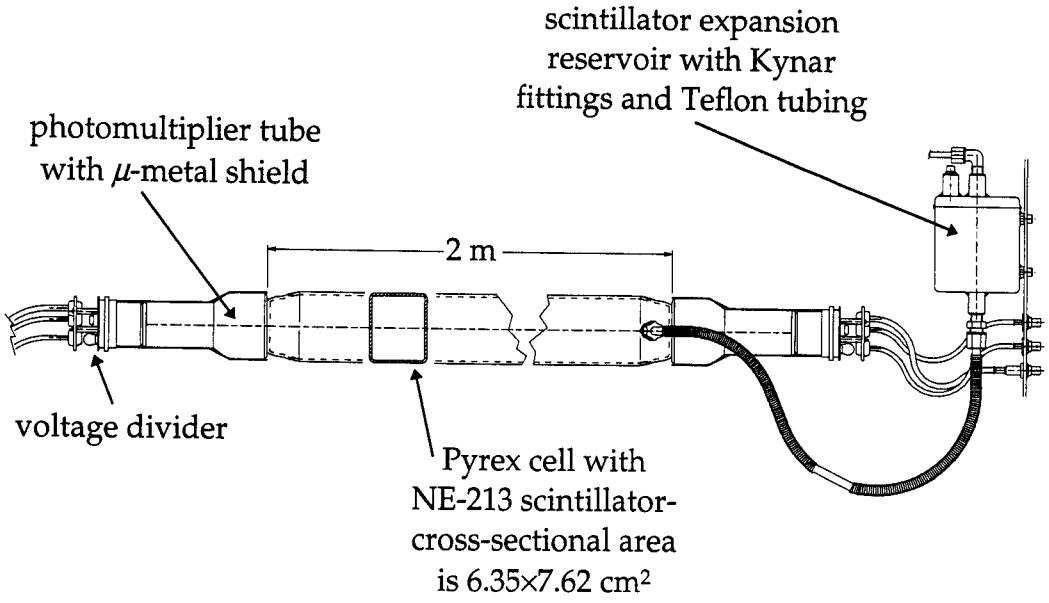

Figure 3.3 Picture of one detector from the Neutron Walls.

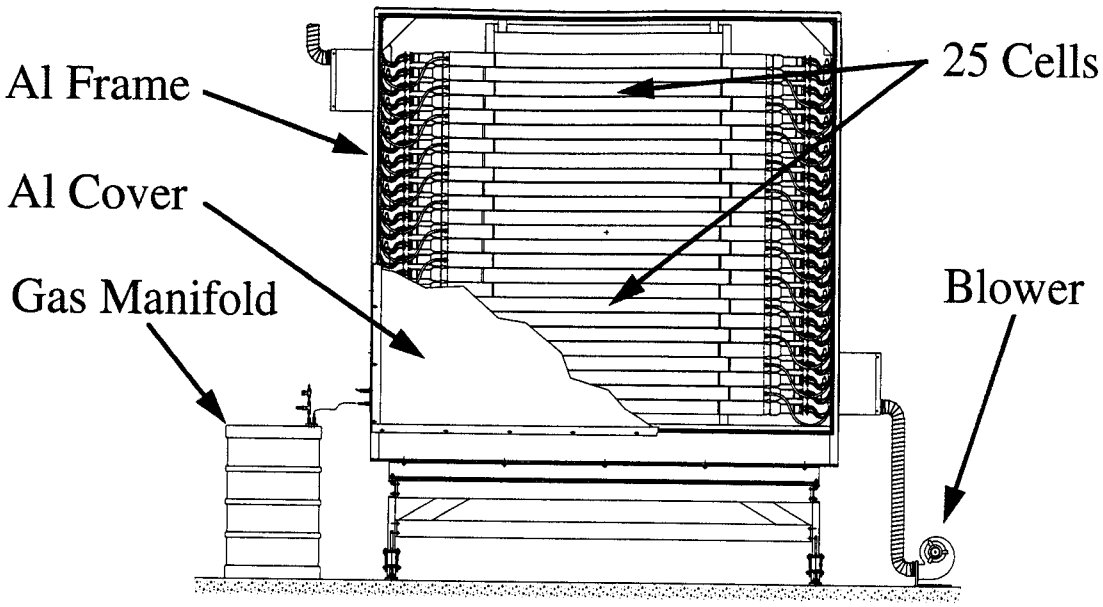

Figure 3.4 Mechanical drawing of one of the Neutron Walls. The glass cells are protected by an aluminum cover, which is sealed to prevent light from reaching the PMTs.

3.1.3 Other Experimental Details

The E/A = 25 MeV ^{40}Ar beam was generated from the K1200 Cyclotron at the NSCL. The beam, with an intensity of approximately $5x10^9$ particles/sec., was delivered to the target. The target was ^{165}Ho, which is naturally mono-isotopic and had an areal density of 32 mg/cm^2. The beam lost E/A = 2.6 MeV in the target [Hube 90], so the interaction energy varied from E/A = 23.4 - 25.0 MeV.

3.2 Electronics

3.2.1 Fragment Telescopes

The two silicon detectors in the telescopes produce signals which can be used to determine the charge, mass, and energy of a particle. The first detector measures energy loss for a specific distance, dE/dx, while the thicker second detector measures the remaining energy, E, of the stopped particle. These two quantities depend on the mass, M, and charge, z, of the particle in the detector, and so a plot of dE/dx, also referred to as ΔE, versus E will show distinct bands for each isotope [Goul 64, Butl 70]. The Bethe-Block describes the energy loss in the form

$$\frac{dE}{dx} = -B\frac{Mz^2}{E}\ln(\frac{CE}{M}),$$

where B and C are constants depending on the detector characteristics [Engl 74].

In order to choose compound nuclei, events were selected where fragments were measured with Z > 2 [Kim 89]. A first cut for heavier fragments was done with hardware.

This cut requires the sum of E and ΔE signals, $x = \Delta E + \alpha E$, to be above a threshold. The threshold and weighting factor, α, were adjusted for each detector, so that most alphas were excluded, but lithium was not (Figure 3.5). The silicon telescope electronics which include this logic are shown in Figure 3.6. The attenuator allows α to be adjusted, and the constant fraction discriminator (CFD) threshold adjusts the minimum x.

The fragment telescopes also provide the zero time for the neutron time-of-flight. A timing pick off (TPO) produces a timing signal from the ΔE signal, which has a faster rise time than the E detector. The TPOs provide quick time signals, but they are prone to oscillations and so require some attention in setup. This signal is delayed with cables by 250 ns and makes the stop for the Neutron Wall timing CFD.

3.2.2 Neutron Walls

Since neutrons do not ionize materials, the most common way to detect them is to measure a recoiling nucleus, which has been scattered by the neutron. Mostly, the Neutron Walls detect neutrons which scatter elastically on protons in a scintillator. These protons excite and ionize the scintillator molecules. The scintillator produces light which propagates by total internal reflection to the photomultiplier tubes (PMTs) where the light signal is detected. If both PMT signals are larger than the threshold of 1 MeV electron equivalent (MeVee) set in the constant fraction discriminators (CFDs), then the event will be recorded.

In the Neutron Walls the phototubes provide two signals, one from the dynode and one from the anode. The signal from the dynode is sent through a CFD and provides

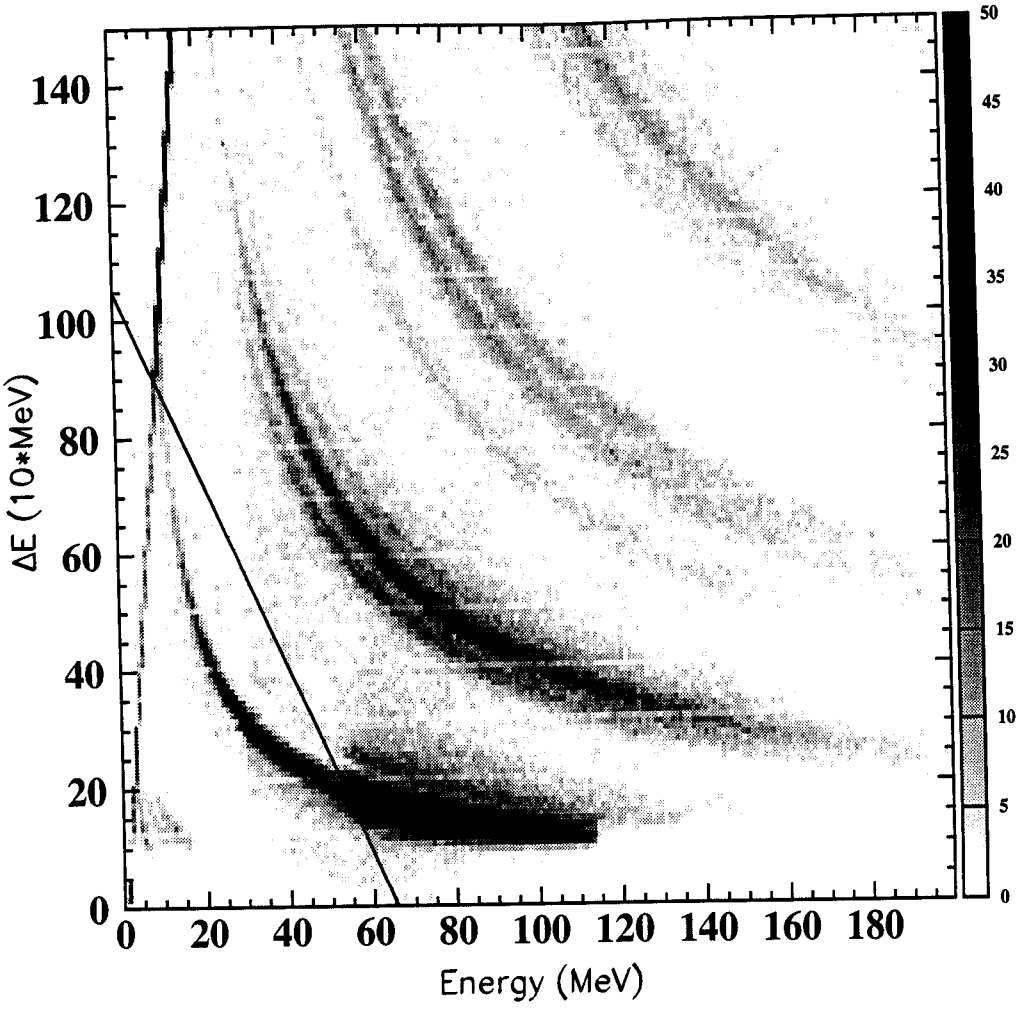

Figure 3.5 E versus ΔE showing the hardware cut. The counts in the lower left corner have been reduced by the hardware trigger. Those remaining come from events triggered by another Si detector. The lack of ^{8}Be gives a useful reference for isotope identification.

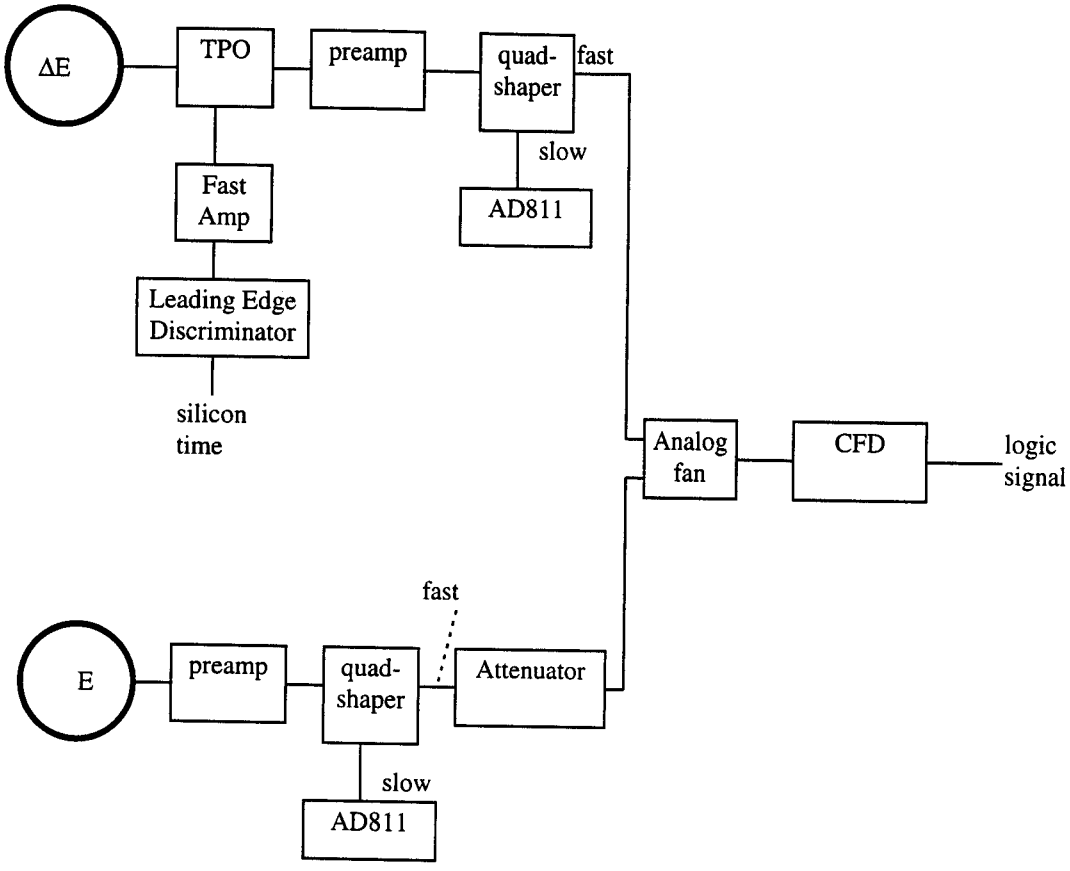

Figure 3.6 Electronics for the Si telescopes. TPO = timing pick off; CFD = constant fraction discriminator; AD811 is a peak-sensing analog-to-digital converter.

logic signals for the circuit. The charge from the anode signal is further processed to provide a measure of the shape and intensity of the light signal.

The time for the neutron time-of-flight is measured by a Time to FERA Converter, TFC. This unit is started by the signal from the CFD and is stopped by the time from the Si telescope, which has been delayed by 250 ns.

These neutron detectors can distinguish gamma rays from neutrons. When ionizing radiation interacts with this organic scintillator, it produces a pulse of light primarily with two components. One component is prompt (decaying in a few nanoseconds) while the other is delayed (decaying over hundreds of nanoseconds). Gamma rays are detected by Compton scattering on electrons. The electrons excite the scintillator and produce light with a mostly prompt fluorescence. On the other hand, neutrons scatter on protons which ionize the scintillator and produce much of their light as delayed fluorescence. The light produces an electric pulse in the PMT, which has the same shape as the light pulse. Because the shape of the electric pulse produced by gammas and neutrons is different, it is possible to compare the shapes of the signals to determine the source of the ionization. Traditionally the comparison was done by using two analog-to-digital converters (ADCs). One ADC measured the total charge produced, and the other measured some fixed fraction of the pulse, for example the first 30 ns. Because this method requires separate gates for each ADC channel and this experiment has almost one hundred channels, an alternate more cost-effective approach was chosen.

The Neutron Walls have a pulse shape discrimination circuit that was designed and built for this detector. This circuit takes the anode pulse and produces four signals:

"Total", "Attenuated Total", "Fast", and "Attenuated Fast". "Fast" is proportional to the charge in the first part of the pulse. The attenuated outputs reduce the signals by approximately a factor of four to give the detectors a wider range. A plot of "Fast" vs. "Total" separates neutrons and gamma rays. During this experiment only enough electronics were available to measure three of the possible signals, and so "Attenuated Fast" was not recorded.

One potential source of error in this experiment is the detection of high energy protons from the reaction in the neutron detectors. Protons produce a light signal exactly like a neutron, and so protons cannot be excluded by pulse shape discrimination. The vacuum chamber, with walls made of 3 mm-thick steel, has a large effect in stopping protons. Using energy loss calculations based on Reference [Hube 90], a proton with energy less than 40 MeV will be stopped by the steel in the chamber wall. Protons up to 57 MeV will be stopped before reaching the scintillator by the additional material present. The protons must pass through 4.0 m of air, the 1/32 inch aluminum box and the 1/8 inch glass cell. Very few protons are expected with energies higher than 57 MeV, thus the effect of protons is not considered in the analysis.

3.2.3 Trigger Electronics

During the experiment three types of events were recorded. The first type of event was the coincidences with at least one hit in the Neutron Wall and a particle with $Z > 2$ in a silicon telescope. The other two event types were downscaled telescope events and downscaled Neutron Wall events. These were singles, where either the Neutron Wall or

the telescope fired alone. Because these events greatly outnumber the coincidence events, they were downscaled and only recorded one time out of 1000. A schematic of the trigger electronics is shown in Figure 3.7. Because the processing time to make the master trigger was over 1 μs, the electronics required a Fast Clear for the Neutron Walls.

3.3 Data Reduction

3.3.1 Fragment Telescopes

The silicon telescopes must identify the isotopes and measure their energy. The energy measured by the silicon detectors, both E and ΔE, was calibrated using an alpha-particle source and a calibrated pulser. A ^{228}Th source was used. It is especially appropriate for the thin silicon detector since it provides an alpha particle with 8.78 MeV which is close to the highest energy measured in the detector. The linearity of the electronics for the full range of each detector was checked by using a pulser. An energy calibration of 10% is adequate to find the particle flight time to within 0.2 ns, but the actual energy calibration is much better (~2%).

Isotopes were identified for each detector after constructing a particle identification (PID) function: $\mathrm{PID} = (E\Delta E)^{1/3} - (0.005)\Delta E$. Figure 3.8 shows the PID resolution for a typical detector. This PID makes setting gates on isotopes easier since instead of the strongly curved gates that would be needed in Figure 3.5, these gates are approximately rectangles. The isotopes were identified based on fixed points, such as ^{6}Li as the lowest Z = 3 isotope and the absence of ^{8}Be, and confirmed by looking at

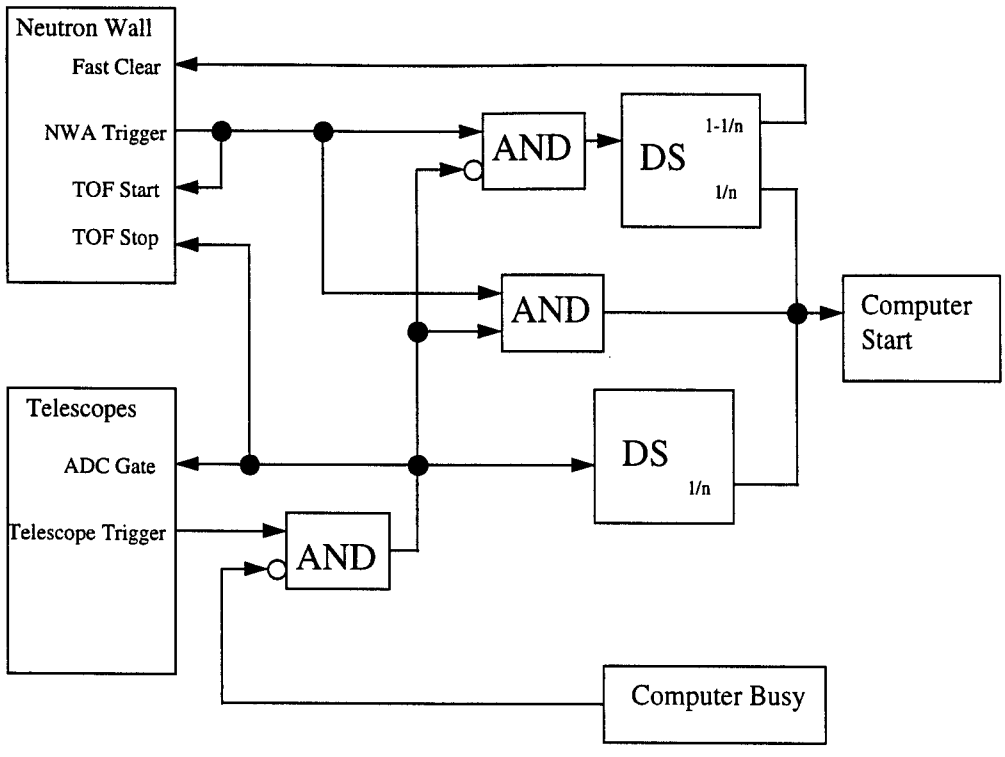

Figure 3.7 Schematic diagram of the trigger electronics from the experiment. The elements marked DS are downscalers.

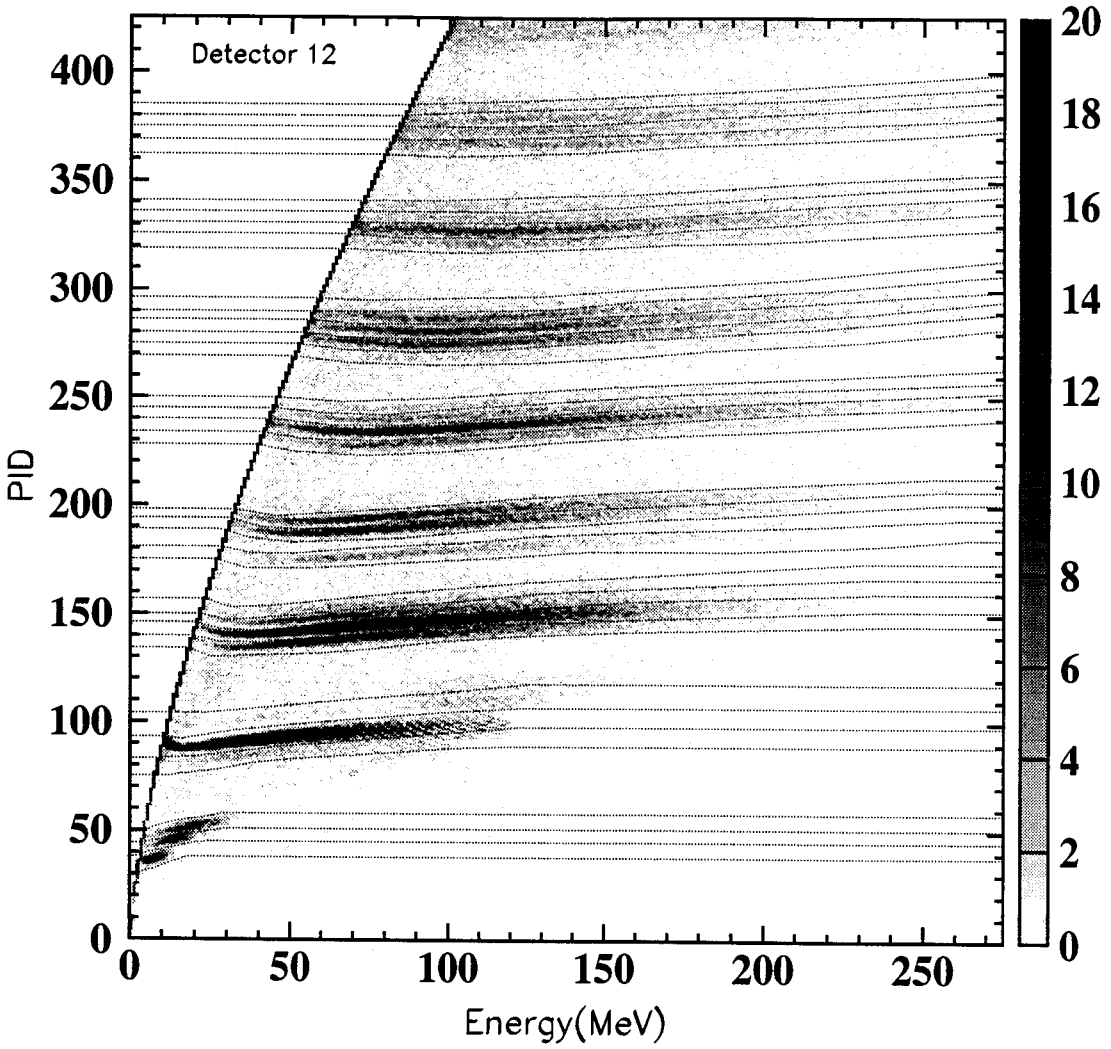

Figure 3.8 PID for silicon telescopes. This plot of energy versus particle identification shows the clear separation between isotopes. The gates are also plotted.

predictions for these detectors using an energy loss program. As expected, the energy threshold increases as a function of mass.

3.3.2 Neutron Walls

For each phototube in the Neutron Walls, a time and light signals were recorded. These signals provide information about the energy, position, particle identification, and amount of light measured for each hit in the detector.

3.3.2.1 Neutron Energy

The neutron energy is determined from the time-of-flight of a neutron between the target and the detector. The time that is measured for each PMT corresponds to the time between the silicon detector trigger and the PMT trigger. This measured time must be corrected in order to find the actual time-of-flight.

The time signals, T_L and T_R, are measured in the experiment by the TFCs which start with the CFD signal for the left or right PMTs and stop with the delayed silicon telescope trigger. This raw time was calibrated with a time calibrator which gives start and stop signals at given time intervals. The signals for the left and right times are then averaged to remove the position dependence, $T_n = (T_L + T_R)/2$. T_n is proportional to the time between a hit in the Neutron Walls and the silicon detector trigger. Because the Neutron Wall starts the time, a smaller T_n corresponds to later times.

In order to find the time-of-flight, TOF, several corrections must be made to the measured time. Specifically TOF is defined as

$$TOF = - T_n + T_{Si} + \Delta T_c.$$

The measured time, T_n, determines the relative time between various signals. In order to find an absolute time a reference time is used. The prompt gammas provide this reference. In the case of prompt gammas

$$TOF = T_\gamma = \sqrt{(d^2 + x^2 + y^2)} / c,$$

where d is the distance to the wall, 4 or 5 meters, x and y are the horizontal and vertical positions of the hit, and c is the speed of light. For each combination of silicon telescope and Neutron Wall cell, this reference point in the time spectra can be found and ΔT_c chosen appropriately. This correction takes into account differences in cable delays, and electronic responses.

The time must also be corrected for the time a fragment takes to arrive at the telescope and trigger the electronics. This correction, T_{Si}, adds the flight time for the fragment and an energy dependent walk factor,

$$T_{Si} = d_{Si}/v_{Si} + \alpha(E).$$

The velocity, v_{Si} is calculated from the mass and energy of the isotope measured. The fragment flight time, d_{Si}/v_{Si}, is usually 2-5 ns. The silicon time was measured with a leading edge discriminator, so a walk correction is also needed, $\alpha(E)$.

The walk correction was determined empirically from the data. In a plot of the energy signal measured in the ΔE detector versus T_n for prompt gamma rays, the curvature caused by walk is evident (Figure 3.9 top). The maximum of the prompt gamma peak is fitted by a function $\alpha(\Delta E) = \tau\sqrt{\log(\Delta E / \Delta E_{th})}$, where E_{th} is the energy

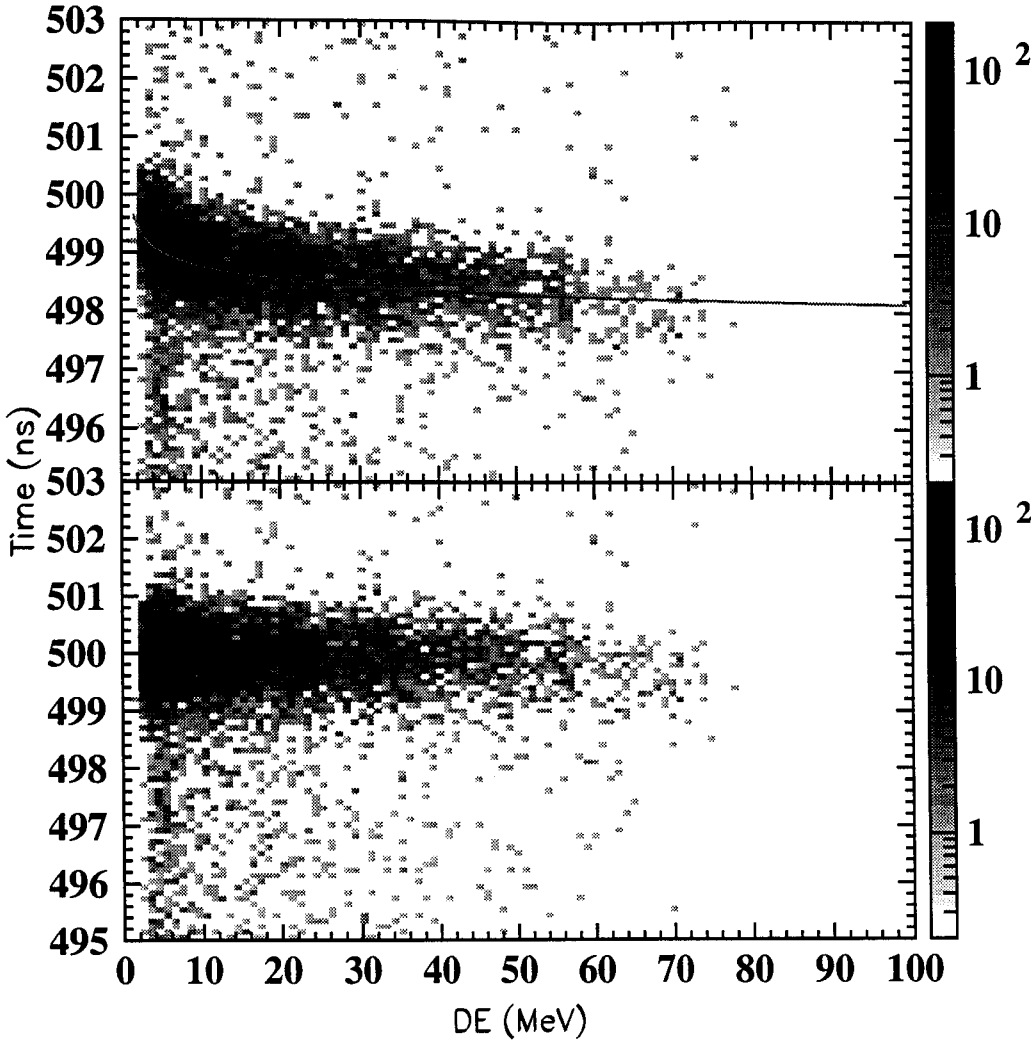

Figure 3.9 Walk correction for the timing signal from the leading edge discriminator. The top panel shows the time for the prompt gamma peak measured by the Neutron Wall, T_n, versus the ΔE signal before correction. The line is the fit used to correct for walk. The bottom panel is the same plot after the walk correction $\alpha(E)$ has been applied.

threshold and τ is adjusted for each detector. After correction the energy dependence of the prompt gamma's time is removed (Figure 3.9 bottom).

After these corrections, the time spectra shows the width of the gamma peak and thus the resolution of the detector and electronics (Figure 3.10). The time is plotted as

$$\text{time} = 500\ \text{ns} + T_\gamma\text{-TOF}.$$

For most detectors the full-width at half-maximum (FWHM) resolution is about 1.0 ns. One of the fan-in fan-outs (FIFOs) used to split the stop signal introduced additional noise in the detector timing. This noise added a width of about 1 ns to the resolution of one third of the detectors. The gamma peak for these detectors measured about 1.4 ns FWHM.

The neutron energy can be easily calculated from the TOF. Relativistically,

$$E_n + mc^2 = \sqrt{m^2c^4 + \left(\frac{\frac{v_n}{c} mc^2}{\sqrt{1-\left(\frac{v_n}{c}\right)^2}} \right)^2}$$

where m is the mass of the neutron and $v_n = \frac{d_n}{TOF}$. The distance to the hit is d_n. The energy spectra measured for single neutron events is shown in Figure 3.11. The energy spectra for the front and back walls differ somewhat because the first wall acts as a scatterer for the neutrons arriving at the back wall.

3.3.2.2 Neutron Position

Besides providing energy information, the time signal also measures the position of an interaction in the detector. If the neutron interacts close to one photomultiplier tube,

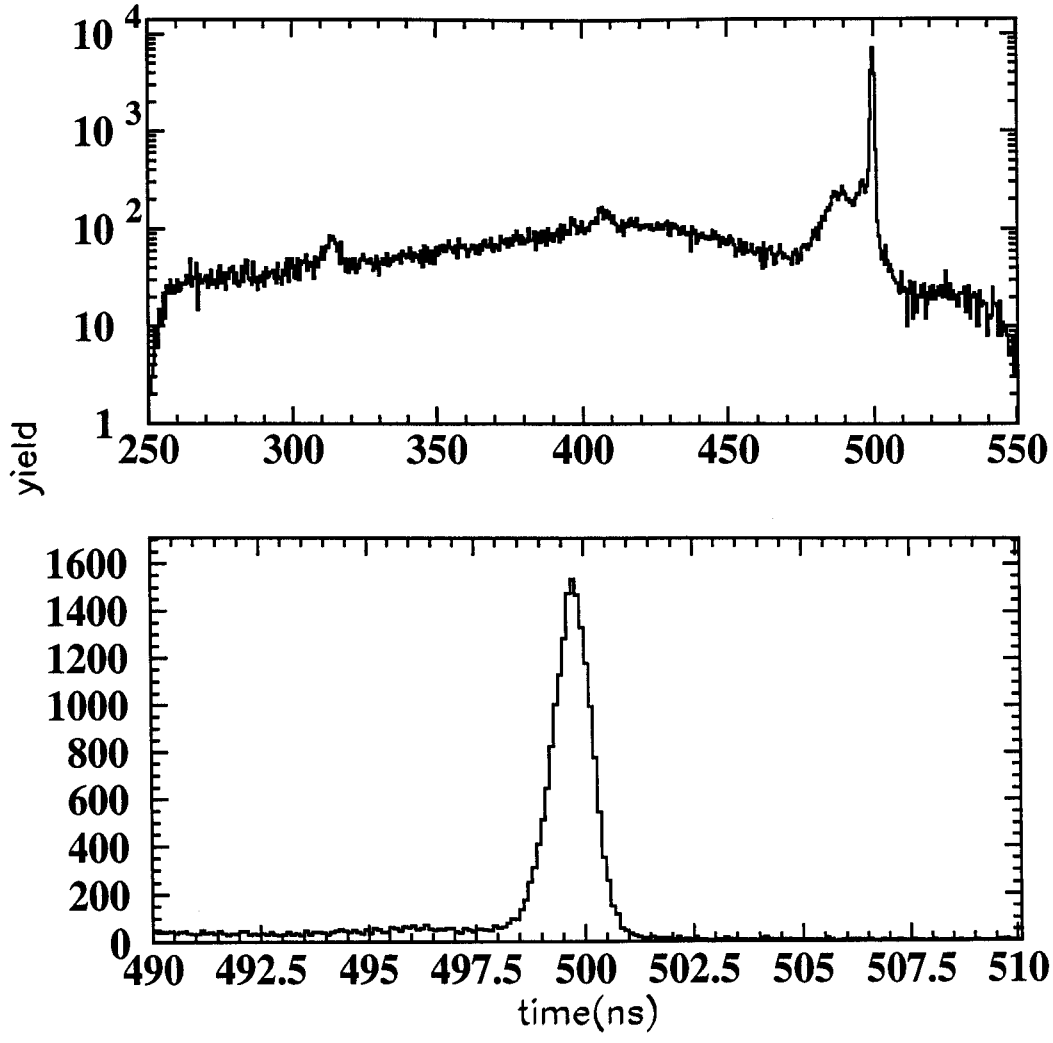

Figure 3.10 Time spectra for the Neutron Walls after all correction, T_γ - TOF + 500 ns. The bottom panel is an expansion of the region around the prompt gamma peak.

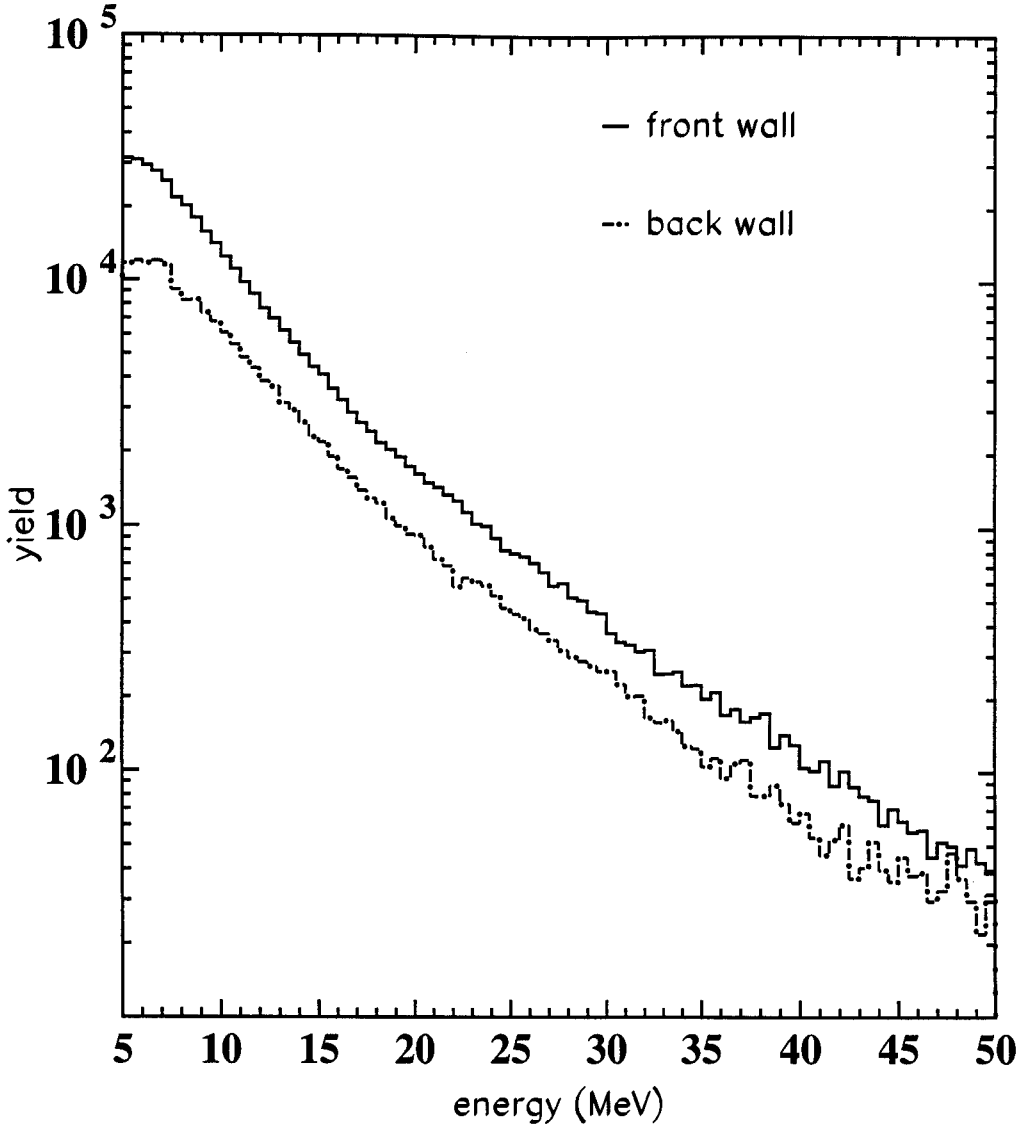

Figure 3.11 Energy spectra for the Neutron Walls (front and back detectors). These spectra are not efficiency corrected.

the light produced takes less time to reach that PMT and longer to reach the other side. The difference in time between the two signals measures the position of the interaction, $t_p(x) = t_L - t_R$. The position in centimeters, x, was determined by the times at the edges of the wall, x_L and x_R, $x = t_p(x) \frac{200cm}{t_p(x_L) - t_p(x_R)}$. The edges of the distribution were designated as the place where the number of counts fell to half of the full yield.

The position resolution can be seen by shadowing a part of the wall. A shadow bar 35 cm long that shadowed 36 cm on the wall was placed into the path of the neutrons (Figure 3.12). These adjacent detectors measure the same size for the shadow bars, and the resolution is better than 5 cm FWHM.

The position spectra also show some structure, especially near the center of the tube. This non-linear response was later shown to be the result of electronic crosstalk between different channels within the CFD. A signal in one channel induces noise on the neighboring channels, so when two signals arrived at nearly the same time the crossover time is shifted. Each detector was cabled so that the signal from the right and left PMT were in adjacent channels. For one location in the detector, usually near the center of the tube, the signals arrive simultaneously at the CFD, $\Delta t = 0$ (Figure 3.12).

The correlation function should not be effected by this electronic crosstalk, since the effect for one detector changes the numerator and denominator in the same way. The only way this electronic crosstalk could change the correlation function is if it caused a correlation between different detectors. To investigate this correlation, the position is plotted for one detector when another detector in the same (Figure 3.13, lower panel) or

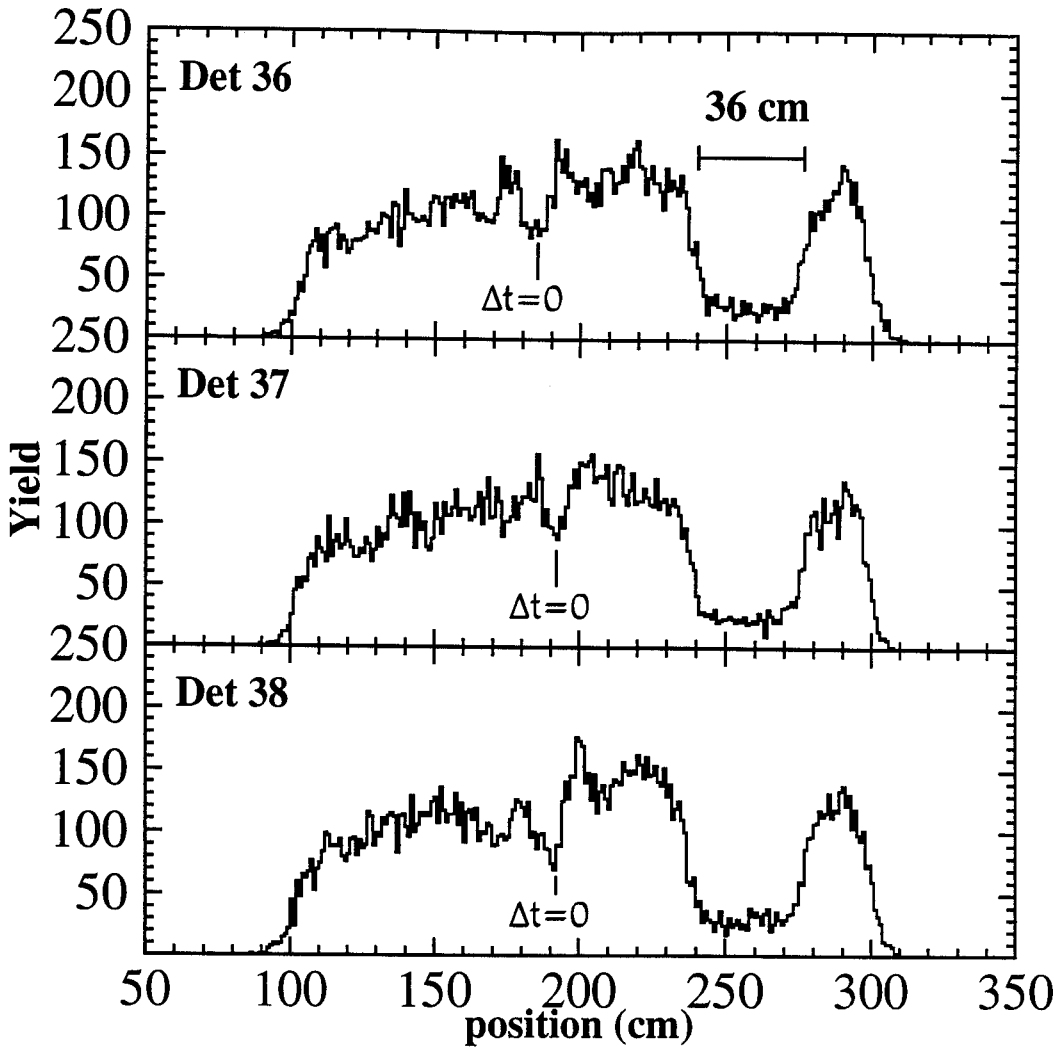

Figure 3.12 Position spectra for the Neutron Walls. A shadow bar creating a shadow of 36 cm was placed in front of one section of these detectors, creating a large suppression in the yield. The other structure in this spectra is the result of electronic crosstalk.

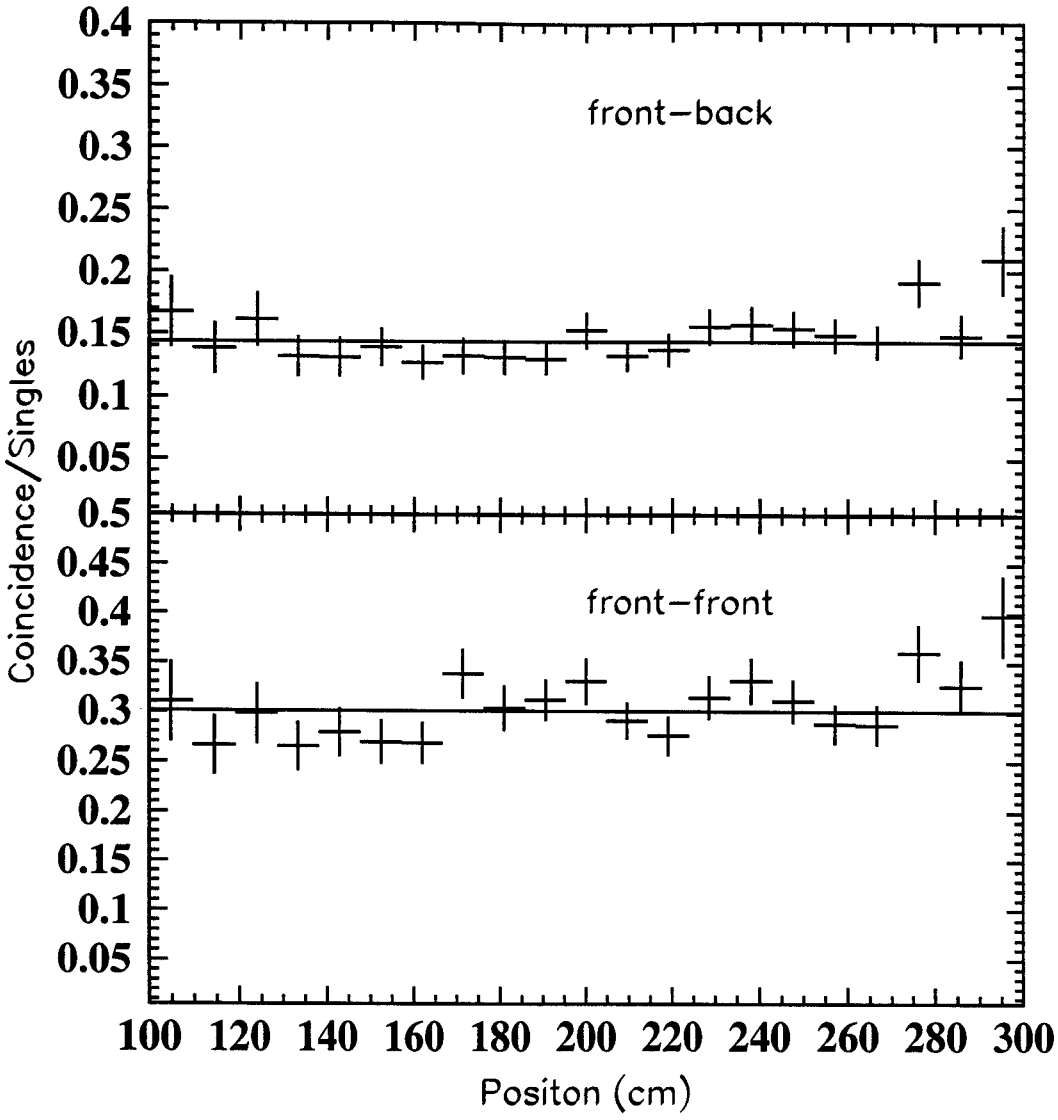

Figure 3.13 The coincidence signal for one detector either in a front-back (top panel) or front-front (bottom panel) pair divided by the singles yield for that detector.

opposite (upper panel) wall fires. The spectra are divided by the singles spectra for the same detector.

$$\frac{\text{Coincidence}}{\text{Singles}} = \frac{\sum Y_2(\vec{p}_1, \vec{p}_2)}{\sum Y_1(\vec{p}_1)},$$

where the numerator is summed over all $\vec{p}_1$ for one detector and all $\vec{p}_2$ for detectors in the appropriate wall. The denominator is summed over all $\vec{p}_1$ for the one detector. Within the error bars there does not seem to be any correlation in these spectra. Detectors in opposite walls should not have any correlations since their signals are processed in different CFDs.

3.3.2.3 Neutron Particle Identification

The pulse shape discrimination in the neutron walls allows a separation of neutrons and gammas. Two different scales were used for the particle identification. Figure 3.14 shows the "Fast" signal versus the "Attenuated Total" signal, used for higher-energy neutrons and Figure 3.15 shows "Total" versus a PID function used for low-energy neutrons. The PID function was determined empirically to expand the resolution of the lower-energy part of the spectra and to straighten the results.

$$\text{PID} = 7.9898\ F - 0.003413\ F*T + 0.00188\ T^2 - 4.439\ T + 1116,$$

where F is "Fast" and T is "Total." By gating on these spectra it is possible to eliminate most of the gamma rays. The timing spectra after the gammas are eliminated show a reduction of the height of the gamma peak from $2x10^4$ to $1x10^3$ counts (Figure 3.16).

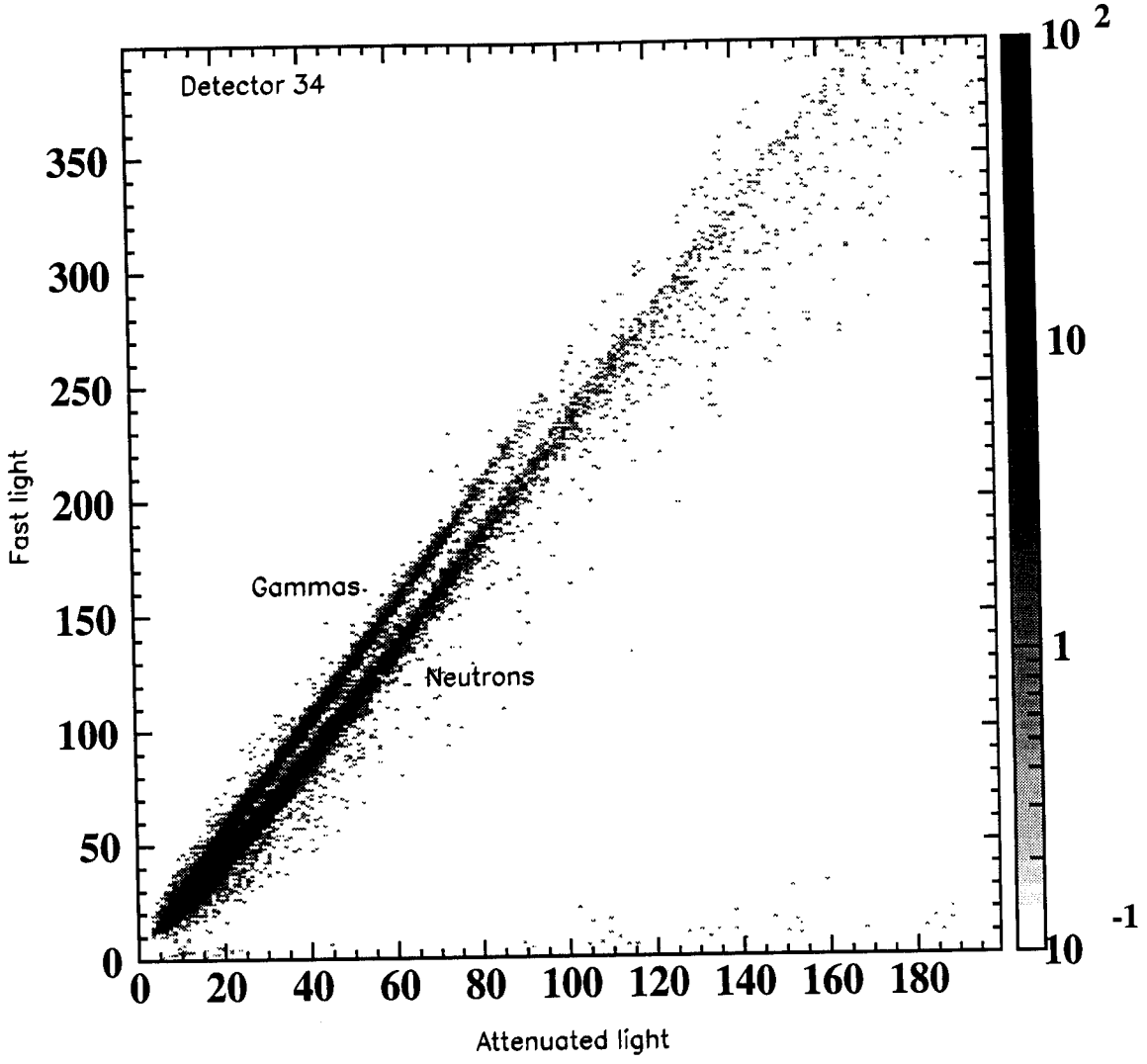

Figure 3.14 Neutron-gamma discrimination for the high energy neutrons in the Neutron Walls. The plot of "Fast" versus "Attenuated Total" signal shows a separation between neutrons and gammas.

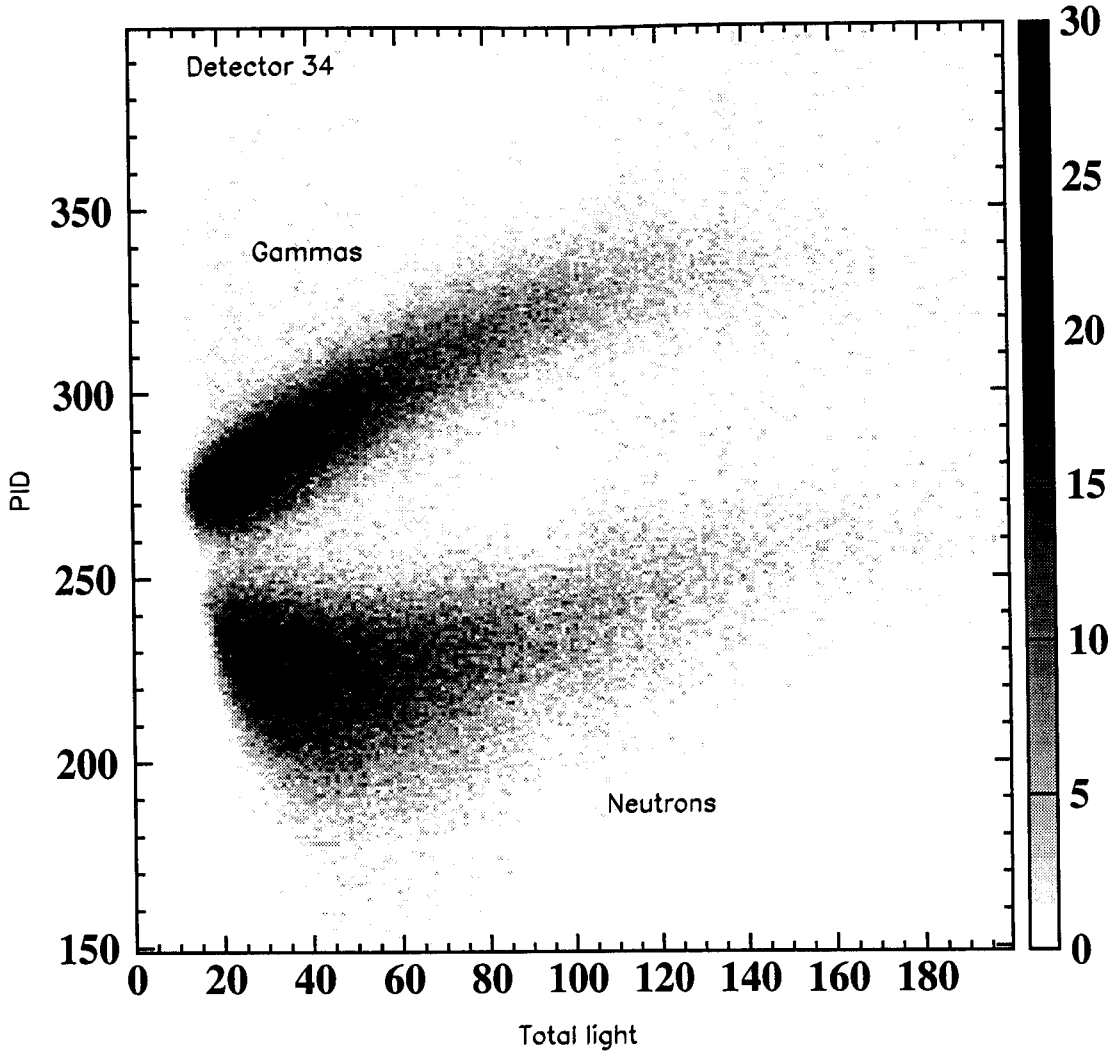

Figure 3.15 Neutron-gamma discrimination for the low energy neutrons. "Total" signal versus a particle identification, PID, chosen to straighten and expand the spectra. See text for definition of PID.

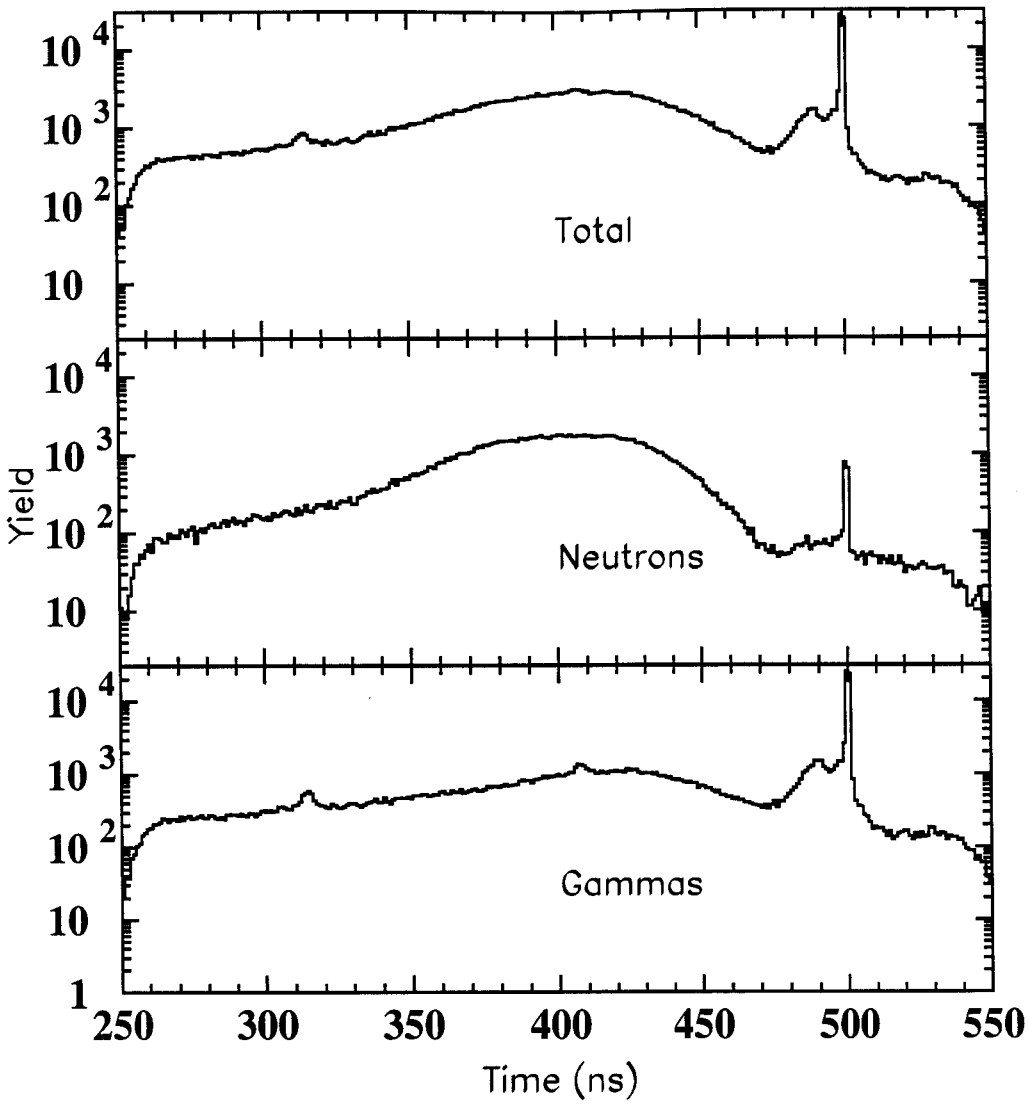

Figure 3.16 Timing spectra for the Neutron Walls. The top panel shows the time spectrum for all hits. The middle panel is gated on neutrons identified by gates on either the high or low energy discrimination plot. The bottom panel is gated on gammas identified by either gate in the discrimination plots.

3.3.2.4 Neutron Light

In order to correct for detector crosstalk (Section 4.2.2), it is important to relate the light signal to the amount of energy deposited in the cell by a neutron. The light is calibrated and then related to the proton energy necessary to produce this much light. The proton energy is used to identify the crosstalk events.

The light intensity measured in each PMT by the "Attenuated Total" signal was calibrated by looking at the Compton edge of various gamma sources: $^{12}C(E_x = 4.44$ Mev) in a PuBe, ^{228}Th and ^{60}Co (Figure 3.17). The Compton edges were found from the light for events from a restricted range of positions in the Neutron Walls. The light is calibrated in units compared to the light produced by a 1 MeV electron (1 MeV electron equivalent, 1 MeVee) which is the most light a 1 MeV gamma ray can produce.

The total light signal is a position-independent combination of the calibrated left and right signals. The individual signals at a position x defined from the left side of the cell can be represented by $L_{left} = L\, e^{-x/\lambda}$ and $L_{right} = L\, e^{-(d-x)/\lambda}$, where L is the total light produced, d is the length of the cell and λ is the attenuation length (Figure 3.18). A position-independent signal can be constructed by taking the geometric mean of the two light signals, $L = \sqrt{L_{left} * L_{right}}$.

From the total light, L, the proton energy can be reconstructed using a light response curve, $E_p(L)$. Two light response curves were used. (Figure 3.19). The first is based on a fit of the data from References [Verb 68, Ceci 79]. The second response curve

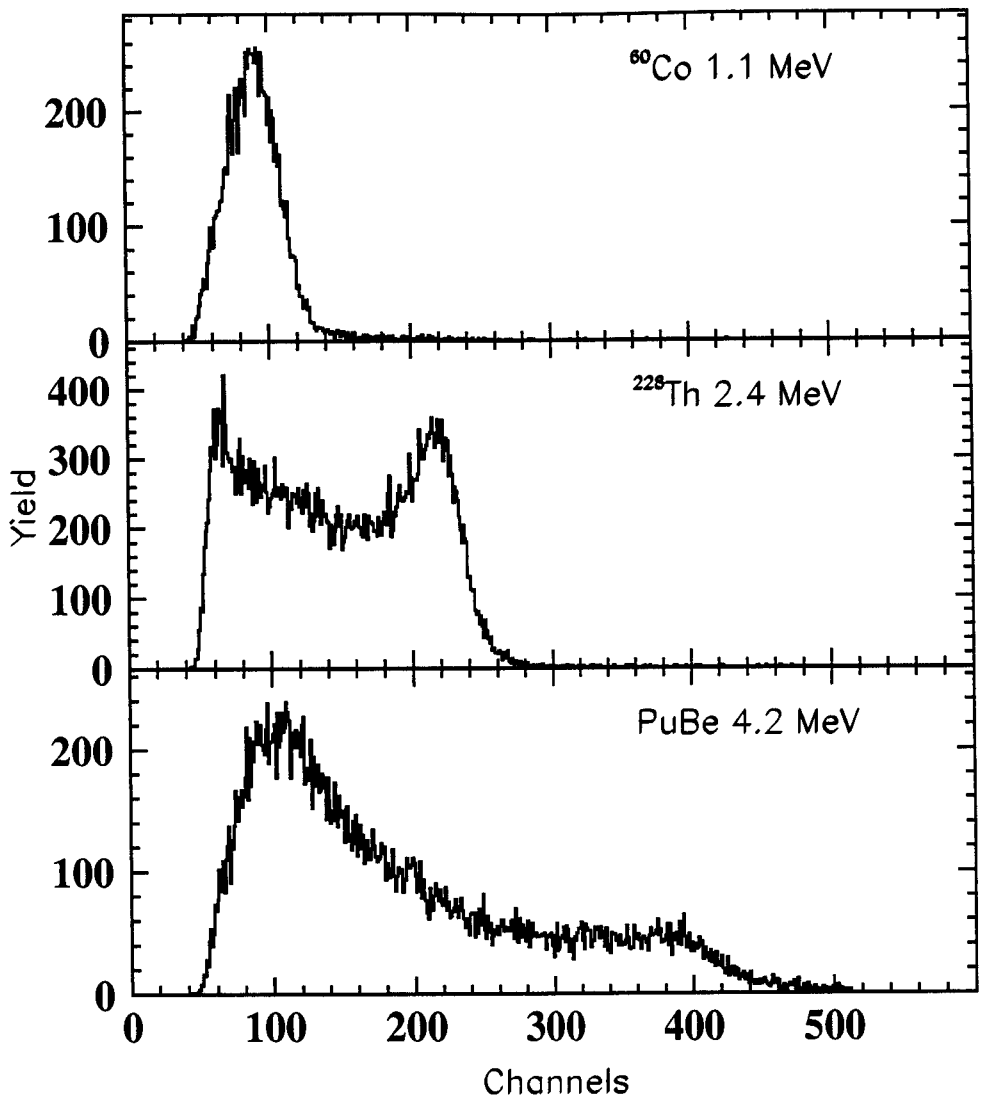

Figure 3.17 Light spectra showing the Compton edges used to calibrate the light signal for the Neutron Walls. The sources and the energy of the Compton edge are given in the figure.

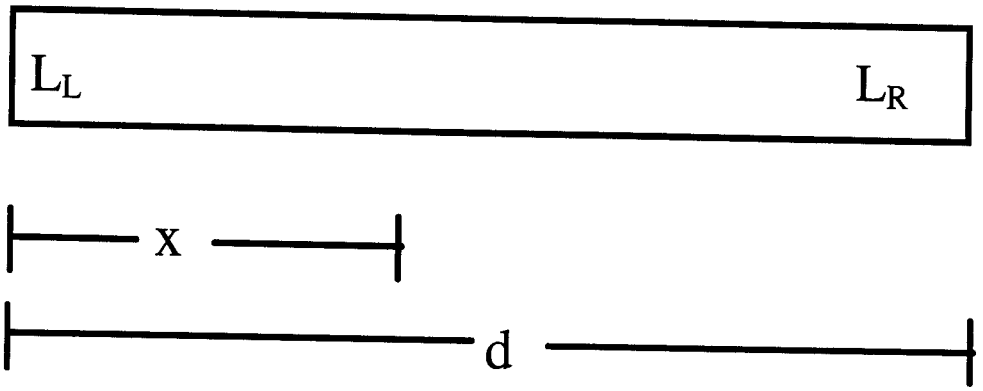

Figure 3.18 Definition of x for the determination of the left and right light signals.

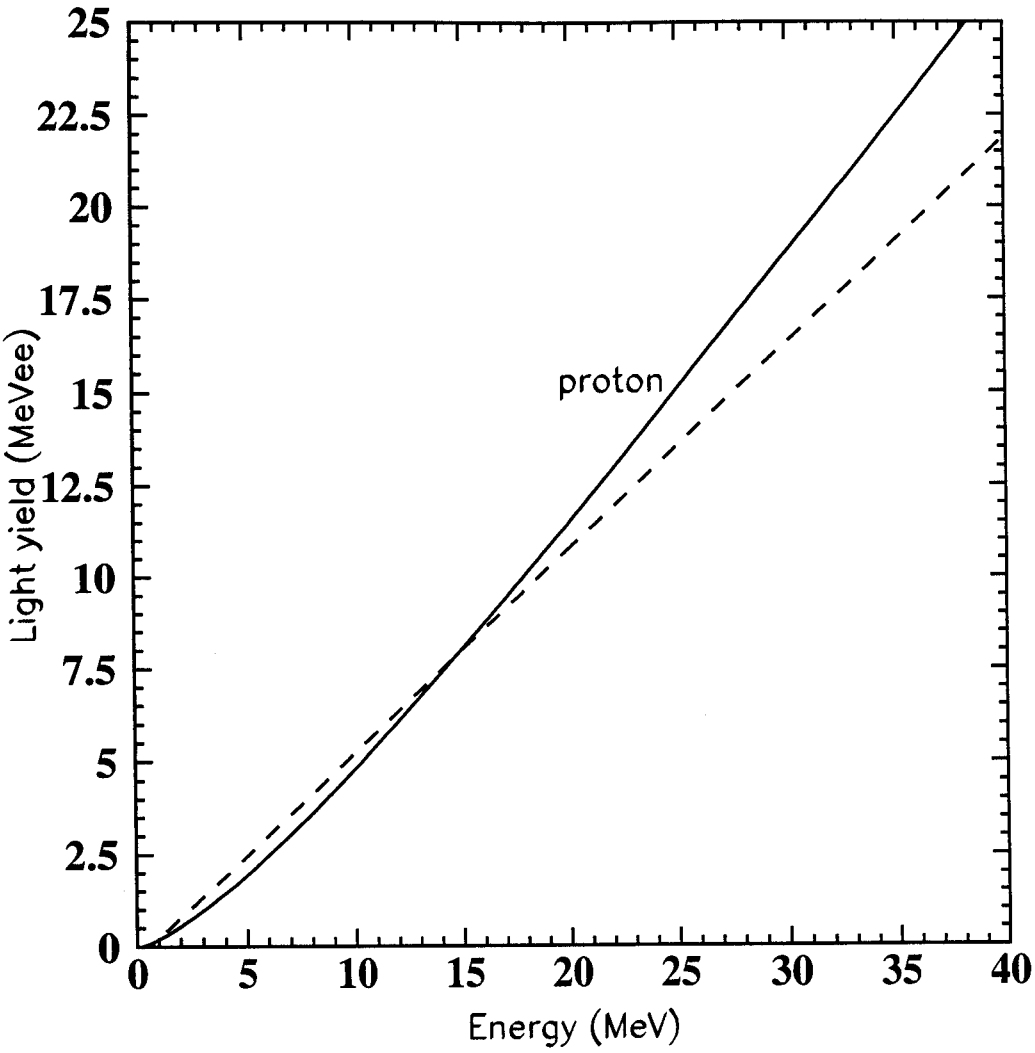

Figure 3.19 Neutron energy versus the highest light yield. The solid line shows a fit to Verbinski data while the dashed line shows a linear fit empirically chosen from the data.

is a linear fit to the maximum light as a function of energy. The second curve was chosen to make symmetric cuts on the crosstalk variables described in Section 4.2.2.

The linear fit was determined from the light intensity as a function of the neutron energy (Figure 3.20). The maximum light for a given energy neutron can be seen as an edge of the distribution, where a line is drawn in this figure. It is reasonable to use the edge of this distribution to estimate the light response function, because the light measured for a given neutron energy is expected to correspond to a flat distribution of proton energies up to a maximum of the total incident neutron energy. This expectation can be seen from the following derivation. The solid angle in the center of mass of the proton and neutron is

$$d\Omega_c = 2\pi \sin\theta_c \, d\theta_c,$$

where θ_c is the scattering angle for the neutron in the center of mass. If one assumes that the masses of the neutron and proton are the same, then the center of mass angle is twice the laboratory angle, $\theta_c = 2\theta_L$ (Figure 3.21). Then

$$d\Omega_c = 8\pi \sin\theta_L \cos\theta_L \, d\theta_L.$$

By scattering kinematics, the final proton energy, E_p, and incident neutron energy, E_n, are related by

$$E_p = E_n \sin^2\theta_L,$$

$$dE_p = 2 E_n \cos\theta_L \sin\theta_L \, d\theta_L.$$

With this information, the yield can be found as a function of the proton energy:

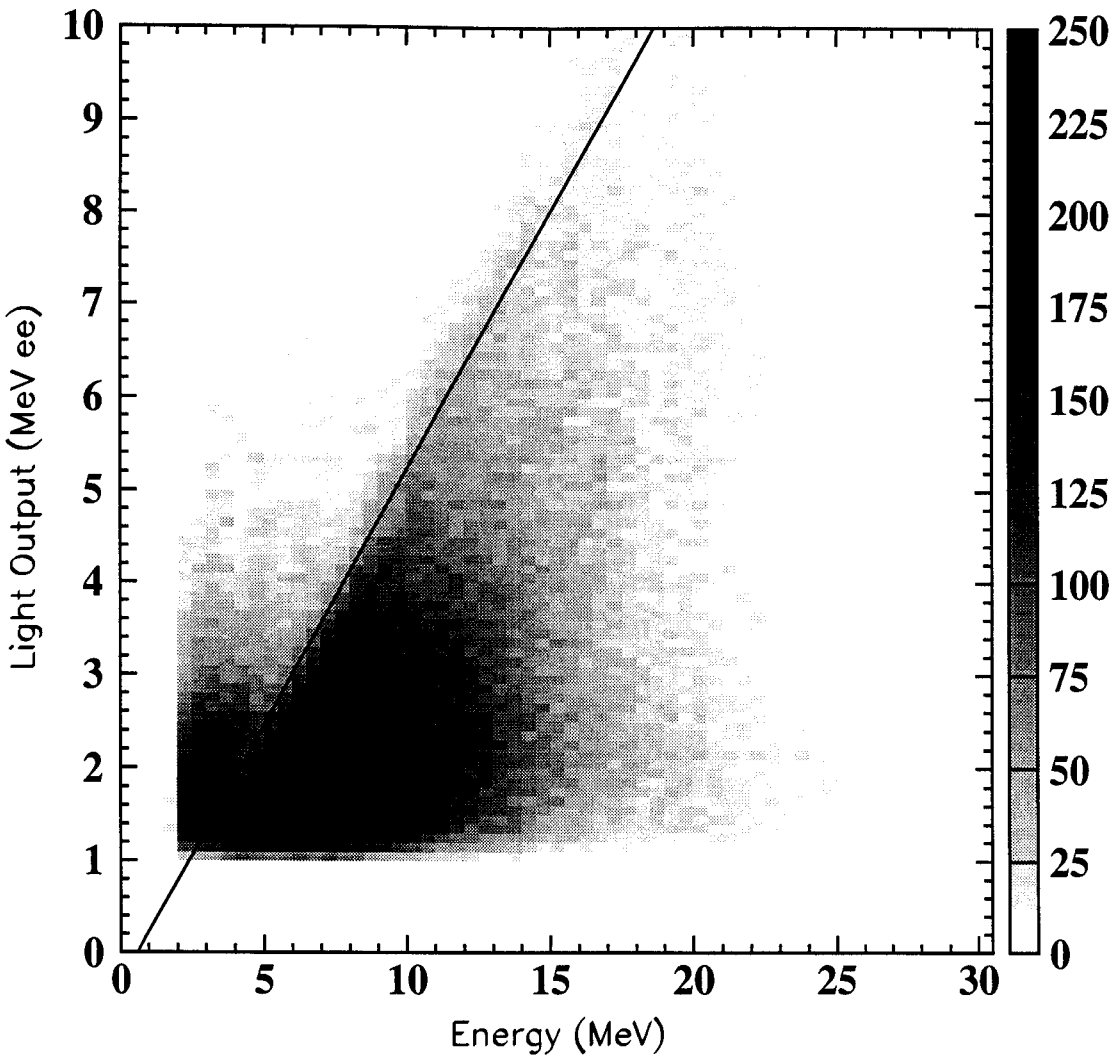

Figure 3.20 Light output versus energy of the neutrons. Neutrons that come directly from the target cannot have light corresponding to a proton energy greater than the neutron energy. The line shows the cut made to exclude background neutrons.

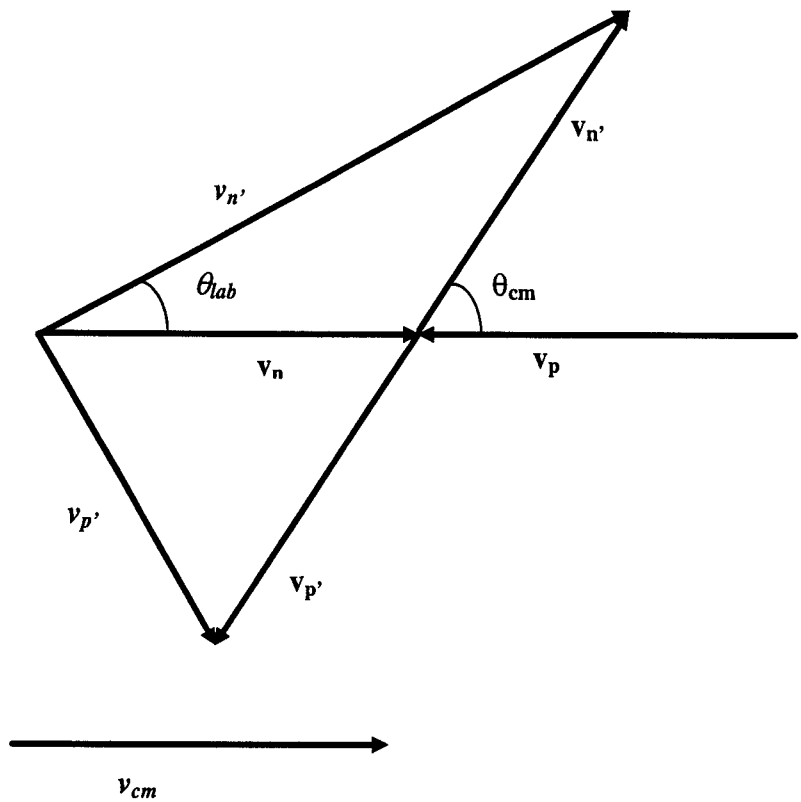

Figure 3.21 Kinematics of neutron scattering. Variables in the laboratory frame are shown in italics while variables in the center of mass frame have a standard font. Note: $|v_n|=|v_{n'}|=|v_p|=|v_{p'}|$

$$\left(\frac{dN}{dE_p}\right)dE_p = \left(\frac{dN}{d\Omega_c}\right)d\Omega_c,$$

$$\left(\frac{dN}{dE_p}\right) = \left(\frac{dN}{d\Omega_c}\right)\frac{d\Omega_c}{dE_p}$$

$$= \left(\frac{dN}{d\Omega_c}\right)\frac{8\pi \sin\theta_L \cos\theta_L d\theta_L}{2E_n \sin\theta_L \cos\theta_L d\theta_L}$$

$$= \left(\frac{dN}{d\Omega_c}\right)\frac{4\pi}{E_n}.$$

Since $dN/d\Omega_c$ is a constant for s-wave scattering, the yield at a given neutron energy is independent of the proton energy, as long as $E_p < E_n$. This condition is required by energy conservation. The light yield from the detector for certain selections of neutron energy is shown in Figure 3.22. The detector resolution and detector inefficiency cause these spectra to differ from the box shape expected.

3.3.3 Measured Background

Background neutrons can effect the correlation function, so it is important to understand the amount and characteristics of the background. Some neutrons come from the target, but scatter before they reach the detector. These background neutrons can scatter from the walls of the vacuum chamber or from the walls and other material in the experiment room.

In order to measure the magnitude of this background, a large shadow bar was placed in the direct path from the target to the Neutron Walls. The shadow bar was located just outside the vacuum chamber, 46 cm from the target. A pile of steel 40 cm

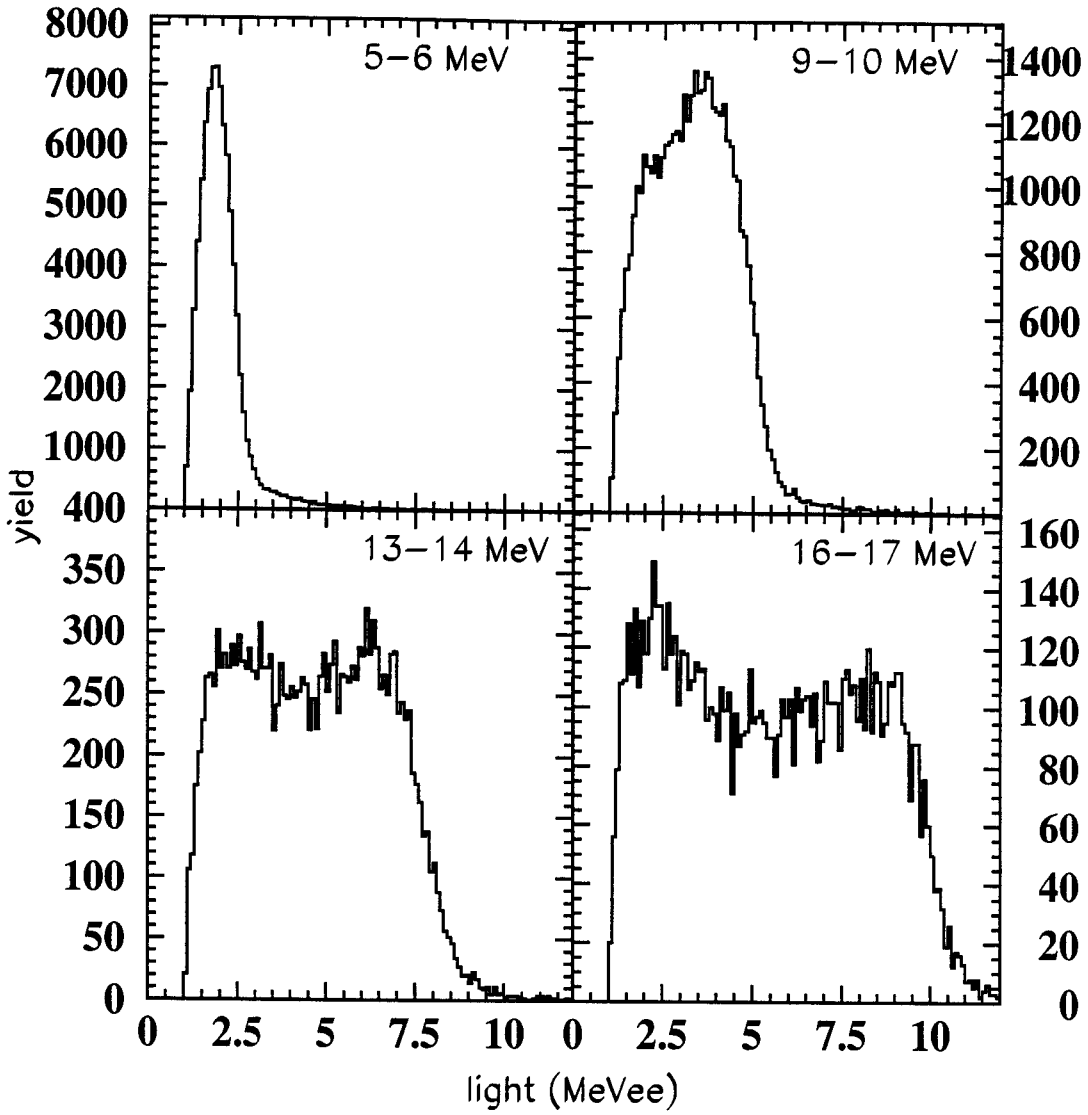

Figure 3.22 Light yield at a given neutron energy. A flat distribution from threshold to maximum possible light is expected. The four panels represent different gates on the energy of the neutrons. The gate applied is specified in the panel.

long and 35.5 cm x 35.5 cm was located so as to shadow the whole neutron wall. This length was calculated in order to reduce the number of neutrons transmitted to a small fraction [Remi 86]. The number of neutrons neither scattering nor interacting in a length of material x can be determined from the relation

$$N = N_0 e^{-n\sigma_T x},$$

where N_0 is the original number of neutrons, n is the number of nuclei/cm^3, and σ_T is the neutron total cross section. An additional correction must be made for the fraction of neutrons that scatter to small angles and so still reach the detector. This calculation can be done more accurately by dividing the shadow bar into J sections with length x = L/J. The fraction transmitted is

$$F = \Pi_{j=1}^{J}(f_j + (1 - f_j)(\Delta\sigma_{el} / \sigma_T)),$$

here $f_j = N_j/N_0$, the fraction of neutrons making it through a short length of the shadow bar.

$$\Delta\sigma_{el} = \int_{\theta=0}^{\theta_0} \frac{d\sigma_{el}(\theta)}{d\Omega} 2\pi \sin\theta d\theta,$$

where the integral is performed over all angles where the neutron will still reach the detector, and σ_{el} is the neutron elastic cross section. The total and elastic cross sections were taken from Reference [Hugh 58]. From these calculations it is possible to estimate that about 2% of 20 MeV neutrons will arrive at the detector through this shadow bar.

By comparing the normalized spectra for the shadow bar run to a run without a shadow bar it is possible to characterize the energy and detector dependence of the inscattering. In Figure 3.23, the energy dependence of the background/total ratio for one

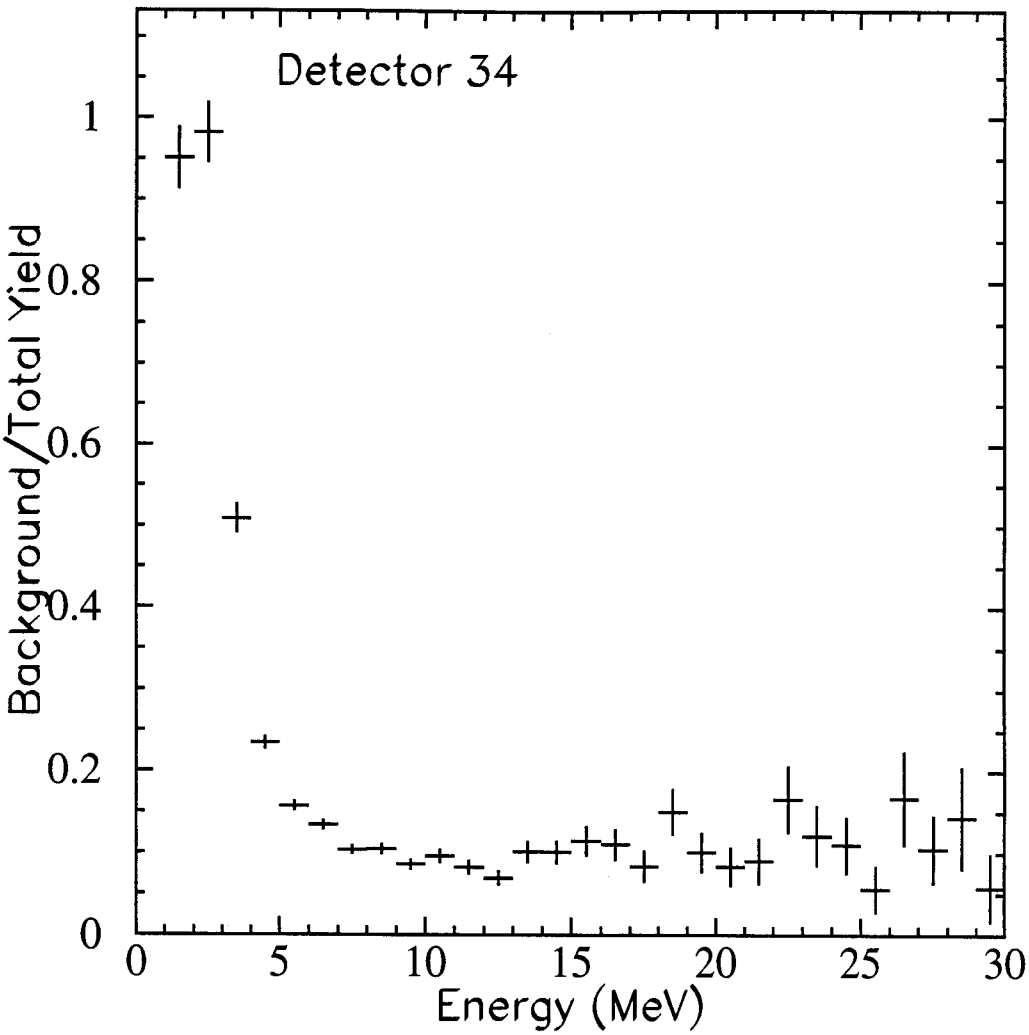

Figure 3.23 Energy dependence of the ratio of background/total neutrons. The yield from a shadow bar run is divided by a standard run and normalized by the total beam current in these runs.

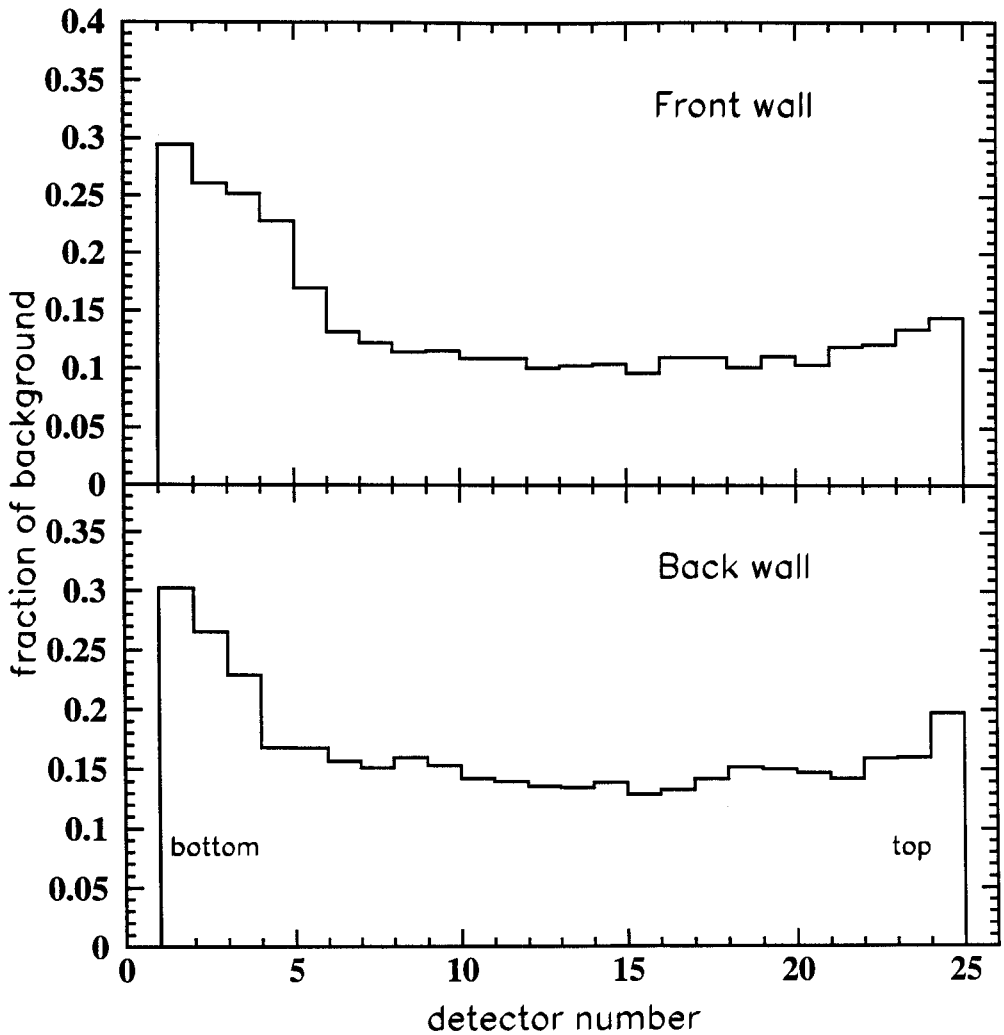

Figure 3.24 Background/total ratio for each detector in the Neutron Walls.

detector is shown. For scattered neutrons, the energy is lowered and the flight path is lengthened by an unknown amount; both effects shift the scattered neutron events into the low energy portion of the spectrum. Indeed, the yield below approximately 4 MeV is mostly background. Figure 3.24 shows how the crosstalk percentage changes with detector number. The detectors closer to the floor and ceiling have more crosstalk. There was no noticeable dependence in the background on the horizontal position within a detector.

Chapter 4 - Two-Neutron Intensity Interferometry: Measured Correlation Functions

4.1 Constructing a Correlation Function

Many previous studies have looked at how correlation functions with identical particles can be used to measure the emission zone of a nuclear reaction [Koon 77, Prat 87, Gong 91a, Gong 91b]. In this section the relevant details are reviewed.

Experimentally, the correlation function is constructed by histogramming events as a function of the (invariant) magnitude of the relative momentum four-vector, $q = \frac{1}{2}|p_1 - p_2|$, and then dividing by a denominator constructed from uncorrelated events. $1 + R(q) = N \frac{\sum Y_2(p_1, p_2)}{\sum Y_{back}(p_1, p_2)}$, where Y_{back} is the yield for uncorrelated events, Y_2 is the coincidence yield, and N is the normalization determined so that $R(q) \rightarrow 0$ at large q [Boal 90 and references therein]. The sums are over all detector and momentum combinations available in the experiment. The correlation function is defined as this ratio to eliminate effects of the single-particle phase space and the detector geometry and efficiency. For this division to be effective, the numerator and denominator must be treated in exactly the same way. In the correlation functions presented here, the same cuts have been applied to numerator and denominator.

The shape of the correlation function for two neutrons reflects the quantum statistics of neutrons and the final-state interactions [Gong 91a, 91b, Colo 95]. The basic

shape of the correlation is a combination of these two effects. If there were only quantum statistics, the correlation would be suppressed at small q (Figure 4.1). ($R(q) + 1 = 0.5$ at $q = 0$, but because the theory is binned in 2 MeV bins the correlation in this figure does not reach 0.5.) However, the final-state nuclear interaction is attractive, so the total correlation is positive for relatively small emission zones.

Intensity interferometry is sensitive to the relative separation of the particles upon emission, and thus the volume of the emission zone [Koon 77, Bert 89]. Consider a source with a radius, r, and a lifetime, τ, where the particles move away from the source with an average speed v. The initial spatial separation, $r + v\tau$, depends on both the radius and lifetime. If the source is small and the lifetime is short, the correlation will be strong (Figure 4.2a). On the other hand, a weaker correlation could come either from a source with a large size and short lifetime or from a small source with a long lifetime (Figure 4.2b and c).

In order to separate lifetime and size effects, it is possible to make a cut on the direction of the relative momentum, $\vec{q}$, compared to the total momentum, $\vec{P}$, of the particle pair. For dimensions on the nuclear scale, the attractive s-wave interaction gives rise to a positive correlation. This nuclear effect is sensitive to the volume of the source emitting particles. However, the effects of the Pauli exclusion principle depend on the shape of the emission zone. The two-neutron wave function must be antisymmetrized, and thus relative momentum states, Δp, will be suppressed over a range $\Delta p \approx \hbar / \Delta x$ where Δx is the average spatial separation. The width of the suppression is primarily

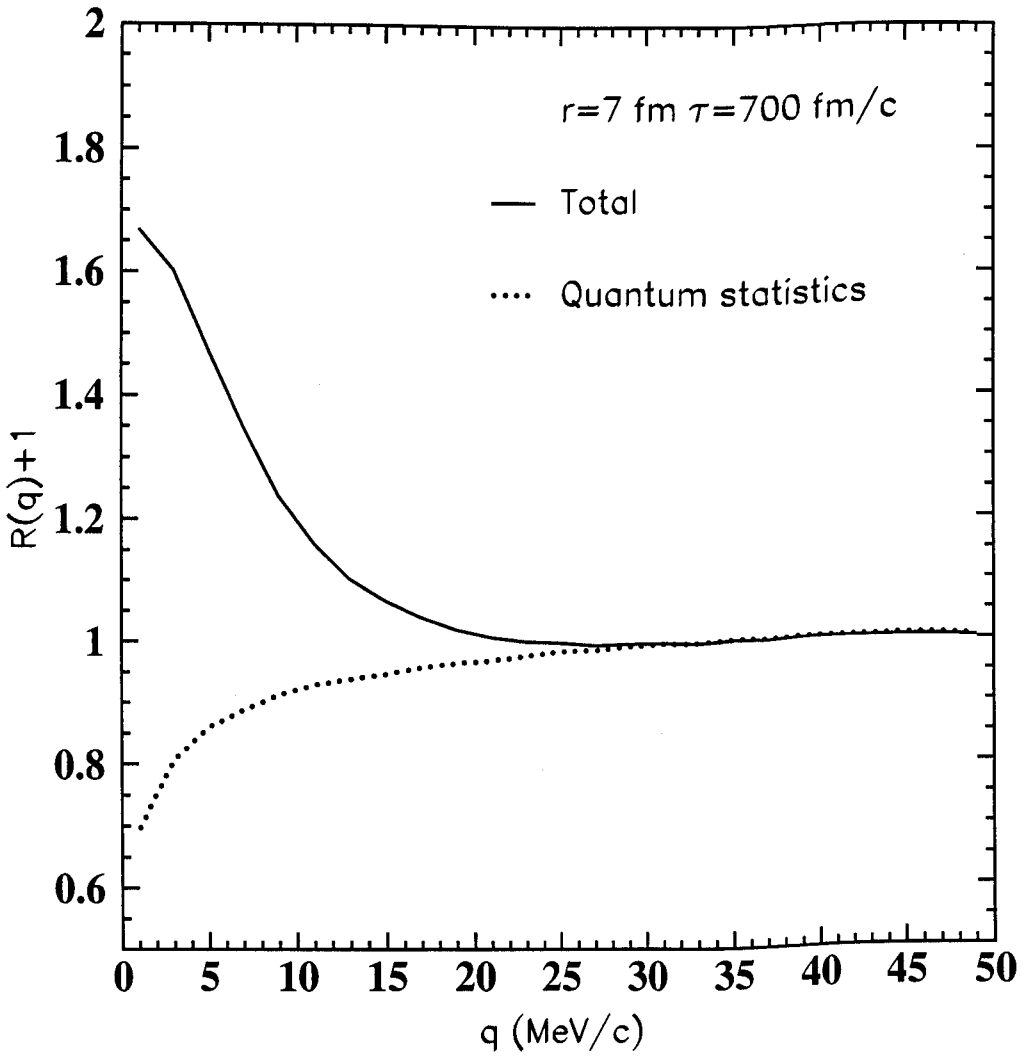

Figure 4.1 Theoretical two-neutron correlation function. Surface emission from a sphere of radius 7 fm with a lifetime of 700 fm/c. The solid line shows the standard two-neutron correlation function. The dotted line shows the correlation from only quantum statistics with no final-state interactions.

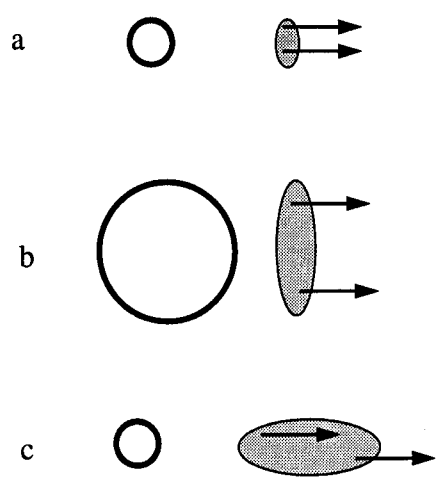

Figure 4.2 Spatial distribution of emitted particles of velocity v from three sources. (a) Small source with a short lifetime (b) Large source with a short lifetime (c) Small source with a long lifetime.

sensitive to the spatial size in the direction of the relative momentum [Boal 90, Prat 87, Awes 88]. If the particles are emitted over a lifetime, the distribution of particles emitted with velocity $v \approx \vec{P}/2m$ is elongated in the $\vec{P}$ direction by $d \approx r + v\tau$ (Figure 4.3) [Hand 95c]. Particles with their relative momenta perpendicular to the $\vec{P}$ direction sample a smaller dimension (of the order of the source radius). At small relative momenta, these particles experience a stronger anticorrelation from the antisymmetrization effects and thus the transverse correlation function is reduced. The directional differences are seen by comparing the two classes of events, longitudinal and transverse, based on the angle $\Psi = \cos^{-1}(\vec{P} \cdot \vec{q} \,/\, Pq)$. This angle must be constructed in the reference frame of the source emitting the particles, so that the directions are aligned appropriately with the source [Lisa 93c].

4.2 Experimental Correlation Function

In constructing the correlation function, it is important to select the appropriate coincidence data. Cuts must be made to choose the central events, to correct for crosstalk between detectors, and to correct for scattering from the vault. Other cuts simplify modeling of the detector.

4.2.1 Event Selection: Individual Neutrons

Because the event trigger recorded many events which did not satisfy the criteria applied for construction of the correlation function, additional requirements were

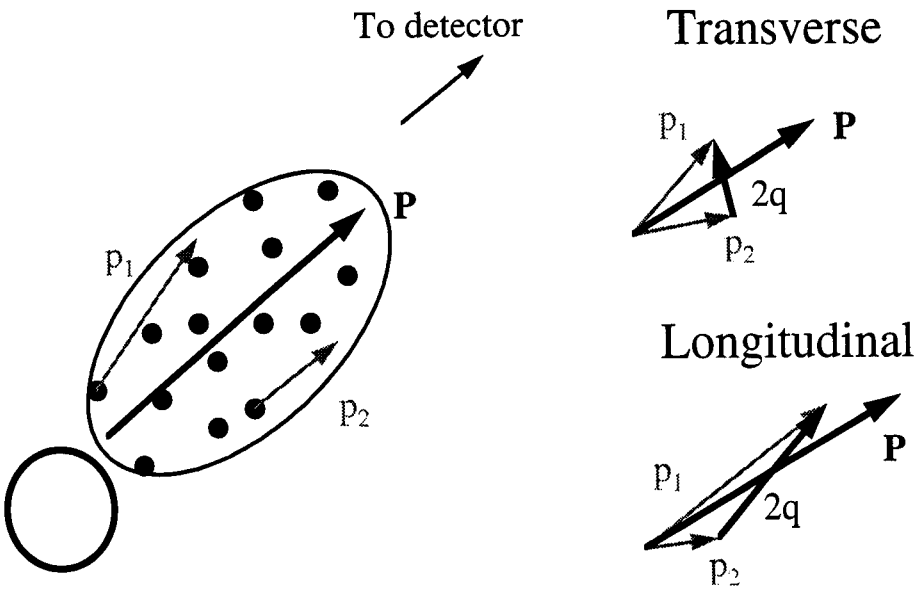

Figure 4.3 Definition of longitudinal and transverse directions. Transverse samples the small dimension of the source while longitudinal samples the lifetime dimension.

imposed in the analysis. Criteria include the charged-particle identification, neutron characteristics, and the multiplicity of neutrons.

One requirement was that the fragment telescope measures one identified isotope with a charge greater than two. The hardware particle selection was not completely effective and so the remaining light particles were excluded in the analysis. Particles that could not be identified as specific isotopes were also excluded, since the particle mass is necessary to correct the neutron time-of-flight. Events with two or more fragments were also excluded because the electronics did not unambiguously distinguish which particle was first, thus causing trouble in correcting the neutron time-of-flight.

No on-line selection was made for gamma-neutron discrimination so this requirement was also added in software. Using the pulse-shape discrimination characteristics of the Neutron Wall detectors, all hits were required to fall into one or both of the neutron gates set for low-energy and high-energy neutrons. This requirement eliminated most of the gamma events coming from the target (See section 3.3.2.3).

Each hit in the neutron detectors should give appropriate values for all measured quantities. The light threshold was set slightly below 1 MeVee by the electronics, but varied from detector to detector. A cut of 1 MeVee was applied to the light signal of each PMT. This software cut makes the spectra easier to simulate. The effect of this cut on the total light threshold as a function of position is shown in Figure 4.4. The position measured was required to be within 1.05 meters of the center of the detector. Some events appear to be outside of this range and probably come from double hits in the detector,

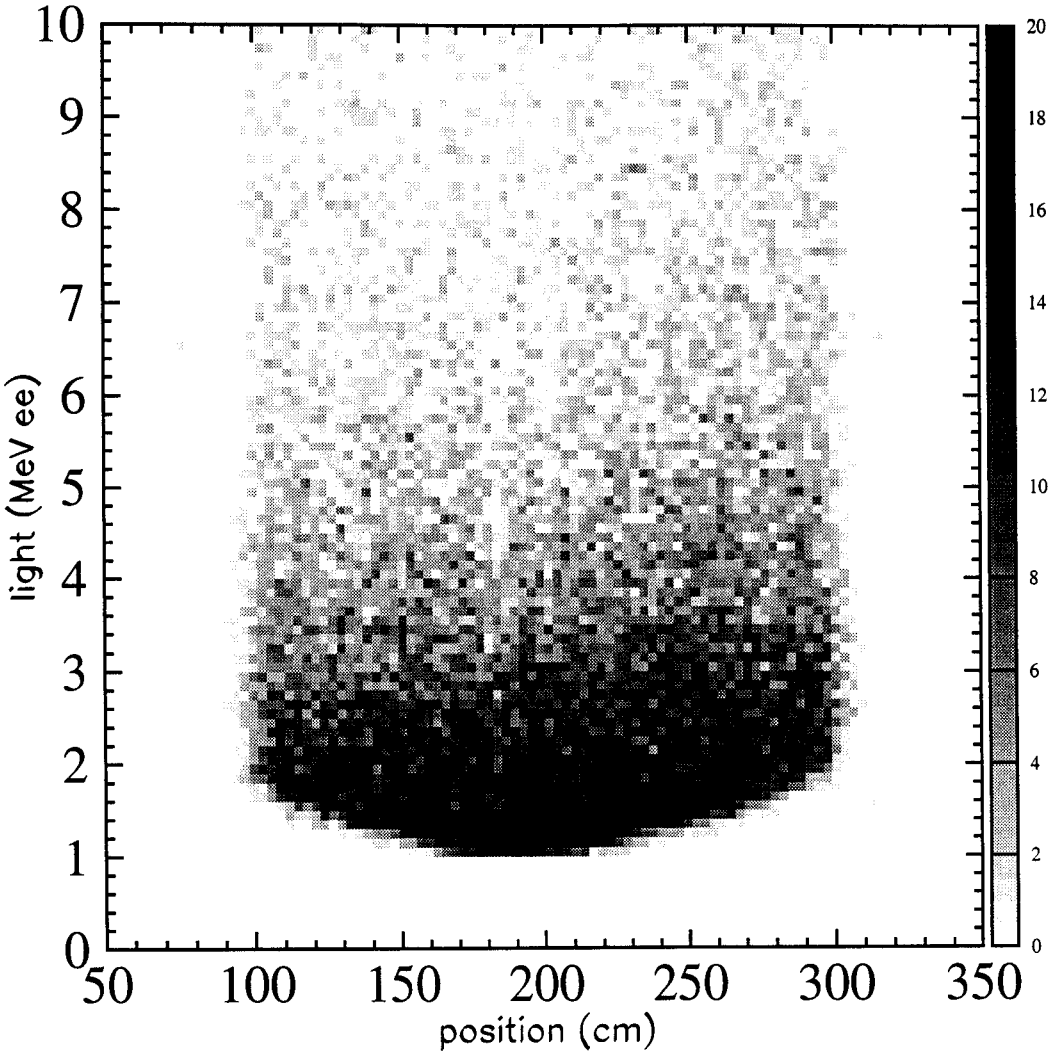

Figure 4.4 The position versus the geometric mean of the measured light for one detector. A 1 MeVee threshold was applied to each PMT.

where the first hit triggered only one of the PMTs. The maximum energy of the neutron was cut at 50 MeV to aid in simulation.

Several requirements were made of the neutron hits in order to eliminate background scattering. As shown previously, the lowest-energy neutrons include many events that are actually background neutrons (Figure 3.22), so a software threshold was applied on the data at 5 MeV. This cut removes many of the background neutrons. A cut on light measured versus energy of the neutron also provided a way to eliminate some background events. Figure 3.20 shows the cut made to eliminate these background events. The shadow-bar run indicates that about half of the background events were eliminated by this cut.

Another selection requirement was the multiplicity of neutrons. For the numerator, coincidence neutrons were required. Events with more than two neutrons were not included because of the difficulty in making effective crosstalk rejections for three or more hits. In the denominator, events were selected from those with one and only one neutron measured (a gamma could be in coincidence). The standard definition of singles includes all events with one or more particles, but in this case an ambiguity exists in how to treat the coincidence events where one hit appears to come from crosstalk. Usually selecting events based on detected multiplicity is a cut on the reaction multiplicity and thus reaction type. Because the detection efficiency of the Neutron Walls is only about 10%, selection on detected multiplicity is not strongly related to the multiplicity of neutrons produced in the event. 79% of the events where two neutrons are incident upon the wall will appear as singles. Also, singles are at least 30 times more plentiful than

coincidences, so the difference between excluding coincidences and keeping them is small. For one run there were 330,000 singles in the front and 150,000 in the back that fulfill all individual neutron criteria. There were 7000 coincidences for the same run where both neutrons fulfill all the individual neutron criteria.

4.2.2 Event Selection: Crosstalk Correction

In making neutron coincidence measurements, it is necessary to correct for crosstalk. A significant fraction of the measured coincidences comes from crosstalk, where one neutron is detected and then scattering into another detector where it is detected again.

Most neutrons are measured in the scintillator when they interact with a proton by elastic scattering (Figure 4.5). Standard scattering kinematics allow calculation of the energy and angle of the outgoing neutron, $E_{n'}$ and θ', if the incident neutron energy, E_n, and the scattered proton's energy, E_p, are known. Since the neutron energy has been calculated from the time-of-flight and the proton energy can be found from the measured light, it is possible to reconstruct with some accuracy where the scattered neutron should go and with what energy.

For each multiplicity-two neutron event, several pieces of information are available for each hit, including the time the neutron hit the detector, t_i, the amount of light detected, L_i, the location of the hit relative to the target which gives the initial velocity, $\vec{v}_i$, and the calculated energy of the neutron, $E_i = 1/2\ mv_i^2$. This information can be used to compare the measured event to the calculated crosstalk event (Figure 4.6).

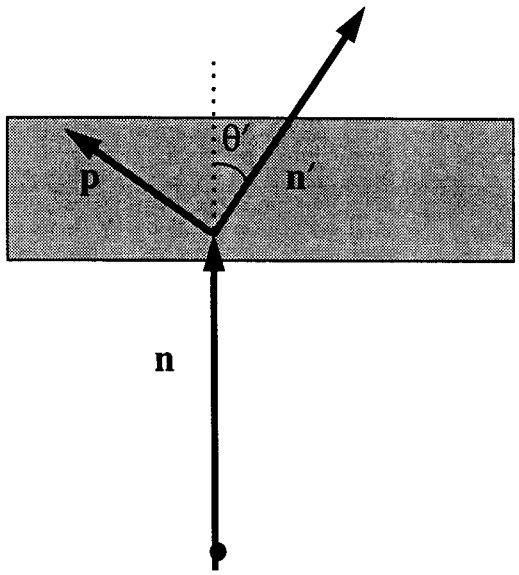

$$E_{n'}=E_n-E_p$$

$$E_{n'}=E_n \cos^2\theta'$$

Figure 4.5 Elastic scattering kinematics, for a neutron scattering from a proton. These formulas are used to calculate the energy and direction, $E_{n'}$ and θ', of the scattered neutron.

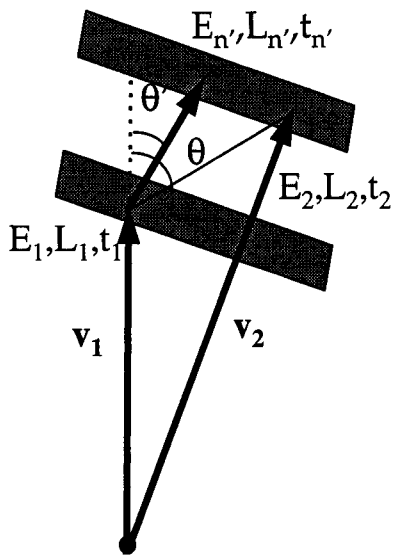

Figure 4.6 The variables involved in the crosstalk correction. $E_{n'}$, $L_{n'}$, $t_{n'}$ are calculated assuming elastic scattering, while the others are measured quantities.

Assuming the mass of the proton and neutron are equal, the calculated energy is $E_{n'} = E_1 - E_p$, where $E_p = E_p(L_1)$ is the energy from the light response. A linear function (Figure 3.19) was used for the light response, so that the crosstalk variables were symmetric around zero.

Various comparisons can be made between the calculated and measured values. Three tests were used to find events with a large probability of being crosstalk, suggested by Reference [Wang 97].

1. The difference between the scattering angle calculated, $\cos\theta'$, for the crosstalk neutron and the measured angle, $\cos\theta$, is restricted to:

$$\Delta C_- < \cos\theta' - \cos\theta < \Delta C_+ .$$

The measured scattering angle is defined as $\cos\theta = \frac{\vec{v}_1 \cdot (\vec{v}_2 - \vec{v}_1)}{|\vec{v}_1||\vec{v}_2 - \vec{v}_1|}$, while the calculated quantity is $\cos\theta' = \sqrt{\frac{E_{n'}}{E_1}}$. The minimum and maximum difference in angles that can be classified as a crosstalk event are defined by ΔC_- and ΔC_+, respectively.

2. The difference between the time needed for the scattered neutron to reach the second detector, $t_{n'}$, and the time between hits, $t_2 - t_1$, is restricted to:

$$\Delta T_- < t_{n'} - (t_2 - t_1) < \Delta T_+ .$$

The calculated time is $t_{n'} = \frac{d_{n'}}{v_{n'}}$, where the distance to be traveled is $d_{n'} = |\vec{r}_2 - \vec{r}_1|$ and the velocity relativistically is calculated as

$v_{n'} = c\sqrt{\frac{E_{n'}(E_{n'} + 2mc^2)}{(E_{n'} + mc^2)^2}}$ and m is the neutron mass. The minimum and maximum difference in time that are classified as crosstalk are ΔT_- and ΔT_+, respectively.

3. The difference between the scattered neutron's energy, $E_{n'}$ and recoil proton energy for the light measured in the second detector, $E_p(L_2)$, is restricted to

$$E_{n'}-E_p(L_2) > \Delta E.$$

ΔE is the minimum proton energy possible for a crosstalk event.

If the neutron could be crosstalk by all three of these criteria, it is excluded from the analysis. The differences in calculated and measured values, $\cos\theta' - \cos\theta$, $t_{n'} - (t_2 - t_1)$, and $E_{n'} - E_p(L_2)$ show a strong correlation from crosstalk (Figure 4.7). The first two criteria peak at zero and the last criterion has a peak at positive values as expected for crosstalk. Two different sets of gates (listed in Table 4.1) have been applied in this figure.

The crosstalk in true coincidences can be compared to the same variables when coincidences are constructed by mixing singles events, which thus have no crosstalk (Figure 4.8). The singles events do not show the sharp peak at zero for the cosine and time criteria, and in the light criterion they do not show a second peak for positive differences. (These peaks are the result of crosstalk.) A two-dimensional plot of the differences in angles vs. the differences in times also shows that the peaks of these criteria exhibit a significant correlation (Figure 4.9) as is expected for crosstalk.

The crosstalk can also be seen in the correlation function. Figure 4.10 shows the integrated correlation function with one neutron in the front wall and one in the back

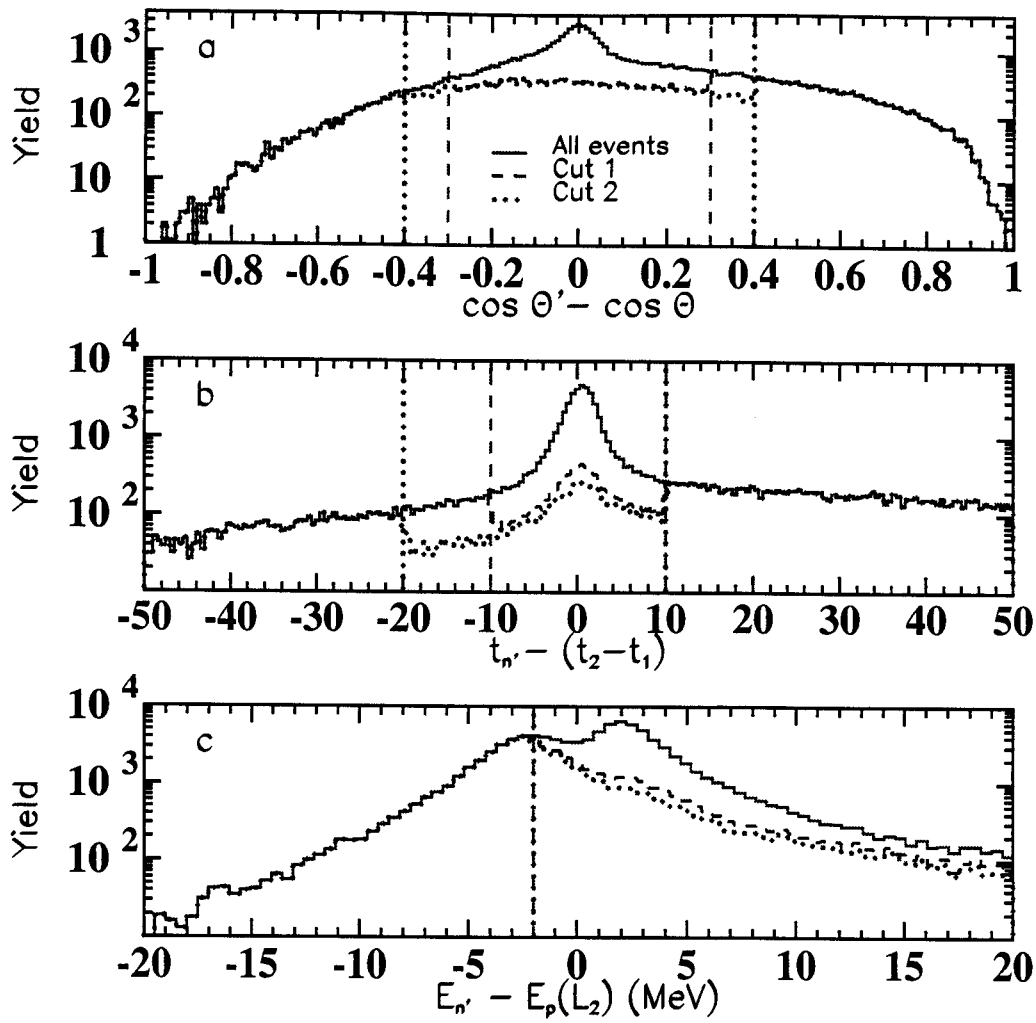

Figure 4.7 Crosstalk criteria. (a) Difference in angles calculated and measured. (b) Difference in time between hits, calculated and measured. (c) Difference in the energy of the scattered neutron and the energy corresponding to the light measured in the second detector. The cuts are shown on the figure and defined in Table 4.1.

Table 4.1 Crosstalk cuts applied to the data. The difference in calculated and measured scattering angles is gated on $\Delta C_- < \cos\theta' - \cos\theta < \Delta C_+$; the difference in the time between hits calculated and measured is gated by $\Delta T_- < t_{n'} - (t_2 - t_1) < \Delta T_+$; the difference in energy deposited in the second detector calculated and measured is gated on $E_{n'} - E_p(L_2) > \Delta E$

Cut	ΔC_-	ΔC_+	ΔT_-	ΔT_+	ΔE
1	-0.3	0.3	-10	10	-2
2	-0.4	0.4	-20	10	-2

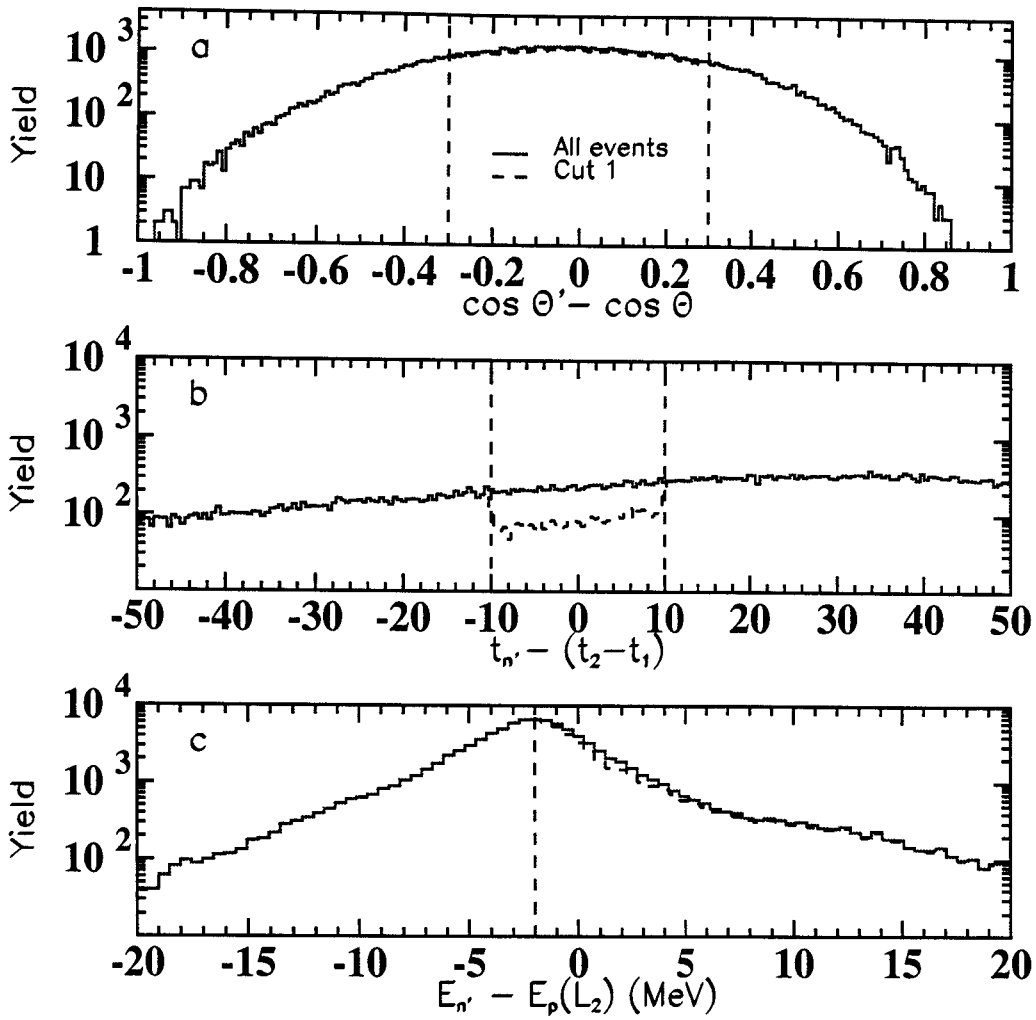

Figure 4.8 Crosstalk criteria constructed from mixed singles where no crosstalk is present. Same variables as Figure 4.7. Cut 1 is shown in this case.

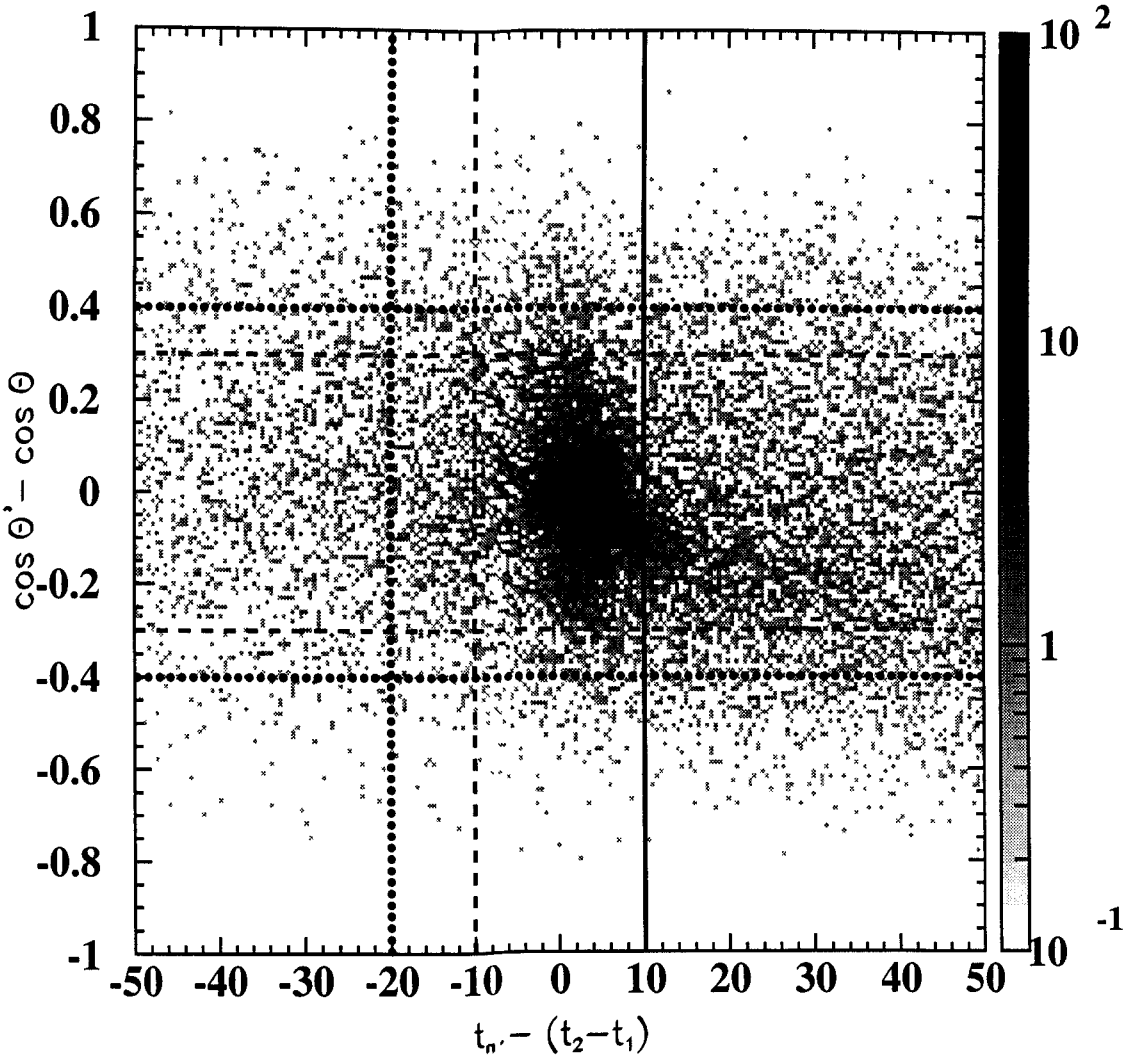

Figure 4.9 Difference between measured and calculated angle versus time between hits for real coincidences. The dashed lines show where the cuts for crosstalk were made for Cut 1 and the dotted lines show Cut 2. The solid line is where both cuts are the same.

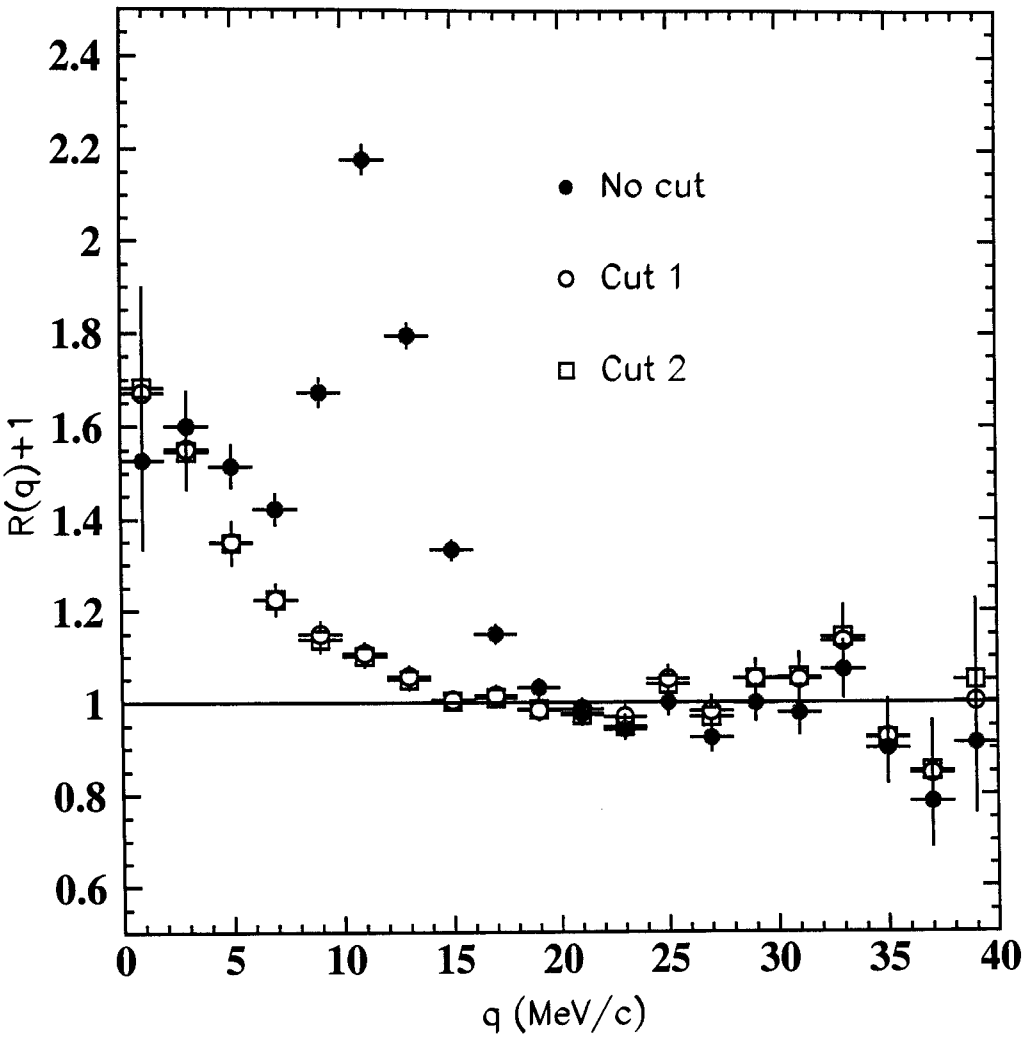

Figure 4.10 The experimental correlation function with and without a crosstalk cut. The neutron pairs have $|\vec{P}| < 250$ MeV/c. The cuts are defined in Table 4.1.

wall. The correlation function is plotted before and after the crosstalk cut is applied. The crosstalk events produce an artificial peak at ~10 MeV/c. One advantage of using detectors at two different distances is that the crosstalk does not peak at q = 0, where the correlation function peaks.

The gates for crosstalk were adjusted by observing the effect on the crosstalk variables, the correlation function, and in the simulations. The gates for the crosstalk must be made so that most of the crosstalk is removed while retaining as many events as possible. The two cuts, shown as examples, both eliminate most of the crosstalk.

The correlation functions in Figure 4.10 are constructed using Cut 1 and also selecting events based on the total momentum of the pair, $|\vec{P}| < 250$ MeV/c. By looking at the correlation function from events above and below this cut, it is possible to see that some crosstalk remains in the higher momentum pairs (Figure 4.11). The lack of statistics for the higher momentum events does not allow further investigation with wider crosstalk gates.

Unfortunately, not all of the crosstalk can be eliminated with this crosstalk method. Some crosstalk neutrons scatter on carbon, or interact more than twice, so that two-body scattering kinematics on hydrogen are not applicable. In the next chapter, the effectiveness of these crosstalk cuts are investigated by comparison with a simulation.

4.2.3 Background Corrections

The experimental correlation function must be corrected for the background scattered neutrons. Figure 3.24 shows that at least ten percent of the measured neutrons

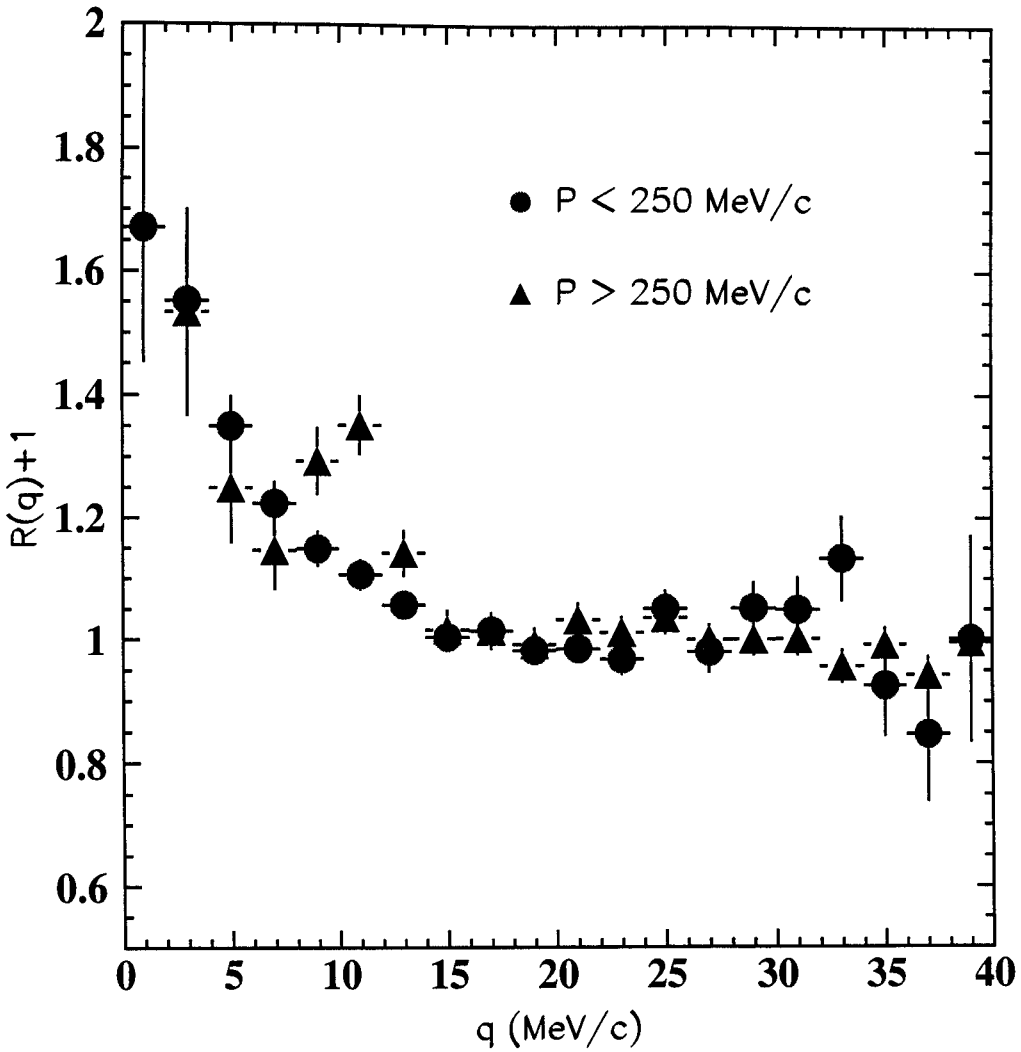

Figure 4.11 The correlation functions cut on total momentum of the neutron pair. Crosstalk Cut 1 was applied to both spectra.

are from background events, even after eliminating the lowest-energy events and cutting on the light measured. These background neutrons add uncorrelated coincidences so that the measured correlation will be smaller than the true correlation for events coming from the target.

If the background events are assumed to be uncorrelated to the real neutrons, it is possible to correct the correlation function for this suppression [Prat 96]. A corrected correlation function can be defined as

$$1 + R'(q) = \frac{\sum N(\vec{p}_1, \vec{p}_2) - \alpha \sum D(\vec{p}_1, \vec{p}_2)(b(\vec{p}_1, \vec{p}_2))}{\alpha \sum D(\vec{p}_1, \vec{p}_2)(1 - b(\vec{p}_1, \vec{p}_2))}.$$

Here the functions $N(\vec{p}_1, \vec{p}_2) = \tilde{Y}_2(\vec{p}_1, \vec{p}_2)$ and $D(\vec{p}_1, \vec{p}_2) = \tilde{Y}_1(\vec{p}_1)\tilde{Y}_1(\vec{p}_2)$ are the numerator and denominator as constructed for the standard correlation function. The denominator in the standard correlation function is a distribution reflecting the geometry and efficiency of the detectors without the correlations of the source. This uncorrelated distribution should be similar to distributions of events that are added by the background scattering. The function $b(\vec{p}_1, \vec{p}_2)$ is the fraction of times that an event measuring neutrons with momenta $\vec{p}_1$ and $\vec{p}_2$ would be a background event. This weighting is applied on an event by event basis. The correction assumes the amount of scattered background in a particular event depends on the detectors hit but is independent of the energy and horizontal position of the neutrons. The opposite function is used to correct the denominator of the corrected correlation function. Here the event is weighted based on the fraction of good events for these detectors. One overall normalization constant is available for the corrected correlation function, chosen as α.

Another way to perform this background correction is to subtract the background from the singles yields before constructing the correlation function. The measured yield of each type of particle, $\tilde{Y}$, is considered to be the real yield, Y, plus a background yield, Y_b. Then the corrected correlation function, 1 + R"(q), can be written as the coincidence yield minus corrections for events with one background and one real neutron and events with two background neutrons.

$$1 + R''(q) = \frac{\sum (AN(\vec{p}_1, \vec{p}_2) - [(\tilde{Y}_1(\vec{p}_1) - Y_{1b}(\vec{p}_1))Y_{2b}(\vec{p}_2) + (\tilde{Y}_1(\vec{p}_2) - Y_{2b}(\vec{p}_2))Y_{1b}(\vec{p}_1)] - Y_{1b}(\vec{p}_1)Y_{2b}(\vec{p}_2))}{\sum (\tilde{Y}_1(\vec{p}_1) - Y_{1b}(\vec{p}_1))(\tilde{Y}_1(\vec{p}_2) - Y_{2b}(\vec{p}_2))}.$$

The normalization constant is A.

This method can be shown to correspond to the first method if functions $f_1(\vec{p}_1)$ and $f_2(\vec{p}_2)$, the fraction of good neutrons in events with this momentum, are defined by $f_1(\vec{p}_1) = 1 - \frac{Y_{1b}(\vec{p}_1)}{\tilde{Y}_1(\vec{p}_1)}$ and $f_2(\vec{p}_2) = 1 - \frac{Y_{2b}(\vec{p}_2)}{\tilde{Y}_1(\vec{p}_2)}$. The denominator of the R" function becomes

$$f_1(\vec{p}_1)\tilde{Y}_1(\vec{p}_1)f_2(\vec{p}_2)\tilde{Y}_1(\vec{p}_2) = g(\vec{p}_1, \vec{p}_2)D(\vec{p}_1, \vec{p}_2),$$

where $g(\vec{p}_1, \vec{p}_2) = 1 - b(\vec{p}_1, \vec{p}_2)$ represents the fraction of events that are good. The correction for one background neutron, can be written as

$$[f_1(\vec{p}_1)\tilde{Y}_1(\vec{p}_1)(1 - f_2(\vec{p}_2))\tilde{Y}_1(\vec{p}_2) + (1 - f_1(\vec{p}_1))\tilde{Y}_1(\vec{p}_1)f_2(\vec{p}_2)\tilde{Y}_1(\vec{p}_2)]$$

$$= \tilde{Y}_1(\vec{p}_1)\tilde{Y}_1(\vec{p}_2)[f_1(\vec{p}_1) - f_1(\vec{p}_1)f_2(\vec{p}_2) + f_2(\vec{p}_2) - f_1(\vec{p}_1)f_2(\vec{p}_2)]$$

$$= D(\vec{p}_1, \vec{p}_2)[f_1(\vec{p}_1) + f_2(\vec{p}_2) - 2f_1(\vec{p}_1)f_2(\vec{p}_2)].$$

The second correction, for two background neutrons, can be written as:

$$[(1 - f_1(\vec{p}_1))\tilde{Y}_1(\vec{p}_1)(1 - f_2(\vec{p}_2))\tilde{Y}_1(\vec{p}_2)]$$

$$= \tilde{Y}_1(\vec{p}_1)\tilde{Y}_1(\vec{p}_2)[1 - f_1(\vec{p}_1) - f_2(\vec{p}_2) + f_1(\vec{p}_1)f_2(\vec{p}_2)]$$

$$= D(\vec{p}_1, \vec{p}_2)[1 - f_1(\vec{p}_1) - f_2(\vec{p}_2) + f_1(\vec{p}_1)f_2(\vec{p}_2)].$$

Combining these terms the numerator will be

$$\sum AN(\vec{p}_1, \vec{p}_2) - \sum D(\vec{p}_1, \vec{p}_2)[1 - f_1(\vec{p}_1)f_2(\vec{p}_2)].$$

Since $[1 - f_1(\vec{p}_1)f_2(\vec{p}_2)] = b(\vec{p}_1, \vec{p}_2)$ this form is the same as that given above with $A = 1/\alpha$. So both corrections, R'(q) and R"(q), will give the same result.

After applying this correction, the correlation function was enhanced by about 10% (Figure 4.12). This method provides an average correction for the correlation function. The background ratios have not been corrected for the neutrons that will reach the detector through the shadow bar or for changes in the background scattering resulting from the shadow bars. The original plan for the experiment was to measure the background spectra $\tilde{Y}_1(\vec{p}_1)Y_{2b}(\vec{p}_2)$ by using small shadow bars, to check the assumption of uncorrelated background, but the statistics which could be collected in the time available were too small.

4.2.4 Singles vs. Mixed-Events Technique

In previous studies two methods for creating the denominator have been used [Zajc 84, Lisa 93b (p105)]. The first is to mix neutrons from different coincidence events and so create an uncorrelated function for the denominator [Troc 87, Fox 88, Cebr 89, DeYo 89]. This technique requires only coincidence measurements, and it ensures that the denominator and numerator both come from the same class of events. The second

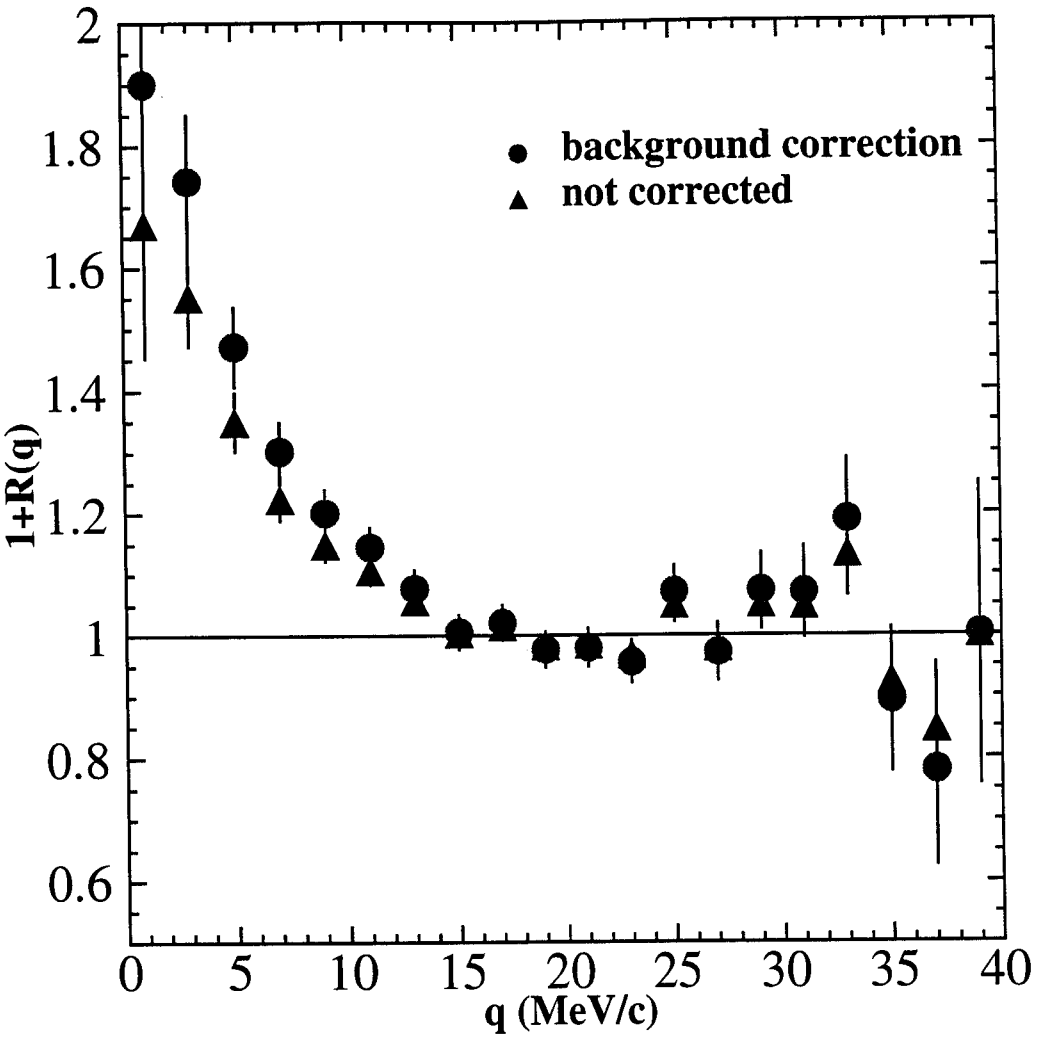

Figure 4.12 The correlation function corrected for background scattering (circles). The uncorrected correlation function is shown for comparison (triangles). (Both have $|\vec{P}| < 250$ MeV/c and crosstalk Cut 1 applied.)

technique is to use singles events[Lync 83, Chit 85, 86, Poch 85a, 85b, Chen 87, Awes 88, Ghet 93]. Here particles from events where one particle is measured are combined to construct the denominator.

For two-neutron correlation functions, an ambiguity exists in how to treat crosstalk events in a mixed-event analysis. When an event has been identified as crosstalk, what should happen to it? Both neutrons could be mixed with the rest, only the "real" neutron included, or the whole event excluded. If the crosstalk is not removed, neutrons that do not come from the target are included. However, if some events are excluded before the events are mixed an inefficiency that depends on the momentum of both particles is introduced.

The effect of this crosstalk cut on the correlation function can be seen by considering how the correlation function is made. Inefficiencies in the detectors cause the measured singles, $\tilde{Y}_1(\vec{p})$, and coincidence yields, $\tilde{Y}_2(\vec{p}_1, \vec{p}_2)$, to differ from the true yields. By constructing a ratio of correlated to uncorrelated events with the appropriate conditions these differences will divide out. The usual case is when the coincidence yield is measured with some efficiency factor, $\varepsilon(\vec{p}_1, \vec{p}_2)$. The coincidence yield is then

$$\tilde{Y}_2(\vec{p}_1, \vec{p}_2) = Y_2(\vec{p}_1, \vec{p}_2)\varepsilon(\vec{p}_1, \vec{p}_2).$$

In the mixed event technique pseudo-singles are constructed from the coincidence events.

$$\tilde{Y}_1(\vec{p}_1) = \int \tilde{Y}_2(\vec{p}_1, \vec{p}_2)dp_2 = \int Y_2(\vec{p}_1, \vec{p}_2)\varepsilon(\vec{p}_1, \vec{p}_2)dp_2,$$

similarly

$$\tilde{Y}_1(\vec{p}_2) = \int \tilde{Y}_2(\vec{p}_1, \vec{p}_2)dp_1 = \int Y_2(\vec{p}_1, \vec{p}_2)\varepsilon(\vec{p}_1, \vec{p}_2)dp_1.$$

From these yields, the measured correlation function was constructed:

$$\tilde{C} = \frac{\sum \tilde{Y}_2(\vec{p}_1, \vec{p}_2)}{\sum \tilde{Y}_1(\vec{p}_1)\tilde{Y}_1(\vec{p}_2)} = \frac{\sum Y_2(\vec{p}_1, \vec{p}_2)\varepsilon(\vec{p}_1, \vec{p}_2)}{\sum \int Y_2(\vec{p}_1, \vec{p}_2)\varepsilon(\vec{p}_1, \vec{p}_2)dp_1 \int Y_2(\vec{p}_1, \vec{p}_2)\varepsilon(\vec{p}_1, \vec{p}_2)dp_2}.$$

In order for this correlation function to be equal to the real correlation function,

$$C = \frac{\sum Y_2(\vec{p}_1, \vec{p}_2)}{\sum Y_1(\vec{p}_1)Y_1(\vec{p}_2)},$$

two assumptions must be true:

1. Efficiency depends only on the individual momenta.

$$\varepsilon(\vec{p}_1, \vec{p}_2) = \varepsilon_1(\vec{p}_1)\varepsilon_2(\vec{p}_2)$$

2. Pseudo singles are proportional to real singles.

$$Y_1(\vec{p}_2) \propto \int Y_2(\vec{p}_1, \vec{p}_2)\varepsilon_1(\vec{p}_1)dp_1$$

In the case of neutrons these assumptions cannot be made. The first assumption is especially a problem because the efficiency function is not separable. The crosstalk cuts depend on the combination of $\vec{p}_1$ and $\vec{p}_2$.

The singles technique allows the calculation of the real correlation function from the measured yields. Corrections to the correlation function necessary to remove crosstalk events are applied to both the numerator and denominator. With similar notation this can be written as

$$\tilde{C} = \frac{\sum \tilde{Y}_2(\vec{p}_1, \vec{p}_2)g(\vec{p}_1, \vec{p}_2, \vec{r}_1, \vec{r}_2)}{\sum \tilde{Y}_1(\vec{p}_1)\tilde{Y}_1(\vec{p}_2)g(\vec{p}_1, \vec{p}_2, \vec{r}_1, \vec{r}_2)}$$

$$= \frac{\sum Y_2(\vec{p}_1, \vec{p}_2)\varepsilon_1(\vec{p}_1)\varepsilon_2(\vec{p}_2)g(\vec{p}_1, \vec{p}_2, \vec{r}_1, \vec{r}_2)}{\sum Y_1(\vec{p}_1)\varepsilon_1(\vec{p}_1)Y_1(\vec{p}_2)\varepsilon_2(\vec{p}_2)g(\vec{p}_1, \vec{p}_2, \vec{r}_1, \vec{r}_2)}.$$

Since $Y_2(\vec{p}_1, \vec{p}_2) = CY_1(\vec{p}_1)Y_1(\vec{p}_2)$, if the correlation function, C, varies slowly over this range, it can be factored out and the sums cancel.

Because the mixed-events technique is not valid in this case, a singles technique was used. The problem of treating crosstalk remains if events with multiplicities greater than one are included in the sample. So the denominator was constructed with n = 1 singles. The multiplicity-one events occur about a factor of 30 more often, so the effect of neglecting the coincidence events should be small.

4.2.5 Front-Wall Pairs

The experimental correlation functions shown so far (Figure 4.10, Figure 4.11, and Figure 4.12) were constructed from events with one neutron in each wall. Coincidences were also measured when two neutrons were in the same wall. Two hits in the front wall are more frequent than two hits in the back wall because of the larger solid angle and because the neutron flux is attenuated by the front wall.

Neutrons measured in the same wall have some disadvantages compared to neutrons in different walls. Because of finite detector size, neutrons must hit different detectors and so have at least some minimum relative momentum. Also, the crosstalk correction for front-front pairs is less accurate because the angle between hits is not measured. As a limiting case, the angles are calculated by assuming the first hit occurs at the front face of the detector, and the second hit occurs at the back of the detector. Then the same crosstalk technique is applied for these pairs. The gates are less effective and must be adjusted again for front-front pairs ($\Delta C_+ = 0.7$, $\Delta C_- = -0.3$, $\Delta T_+ = 10$ ns, $\Delta T_- = -10$

ns, ΔE = -2.0 MeV). The biggest disadvantage for same-wall events is that the crosstalk peaks at zero relative momentum just where the correlation function peaks.

The correlation function for front-front pairs is compared to front-back pairs in Figure 4.13. The shape of the front-front correlation function is similar to that measured for the front-back pairs. The difference in sensitivity to low q values can be seen in this plot.

4.3 Longitudinal and Transverse Correlations

In order to distinguish between source size and lifetime, a cut can be made on the direction of q relative to the total momentum of the pair in the source reference frame. The source velocity is assumed to be the velocity of the center of mass of the system v/c = 0.045. After this source correction, the longitudinal, $\Psi < 60°$, and transverse, $\Psi > 80°$, correlation functions are constructed. The cuts for front-back pairs are inconclusive but are consistent with no separation between longitudinal and transverse directions (Figure 4.14).

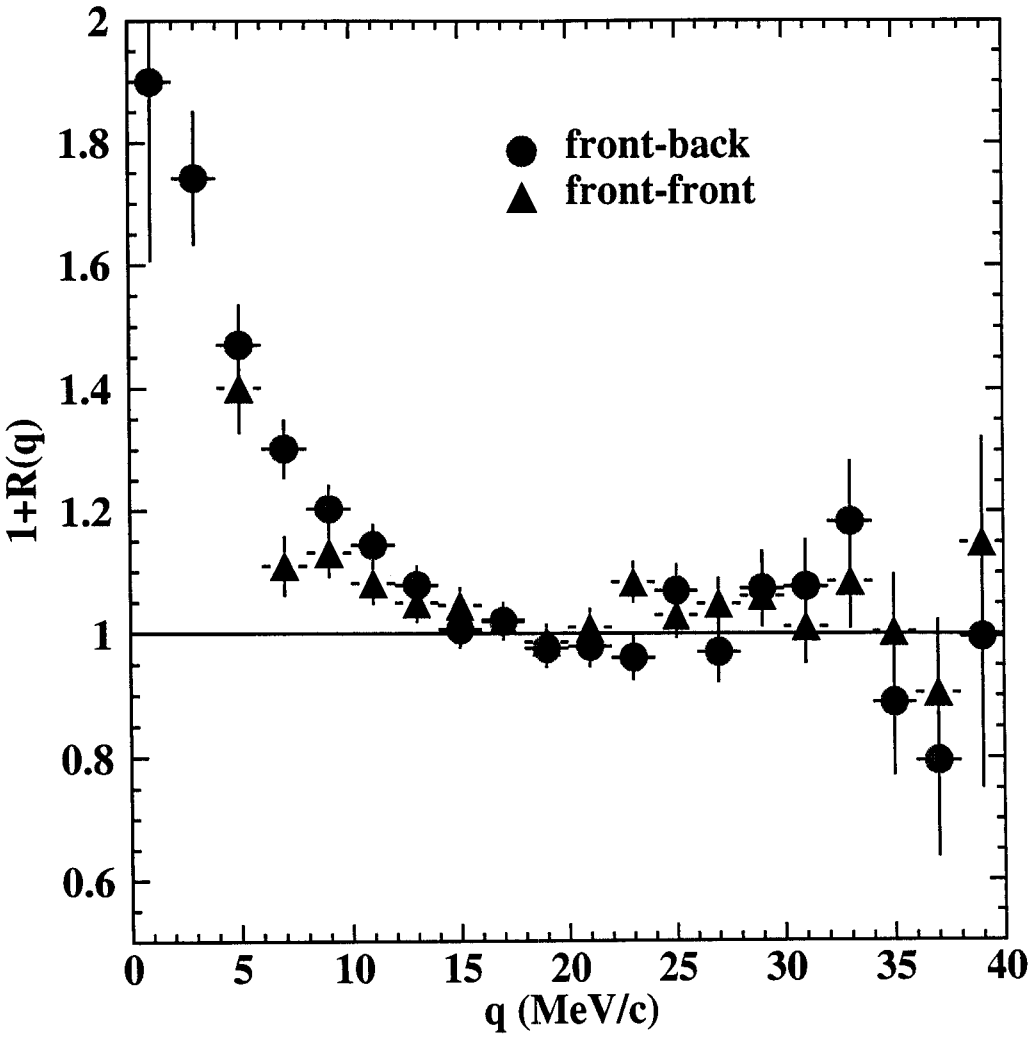

Figure 4.13 Correlation functions for front-front pairs (triangles) and front-back pairs (circles). Both are corrected for background and have $|\vec{P}| < 250$ MeV/c. Cut 1 is applied to the front-back pairs and the cut described in the text applied to the front-front pairs.

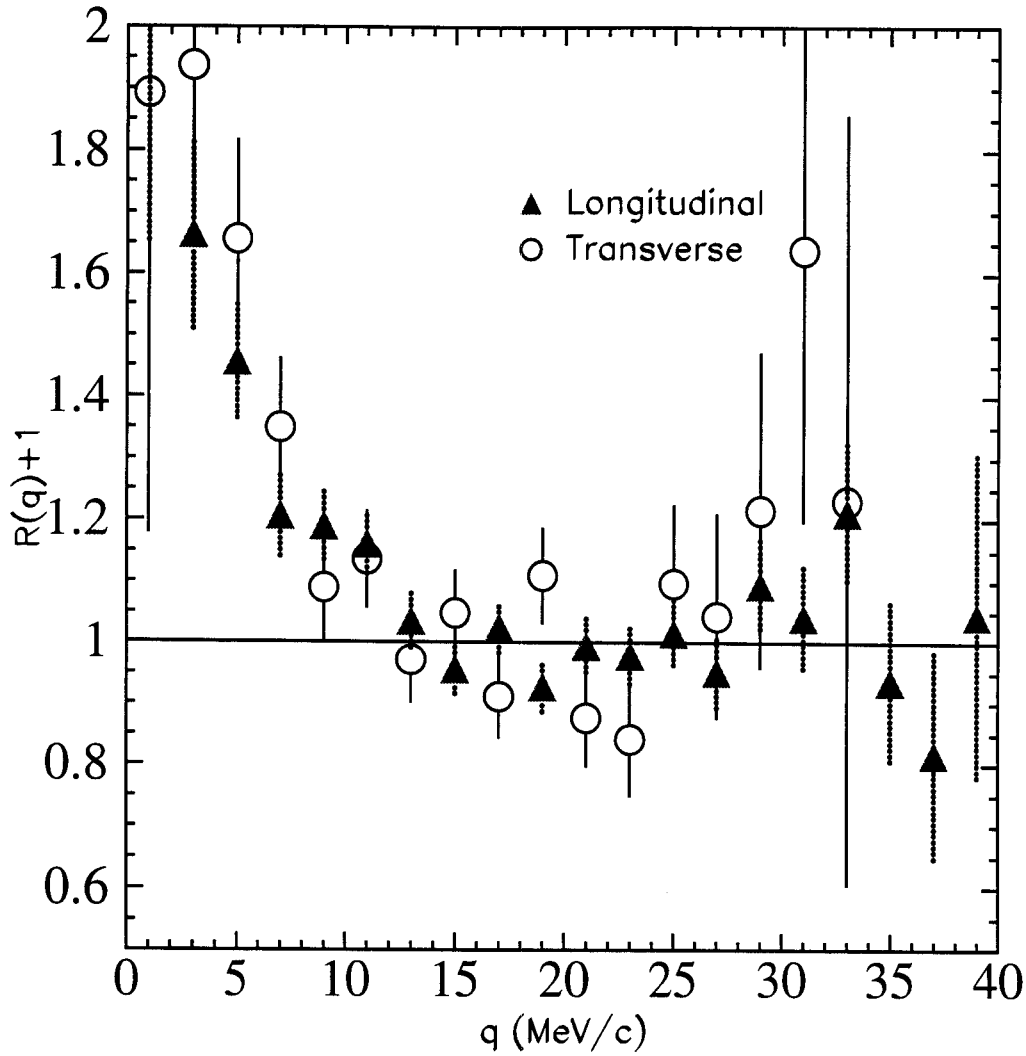

Figure 4.14 Longitudinal and transverse two-neutron correlation functions with $|\vec{P}| < 250$ MeV/c.

Chapter 5 - Two-Neutron Intensity Interferometry: Model Simulations of Detector Response

5.1 Description of Models

Constructing a correlation function for neutrons requires many corrections, as described in the previous chapter. In order to assess how effective these corrections are, and what distortions they might introduce into the results, a simulation which includes the detector response is necessary. Simulations can be especially useful in studying crosstalk and detector efficiency.

Two different simulation programs were used to model this experiment. One program was developed at Michigan State University by Wang et al. [Wang 97] specifically to model crosstalk in the Neutron Walls. The other model, GEANT from the CERN library software, is designed for general detector simulation and has been applied to this specific detector. Both models are based on Monte Carlo principles. For a given event some number of neutrons are initialized: each neutron is given an initial energy and direction. The neutrons are propagated through the detector by small steps. At each step, random numbers are used to sample probability distributions which describe the cross sections for various neutron interactions. After all the steps are completed for all neutrons, the result is compared to some criterion such as whether two detectors registered a neutron interaction. If the event matches this criterion its properties are recorded for further study.

5.1.1 Neutron Interactions

A key element in the simulations is how the neutrons interact in the scintillator. Neutrons can interact with the scintillator by several mechanisms, each with its own partial cross section. For each interaction, the energy deposited must be converted to the amount of light that would be measured by the photo-multiplier tubes, PMTs, and any scattered neutrons must continue to be tracked to see if they interact again somewhere else in the Neutron Walls.

The NE-213 scintillator is made up of hydrogen and carbon. The neutrons can interact with these elements by one of six possible mechanisms, listed in Table 5.1 [Wang 97, Ceci 79]. The energy-dependent cross section for an interaction determines how often that particular event occurs. For illustration, the cross sections for a 24 MeV neutron are given in Table 5.1. Figure 5.1 shows the energy dependence of the neutron interaction with hydrogen and carbon. The first two mechanisms have the largest cross sections and account for most interactions for low energy neutrons. The other mechanisms become more probable at higher neutron energies.

When an interaction occurs in the scintillator, the amount of light produced must be calculated. The simulation determines what kind of interaction has occurred, for example, elastic scattering on a proton. Then the energy of the proton is dissipated in the detector. Both simulations model this process by propagating the proton by small steps until it stops in the scintillator. At each step the energy lost by the proton is converted into light by a light response function. Each particle that excites the scintillator has its own light response (Figure 5.2). The curves used in the simulation come from fits to the data

Table 5.1 Possible interactions between a neutron and the scintillator. For illustration, cross sections for the reaction, σ_R, are given for a 24 MeV neutron [Wang 97].

	INTERACTION	σ_R (24 MeV)
1	$n + p \rightarrow n + p$	0.406 b
2	$n+C \rightarrow n + C$	0.900 b
3	$n+C \rightarrow n' + C + \gamma(4.44\ MeV)$	0.104 b
4	$n+C \rightarrow He + Be - 5.71\ MeV$	0.048 b
5	$n+C \rightarrow n + 3\alpha - 7.26\ MeV$	0.210 b
6	$n+C \rightarrow p + B - 12.59\ MeV$	0.100 b

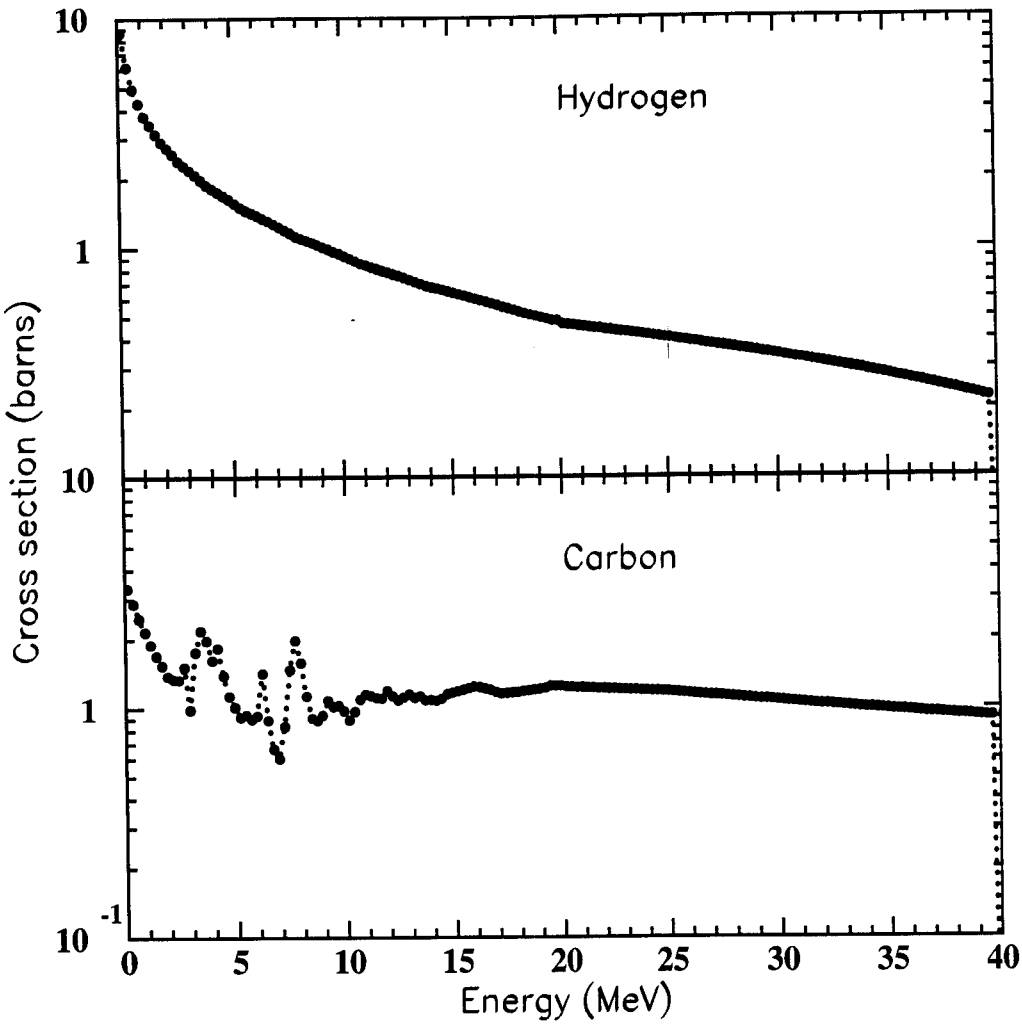

Figure 5.1 GEANT total cross-sections for neutrons scattering on hydrogen and on carbon as a function of the neutron energy.

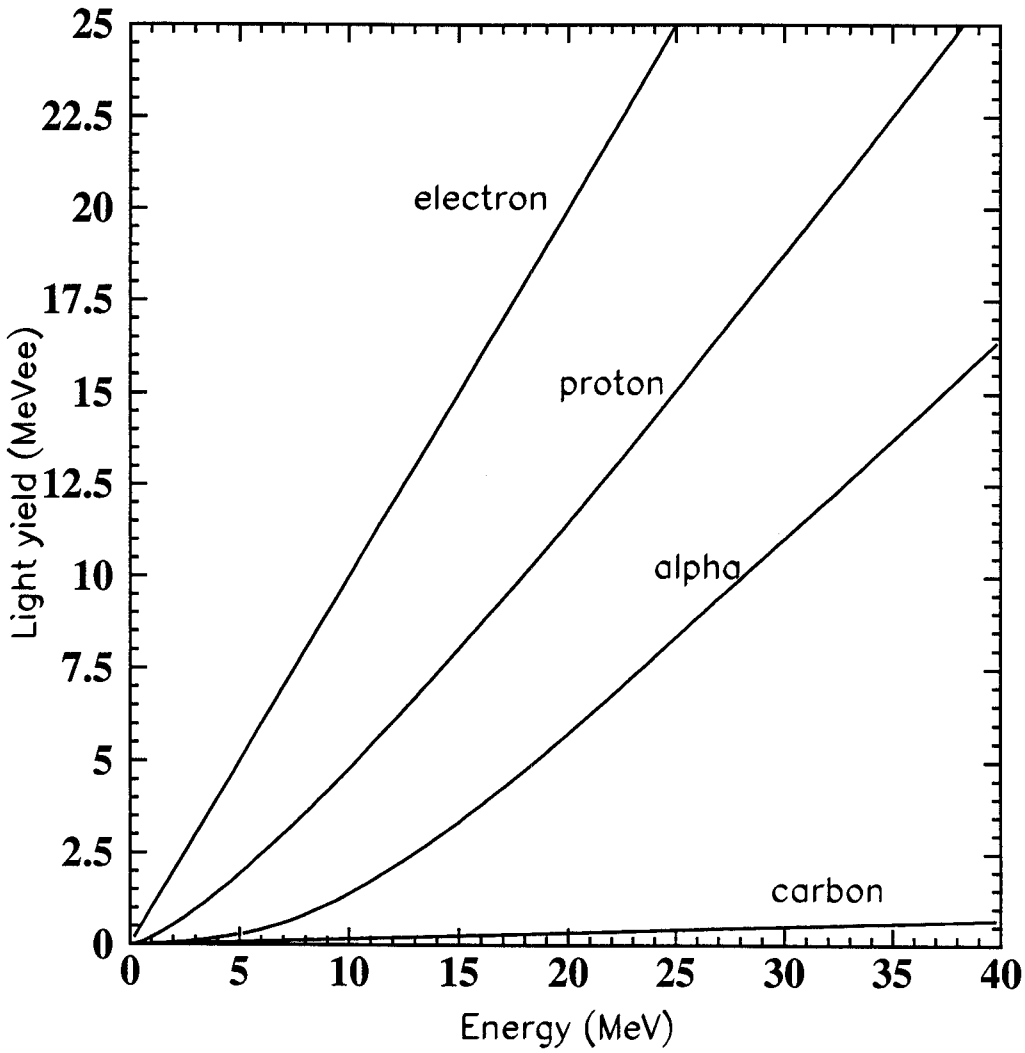

Figure 5.2 Light response for electrons, protons, alphas, and carbons. These response curves are fits to the data from Verbinski [Verb 68, Wang 97]. The light is measured in MeV electron equivalent, the light produced by a 1 MeV electron.

from Reference [Verb 68] of the form given in Table 5.2. The light deposited in the detector is accumulated over all the steps until the particle stops. At the step when the light exceeds the light threshold, L_{th}, the time and position of the interaction are recorded.

The probability of a neutron being detected by a certain mechanism is a combination of the cross section and the light response for that mechanism. Since the protons have the largest light response, and Mechanism #1 has a large cross section, the low energy neutrons in this reaction are most likely to be detected by this mechanism. Some of the interactions which produce alphas, Mechanism #5, exceed the experimental light threshold of 1 MeVee. However, those interactions which have carbon in the final state, Mechanism #2, do not produce enough light to be detected. Neutrons that interact by Mechanism #3 produce a gamma which can be eliminated by pulse-shape discrimination.

After an interaction, any neutrons that remain continue to be tracked to see if they interact again in any other detectors. These scattered neutrons can produce crosstalk events.

5.1.2 Neutron Initialization and Detector Response

Besides the physics of the neutron interactions, other quantities dependent on this experiment are also included in the simulations. The initial neutron energy spectra, the detector resolution, and the light threshold must all be incorporated in a reasonable way.

The neutrons were initialized with values consistent with the measured results. The energy of each initial neutron is chosen from a two-component exponential

Table 5.2 Parameters used to model the light response. These values were determined from a fit of the data given in [Verb 68] with the function $L = a\,(1-\exp(b\,E^c)) + d\,E + f$.

particle	a	b	c	d	f
proton	-5.6375	0.115	0.838	0.7875	0.015
alpha(>5 MeV)	-6.1643	-0.001	2.2	0.01585	0.0
alpha(>5 MeV)	-5.2688	0.0872	1.22	0.543	0.0
Carbon	0.0	0.0	0.0	0.017	0.0

distribution. This distribution was chosen so that the experimental singles spectrum for the front wall is reproduced by the same spectrum from the simulation. The initial neutron direction was chosen isotropically in the direction of the Neutron Walls.

Both simulations determine when a neutron is detected based on a light threshold. This threshold is applied to both the left and right light signals. The total light, L, is determined from the light response curve. Then the light measured at the left and right PMT is calculated by: $L_L = L\exp(-x/\lambda)$ and $L_R = L\exp(-(d-x)/\lambda)$, where the position x is defined from the left side of the cell as in Figure 3.18. The attenuation length used is λ = 226.8 cm. The value of λ affects the position dependence of the threshold (Figure 5.3).

Information is recorded for each detected neutron, including the original momentum of the particle, the final time and position of the hit, the total light, and if the neutron has already interacted in another detector. The position and time of interaction are defined at the time when the total amount of light measured becomes greater than the light threshold. The light is recorded after all interactions have been completed.

The models simulate detector resolution by adding a number sampled from a Gaussian distribution to the measured signals. The widths of these distributions were determined from the data and their values are listed in

. The time resolution was applied to the measured time of neutron detection. In the experiment, the position resolution in x is related to the time resolution and the geometry of the cell. In the simulations, all of these effects were combined into one width, σ_x. The y and z dimensions are constants assigned based on the cell where the interaction occurred. The light resolution, σ_L, is proportional to the number of photons detected in

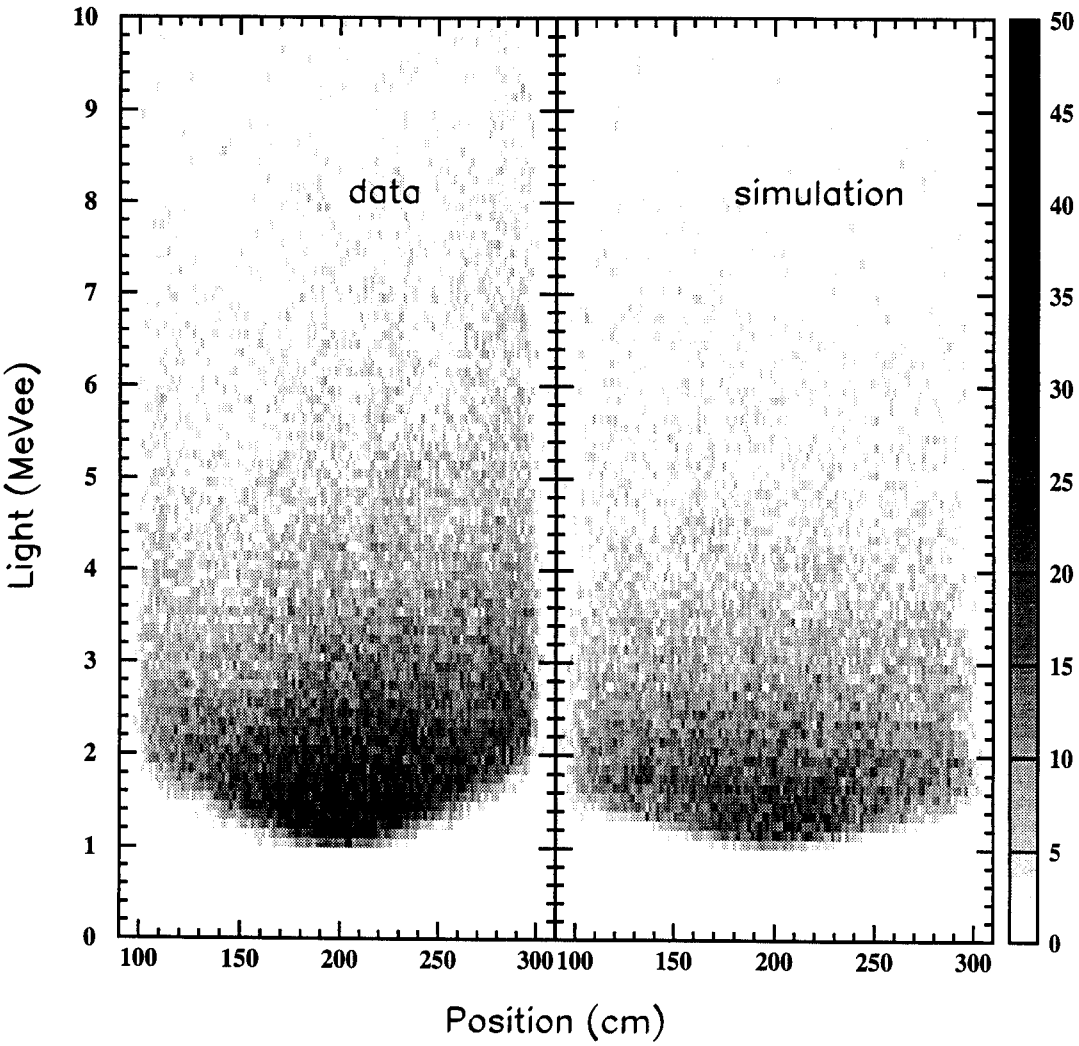

Figure 5.3 Position of the interaction in the cell versus the measured light signal. A light threshold of 1 MeVee at the left and right PMT is applied in both the data and the simulation.

Table 5.3 Detector resolution for time, position, and light, used as input in models. The resolution is assumed to be Gaussian with this standard deviation.

	Standard deviation of Gaussian (σ)
time resolution	$\sigma_t = 0.5$ ns
position resolution	$\sigma_x = 5$ cm
light resolution	$\sigma_L = LR_{LT}\sqrt{\frac{L_T}{L}}$, $R_{LT} = 0.1$

the PMT, N, which is proportional to $\sqrt{L}$. So for a measured light intensity, L_i, the light resolution can be determined from the light resolution at threshold, R_{LT}, by the formula $\sigma_L = L_i * R_{LT} * \sqrt{L_T / L_i}$, where L_T is the light threshold. This resolution is applied to the left and right light signals. The light recorded is the geometric mean of the left and right light signals after the resolution has been applied.

5.1.3 GEANT Simulation Code

One model used was GEANT, the Detector Description and Simulation Tool from the CERN libraries. It was originally designed for high-energy experiments, but has been modified to be applicable for lower-energy experiments [GEAN 93]. The simulation code includes all of the routines for particle tracking. The user defines the detector geometry and the initializes the incident particles and then the GEANT code propagates the particles. At each step the user can access the information about the position and energy of particles in the simulation. If the incident particle interacts with other particles, information about those particles is also available. The user must define what results should be recorded and in what format.

In order to use the appropriate cross sections for low-energy neutron interactions, specific libraries must be used. The low-energy (E < 20 MeV) neutron cross sections are sampled from the MICAP package (A Monte Carlo Ionization Chamber Analysis Package). Cross sections for energies greater than 20 MeV are defined by the FLUKA routines. The total cross sections used for neutrons incident on protons and carbon are shown in Figure 5.1.

The detector geometry must be defined by the user. The cells are defined as boxes with dimensions the size of the cells, 7.62 cm x 6.35 cm x 200 cm and filled with a material defined by an atomic ratio of H/C = 1.212 and a density of 0.874 g/cm^3. The cells are located in a larger volume of air with a size of 300 cm x 300 cm x1200 cm. The coordinate system is defined so that the origin is the source of the particles, and the two walls made of cells are located at z = 400 cm and 500 cm perpendicular to the z axis.

In this model many events were simulated. For each event either one or two neutrons were initialized and the neutrons and any particles they interact with were tracked by the code. When all particles have stopped or have escaped from the air-volume, the event ends.

5.1.4 Wang Simulation Code

The other code we used was written specifically for the Neutron Walls [Wang 97]. This Monte Carlo simulation was based on a previous code [Ceci 79], but it includes the most recent cross section data from the National Nuclear Data Center (NNDC).

The Wang code varies from the GEANT code in a couple of ways. First, it includes the Pyrex cells in the calculations. Neutrons can interact with the Pyrex, but these interactions do not produce any light. Another difference is that this code specifically tracks the neutrons first into the front wall and then into the back wall. This algorithm does not consider the rare occurrence of backscattering from the back wall into the front wall.

Several changes to this code were implemented in order to make it more applicable to this experiment and easier to use. Technical changes included explicitly defining the variables in the FORTRAN code and modifying the output to write n-tuples for analysis with the CERN library code, PAW. A different random number generator was also used for sampling. Because of the large number of random numbers used in this code and the large number of events simulated, a random number generator with a long period was required.

A couple of implementation changes were also made. First, the light threshold for neutron detection was applied to left and right signals. Originally the threshold was just applied to the total light, and so did not simulate the position dependence of the threshold. Also the definition of the recorded time was changed. The original code recorded the last time any energy was deposited in a detector, while the modified code records the time when the light in the detector exceeds the threshold. In many cases this is a small change, but sometimes the proton takes a long time to lose the last bit of energy, and this extends the measured time by a significant amount.

This simulation was designed to model one or two initial neutrons. An event consists of the neutrons being initialized, propagated through the first wall, and then propagated through the second wall.

5.2 Simulation Results

5.2.1 Efficiency

One useful result from these simulations is the efficiency of the detector as a function of energy. In order to compare the measured energy spectra to model predictions, this efficiency must be included. For both simulations the efficiency of the front wall was calculated by dividing the measured energy spectra by the initial energy spectra (Figure 5.4). The two simulations show a similar dependence on energy. The efficiency depends on the light threshold, which in this case was 1 MeVee for both the left and right light signals.

5.2.2 Crosstalk

Both simulation codes model the neutron interactions which produce crosstalk. Because the crosstalk in the simulation can be identified, it can be used to study how much crosstalk is present, how well crosstalk elimination methods remove it, and how these methods affect the distribution of real events.

The same method used to eliminate crosstalk in the data was also applied to the simulation (Section 4.2.2). The calculated energy of the scattered neutron, $E_{n'}$, is determined from the energy of the first neutron, E_1, and the proton energy, E_p. The neutron energy E_1 is calculated from the interaction time and the proton energy for the detected light, L_1, from the Verbinski light curve, $E_p = E_p(L_1)$. From these measured

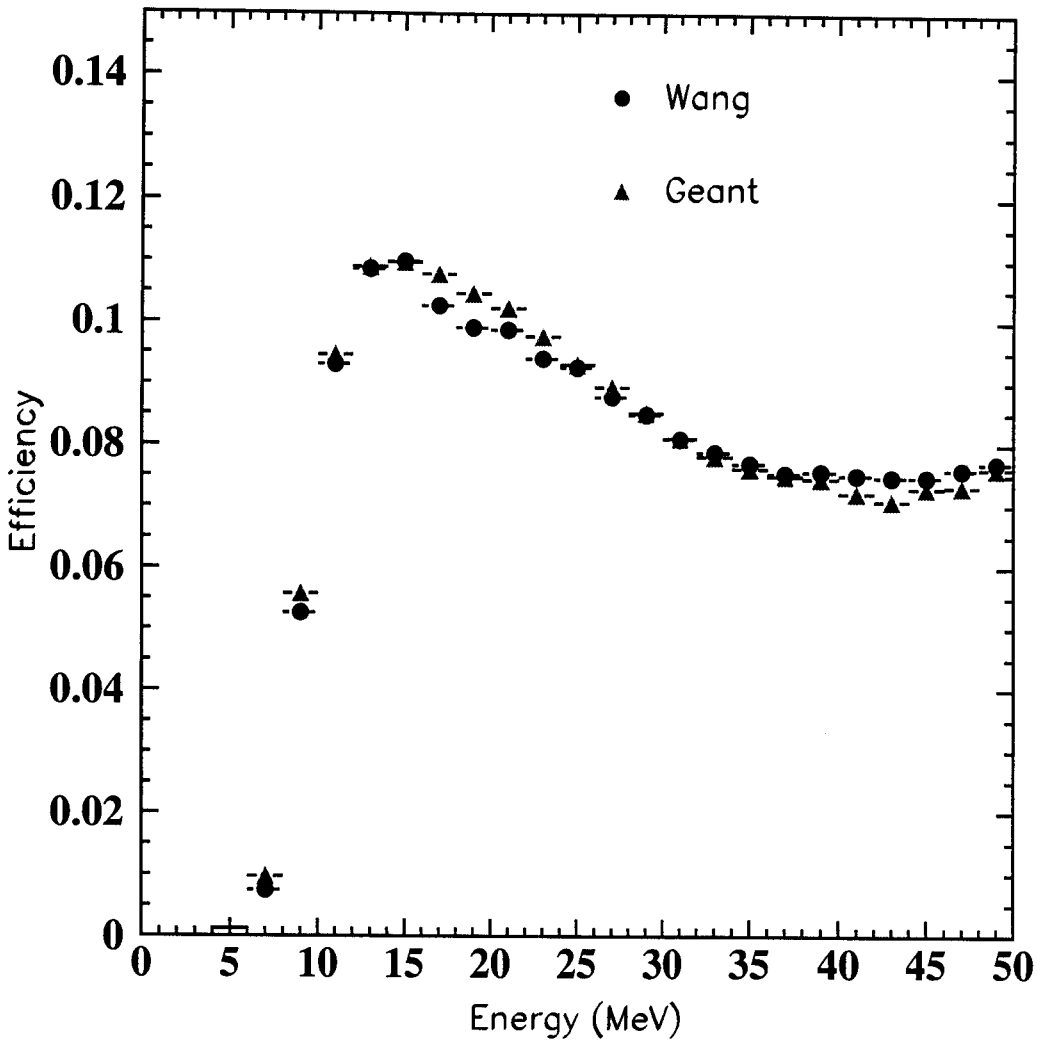

Figure 5.4 Efficiency predicted by Wang and GEANT simulations as a function of neutron energy. The light threshold was set at 1 MeVee for left and right light signals.

quantities $E_{n'} = E_1 - E_p$ is calculated. The same three criteria used with the data are used in the simulation to find the events with a large probability of being crosstalk:

1. The difference between the calculated scattering angle, $\cos\theta'$, and the measured scattering angle, $\cos\theta$, is within the range where crosstalk is expected :

$\Delta C_- < \cos\theta' - \cos\theta < \Delta C_+$.

2. The difference between the calculated time between hits, $t_{n'}$, and the measured time between hits, $(t_2 - t_1)$, within a range close to zero:

$\Delta T_- < t_{n'} - (t_2 - t_1) < \Delta T_+$.

3. The difference between the calculated energy of the scattered neutron, $E_{n'}$, and the minimum energy of the neutron which could deposit the measured light in the second detector, $E_p(L_2)$, indicates that this is a possible crosstalk event:

$E_{n'} - E_p(L_2) > \Delta E$.

Crosstalk events are identified as those where all three criteria are satisfied. These variables from both models look qualitatively like the data (Figure 5.5 and Figure 5.6 compare to Figure 4.7). The crosstalk is evident in peaks centered at zero for the first two criteria, and at a positive value for the third criterion.

In the models, the crosstalk events can be distinguished from the true coincidences. When the crosstalk criteria are plotted only for the events which are crosstalk, the validity of these cuts can be seen (Figure 5.7 and Figure 5.8). For the correlation functions, three different gates were applied to the simulations (Table 5.4). Cuts 2 and 3 are shown in the figures of the crosstalk variables. Note that these cuts are numbered differently than the cuts in Chapter 4.

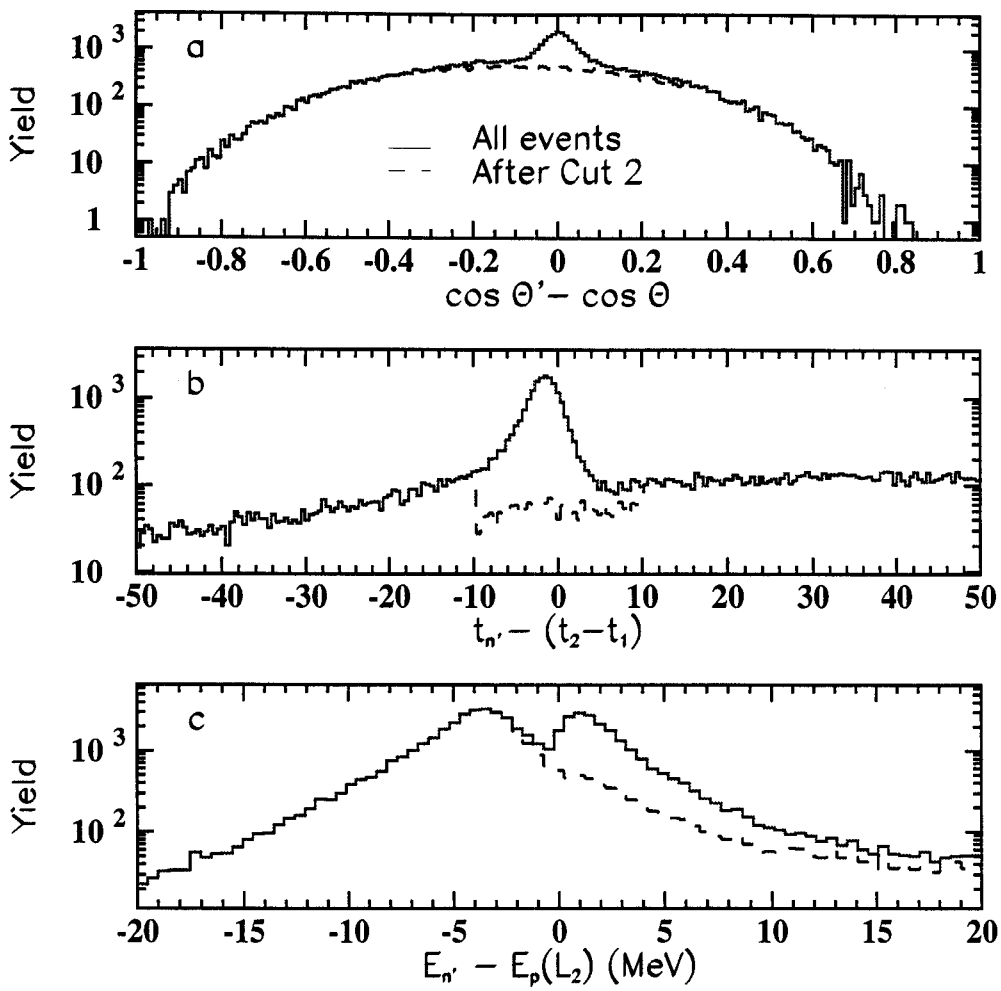

Figure 5.5 Crosstalk criteria for simulations from the Wang model. The solid line is for no crosstalk cut, while the dashed line shows the results after Cut 2 is applied. (a) Difference in angles calculated and measured. (b) Difference in time between hits, calculated and measured. (c) Difference in calculated energy and energy of proton from light measured in the second detector.

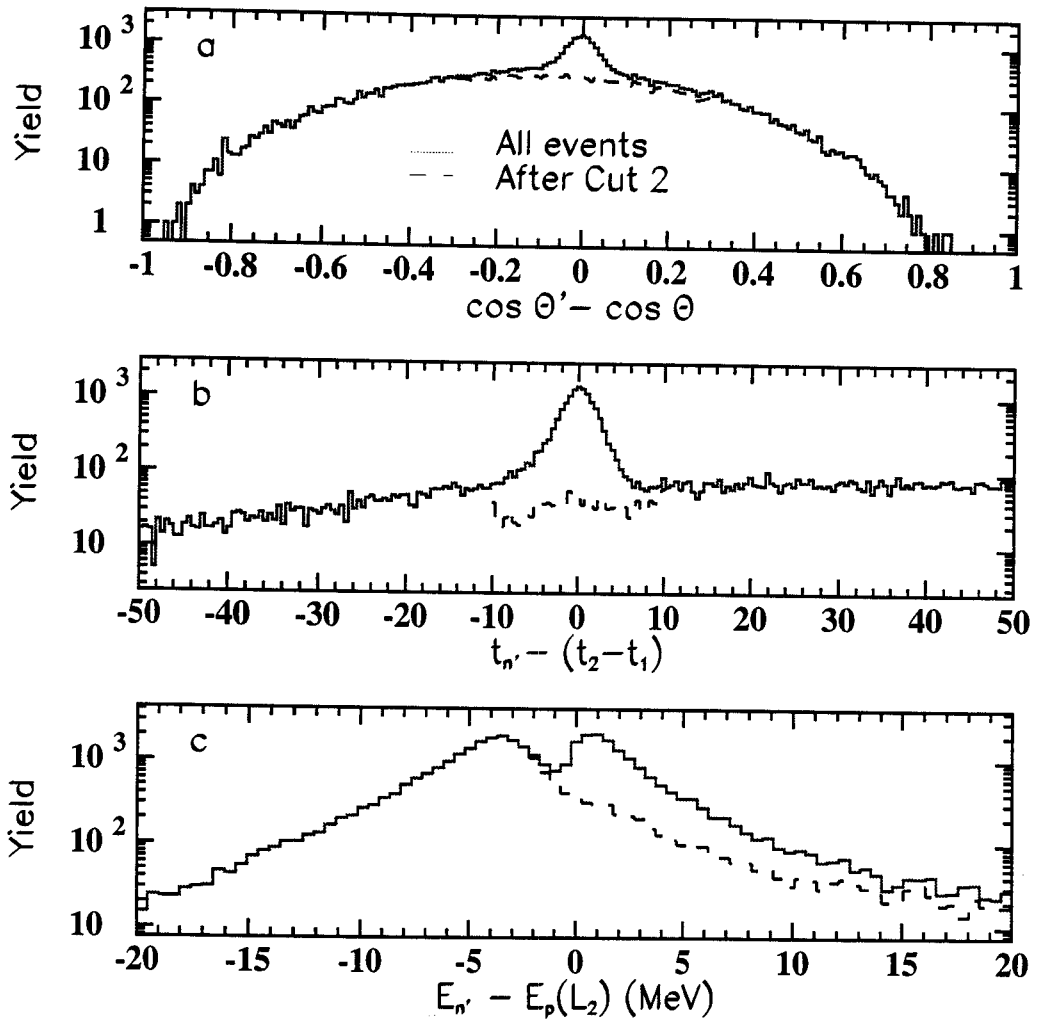

Figure 5.6 Same as Figure 5.5 but from the GEANT model.

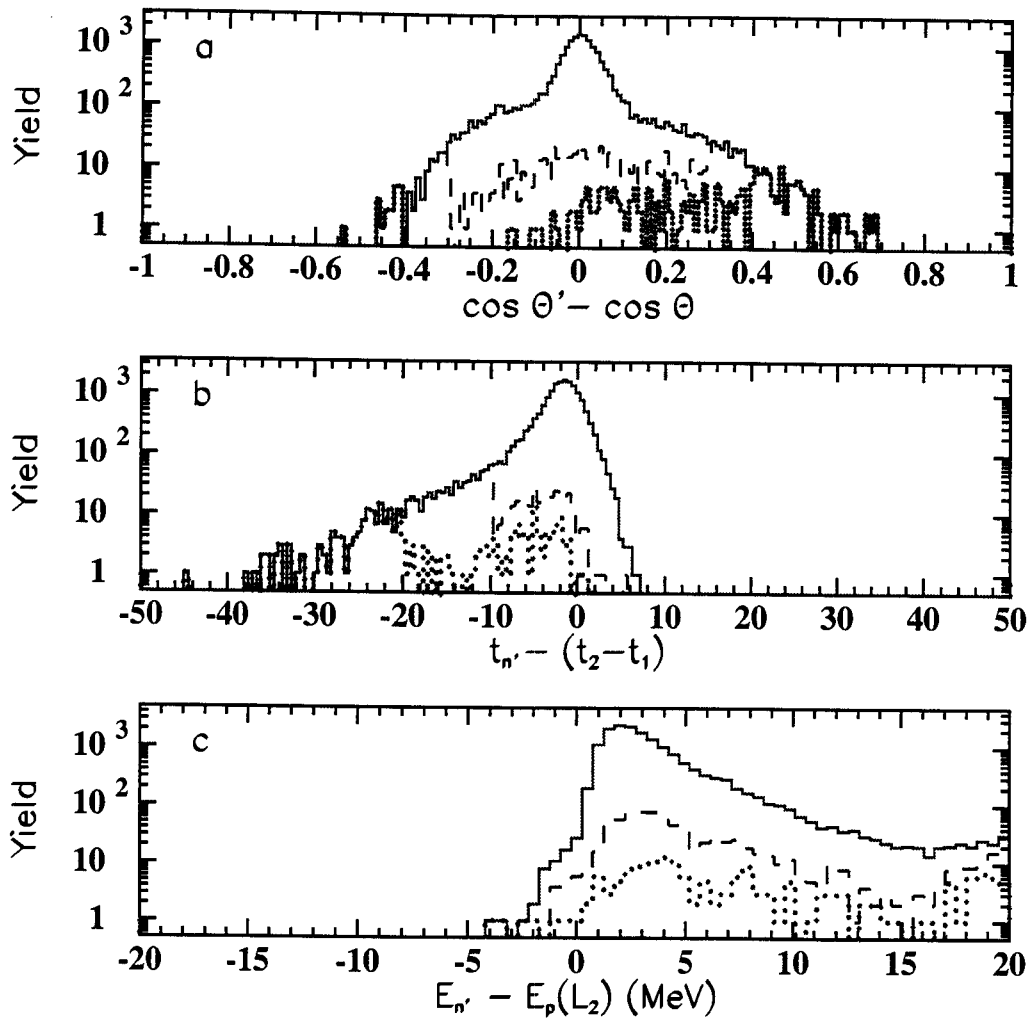

Figure 5.7 Same as Figure 5.5 for events that are crosstalk in the Wang model. The solid line is events with no crosstalk cut, the dashed line is after Cut 2 is applied, and the dotted line is after Cut 3.

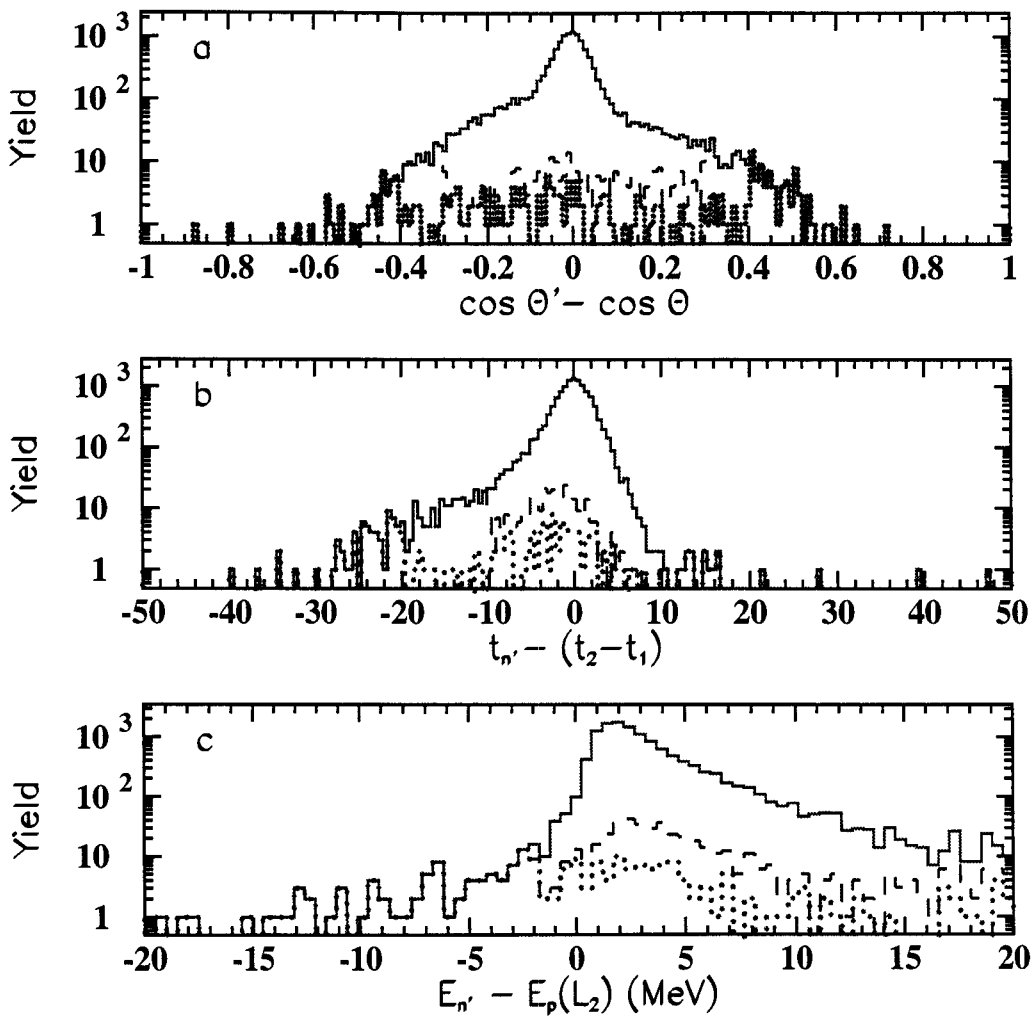

Figure 5.8 Same as Figure 5.7, but for the GEANT model.

Table 5.4 Crosstalk cuts applied for both models. The difference in calculated and measured scattering angles is gated on $\Delta C_- < \cos\theta' - \cos\theta < \Delta C_+$; the difference in the time between hits calculated and measured is gated by $\Delta T_- < t_{n'} - (t_2 - t_1) < \Delta T_+$; the difference in energy deposited in the second detector calculated and measured is gated on $E_{n'} - E_p(L_2) > \Delta E$

Cut	ΔC_-	ΔC_+	ΔT_-	ΔT_+	ΔE
1	-0.1	0.1	-10 ns	10 ns	-2 MeV
2	-0.3	0.3	-10	10	-2
3	-0.4	0.4	-20	10	-2

The fraction of measured coincidences which are crosstalk depends strongly on the total momentum of the neutron pair. The yield of real coincidences decreases with increasing total momentum, $|\vec{P}|$ (Figure 5.9, top panel). At the same time the ratio of crosstalk/total events increases (Figure 5.9, lower panel). Crosstalk events make up a larger part of the coincidences at high momentum because higher-energy neutrons are more likely to measured twice, i.e. to deposit light which will be above threshold in two detectors. Even after applying a crosstalk cut, Cut 2, up to 30% of the remaining events at high total momentum, $|\vec{P}| > 250$ MeV/c, are crosstalk. The momentum dependence of the crosstalk ratio explains why the experimental correlation function with $|\vec{P}| > 250$ MeV/c still shows a peak at 10 MeV/c: crosstalk remains in the numerator (Figure 4.11).

The momentum dependence of the events can be seen in more detail in Table 5.5. The events are divided into two classes defined by $|\vec{P}| < 250$ MeV/c and $|\vec{P}| > 250$ MeV/c. In each class, the number of events is given for a sample run with no crosstalk cut. The number of total, real, and crosstalk events is given for both the Wang and GEANT models. The three crosstalk cuts are applied and the fraction of events remaining is listed for each type of event. As the cuts are made wider, the fraction of crosstalk removed is larger, as is the fraction of the real events removed. The low-momentum events start with five times less crosstalk. For the low-momentum pairs, the gates remove more crosstalk. For example, Cut 2 removes about twice as much of the crosstalk from the low-momentum pairs as from the high-momentum pairs.

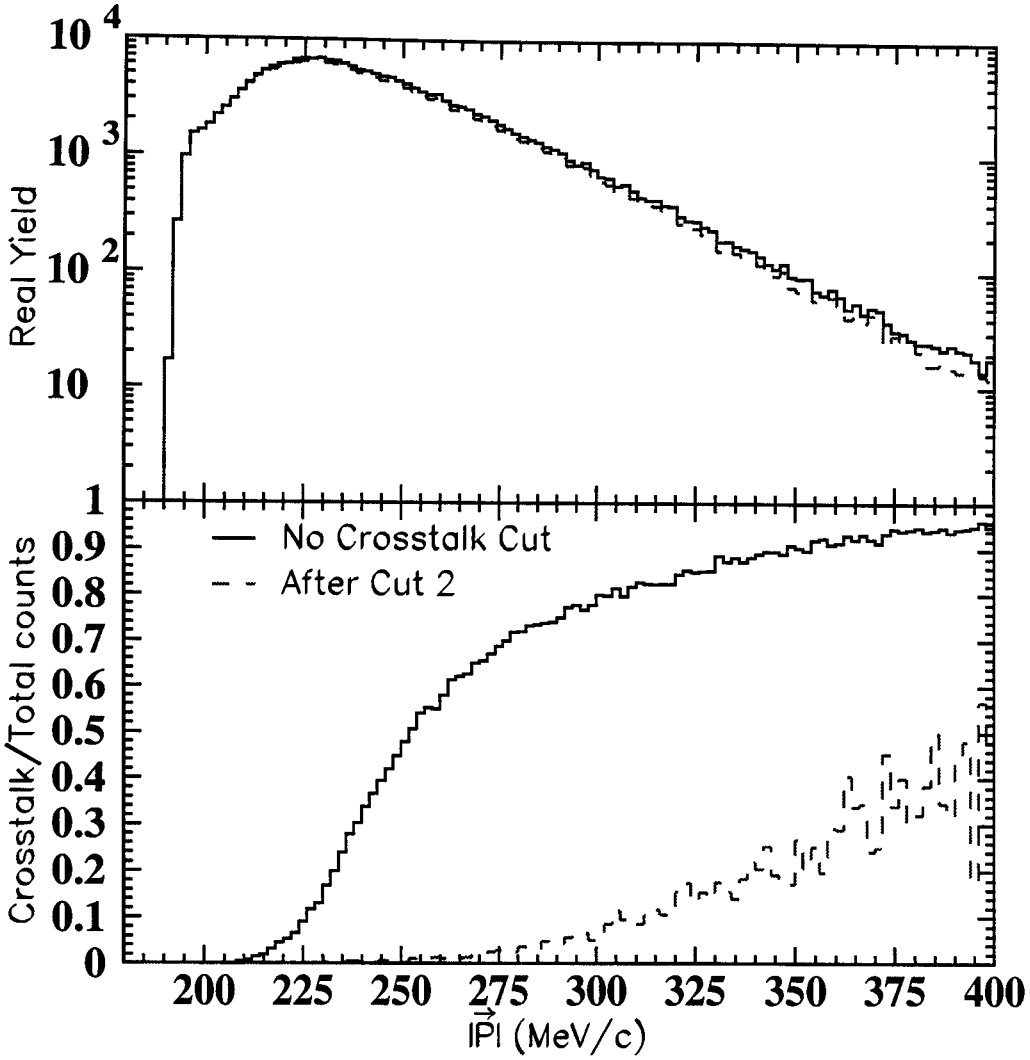

Figure 5.9 Momentum dependence of crosstalk. The top panel shows the real coincidences from two different neutrons before and after Cut 2 is applied. The bottom panel shows the fraction of crosstalk/total events before and after Cut 2 is applied.

Table 5.5 Statistics for two classes of events A. $|\vec{P}| < 250$ MeV/c and B. $|\vec{P}| > 250$ MeV/c. The second column gives the number of events total, real, and crosstalk events in each class for both GEANT and Wang models when no cuts have been applied. The other columns show the ratio remaining in that category after the cut has been applied. The cuts are defined in Table 5.4.

A. $|\vec{P}| < 250$ MeV/c

	No cuts	Cut 1	Cut 2	Cut 3
	#	ratio remaining	ratio remaining	ratio remaining
GEANT all	11649	0.9	0.86	0.84
GEANT real	10506	0.980	0.95	0.93
GEANT crosstalk	1143	0.14	0.03	0.01
Wang all	20659	0.92	0.88	0.85
Wang real	18976	0.98	0.95	0.92
Wang crosstalk	1683	0.19	0.04	0.01

B. $|\vec{P}| > 250$ MeV/c

	No cuts	Cut 1	Cut 2	Cut 3
	#	ratio remaining	ratio remaining	ratio remaining
GEANT all	27152	0.65	0.57	0.53
GEANT real	15638	0.98	0.94	0.9
GEANT crosstalk	11514	0.20	0.06	0.02
Wang all	37171	0.66	0.58	0.53
Wang real	21847	0.98	0.94	0.89
Wang crosstalk	15324	0.20	0.07	0.02

5.2.3 Resolution of Relative Momenta

In constructing a correlation function it is important to understand the resolution of the detector for measuring the relative momentum, q. This is difficult to calculate analytically, but the simulation provides a simple way to compare the real relative momentum with the measured one. In the simulation two values of the relative momentum were chosen to show the resolution at low relative momentum, q = 4 MeV/c and 8 MeV/c. For these values, the first neutron's momentum, $\vec{p}_1$, was chosen by sampling the experimental energy spectra and choosing a direction from an isotropic distribution. Then the momentum of the second neutron, $\vec{p}_2$, was constructed from $\vec{q}$ - $\vec{p}_1$, where the direction of $\vec{q}$ was chosen randomly. The resulting plot of measured q shows a resolution of less than 2 MeV/c FWHM for q < 10 MeV/c (Figure 5.10).

5.2.4 Correlation Function

In order to investigate the effect of the crosstalk and its elimination on the correlation function, the simulated detector response was combined with a theoretical source to produce correlation functions. The correlation function was calculated from the one-particle phase-space distribution using the Koonin-Pratt formalism (Appendix) [Koon 77, Prat 87]. The one-particle phase-space distribution was determined from a momentum distribution of the neutrons, their emission points and the time of emission.

The simulated correlation functions were produced by a two-step process. In the first step, the initial and measured momentum of the detected neutron events were

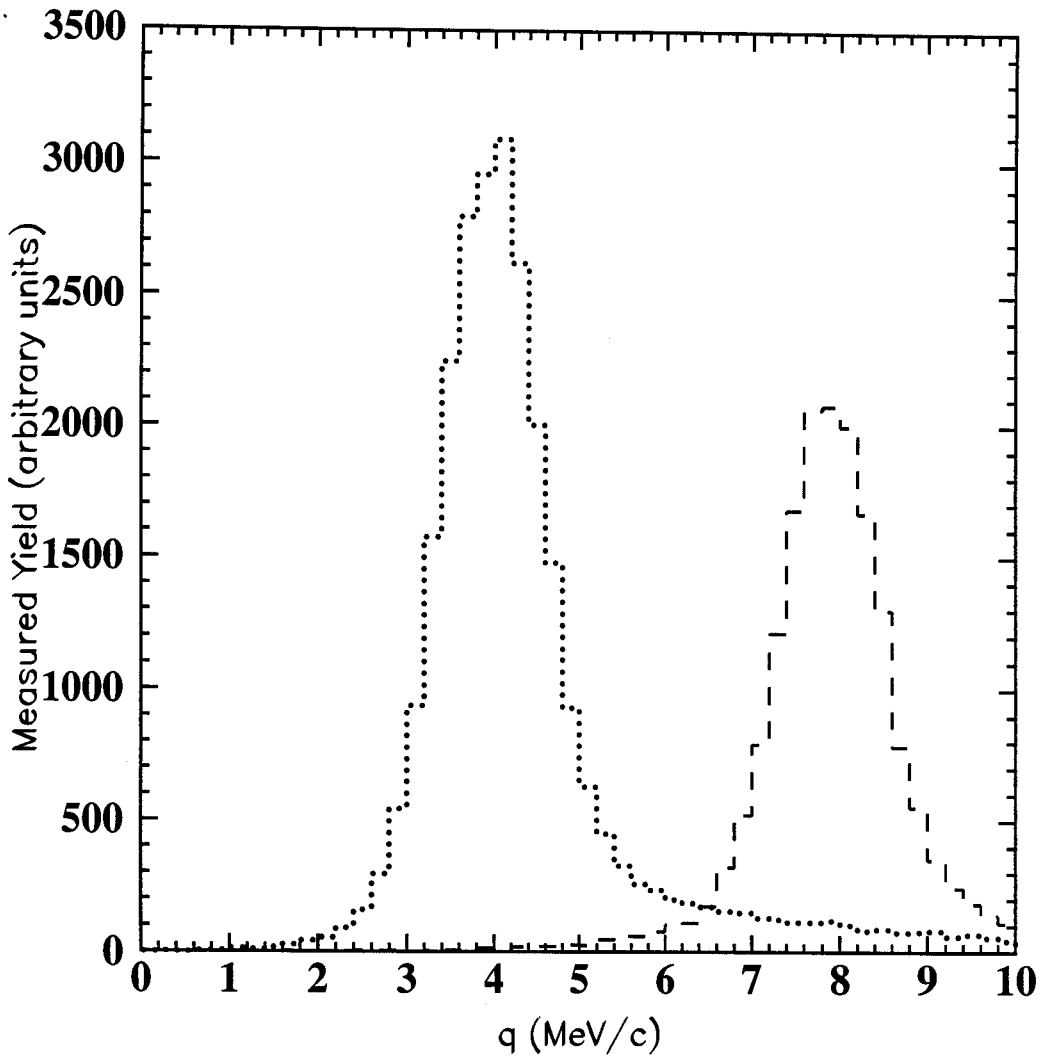

Figure 5.10 Width of measured relative momentum for a given real momentum, either 4 or 8 MeV/c, from the GEANT simulation.

recorded. In the second step, these events were combined with source points and a correlation function constructed.

The first step involves running these simulations for many events with one or two initial neutrons. The numerator was constructed from events where two neutrons were incident on the detector and two neutrons were measured. These measured coincidences include both real and crosstalk events. The events used in the denominator had one neutron incident on the detector and one neutron measured. For both types of events, the original momentum, the measured time, and the measured position were recorded. The measured values determine a measured momentum. The initial neutron energy for the simulation was sampled from the efficiency-corrected energy spectrum from the experiment.

Besides the momentum, it is also necessary to know the initial position and time of the neutron to apply the Koonin-Pratt formalism. For the correlation functions shown in this chapter, the source points were chosen from a surface model where the position and time are independent of the momentum of the particles. For each recorded event, a position was chosen from the surface of a sphere with a specified radius, r. The emission time was chosen by sampling an exponential distribution with a lifetime τ. More complicated models can be used if a table or function is constructed to relate the emission time and location to the initial momentum.

Given the original momentum and source points, it is possible to apply the Koonin-Pratt formalism to construct a correlation function. For neutron pairs from the target, this formalism calculates a weight corresponding to the correlation from

interactions between the neutrons. For crosstalk neutrons, there is no interaction and the weight is set equal to one. The original momentum is used to calculate the weight for the pair, but the measured momentum determines which q-bin is incremented with this weight. The denominator is constructed by mixing singles and binning them by the measured relative momentum, q. The resulting correlation function is normalized to one for 20 MeV/c < q < 40 MeV/c.

The correlation function for front-back pairs with cuts on $|\vec{P}|$ <250 MeV/c and E_i > 5 MeV but without a crosstalk correction (Figure 5.11 open circles) is similar to the correlation function for the data (Figure 4.10). The amplitude of the crosstalk peak in the simulation is smaller than that in the data because of a different weighting of real to crosstalk events. In the simulation, only events with two neutrons incident on the detector are included in the numerator. For the data, the number of incident neutrons varies and many events have one incident neutron. The number of crosstalk events in the data is increased by crosstalk from these one neutron events.

The simulated correlation functions, after corrections, should reproduce theoretical correlation functions without detector effects. These theoretical correlation functions are also constructed using the Koonin-Pratt formalism. The correlations are produced using the same source size and lifetime. The neutron energy is sampled from the same experimental energy spectra and used directly in the correlation function, i.e. no crosstalk, detector efficiency, or resolution effects. The theory calculates the numerator and denominator at the same time. The numerator includes a weight to account for final-state interactions, while the denominator weights all pairs equally.

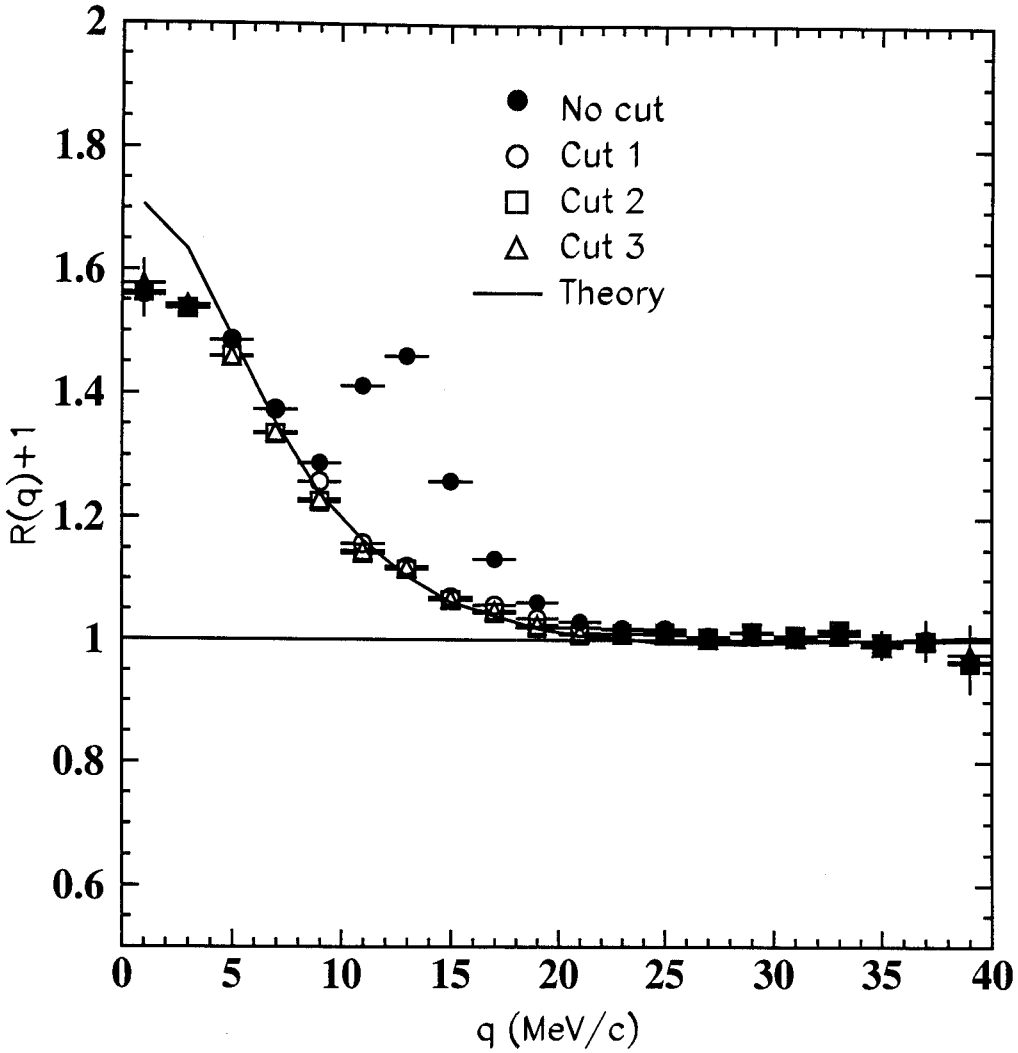

Figure 5.11 The total correlation function from the GEANT simulation. The line shows the theoretical correlation function for a source with r = 7 fm and τ = 700 fm/c and the points show the results of the simulation after various crosstalk cuts. $|\vec{P}| < 250$ MeV/c.

The simulated correlation functions after crosstalk cuts are similar to the theoretical correlations with no detector effects. The results of the correlation functions after crosstalk cuts are also shown in Figure 5.11. All three crosstalk cuts give similar results for the correlation function, showing that the correlation function is stable with respect to this cut. The differences between the theory and simulation for the lowest relative momentum bins are due to the finite resolution in the detector.

For the data, directional cuts were made on the correlation functions, and these cuts can also be made for the simulated correlation function. As in the data, the angle $\Psi = \cos^{-1}(\vec{P} \cdot \vec{q} \,/\, Pq)$ is calculated in the source rest frame (Section 4.1). Longitudinal events are defined as $\Psi < 60°$, while transverse events have $\Psi > 80°$. The effects of crosstalk, obvious in comparison to the theory, appear primarily in the longitudinal direction (Figure 5.12). These directional correlation functions must be constructed carefully since a cut that does not remove enough crosstalk can artificially show a separation between longitudinal and transverse correlation functions. With the crosstalk corrections Cut 2 or Cut 3, the correlation function reproduces the theory (Figure 5.13). In the case of Cut 1, the simulated longitudinal correlation functions is higher than the same correlation function for the other two cuts, i.e. some crosstalk remains. The directional cuts are more sensitive to crosstalk than the total correlation function, but with enough crosstalk removed, they seem to reproduce the strength of the correlation expected from the theory.

The simulation also shows that the correlation function is not as stable for the high-momentum neutron pairs. In Figure 5.14 the total correlation function is plotted for

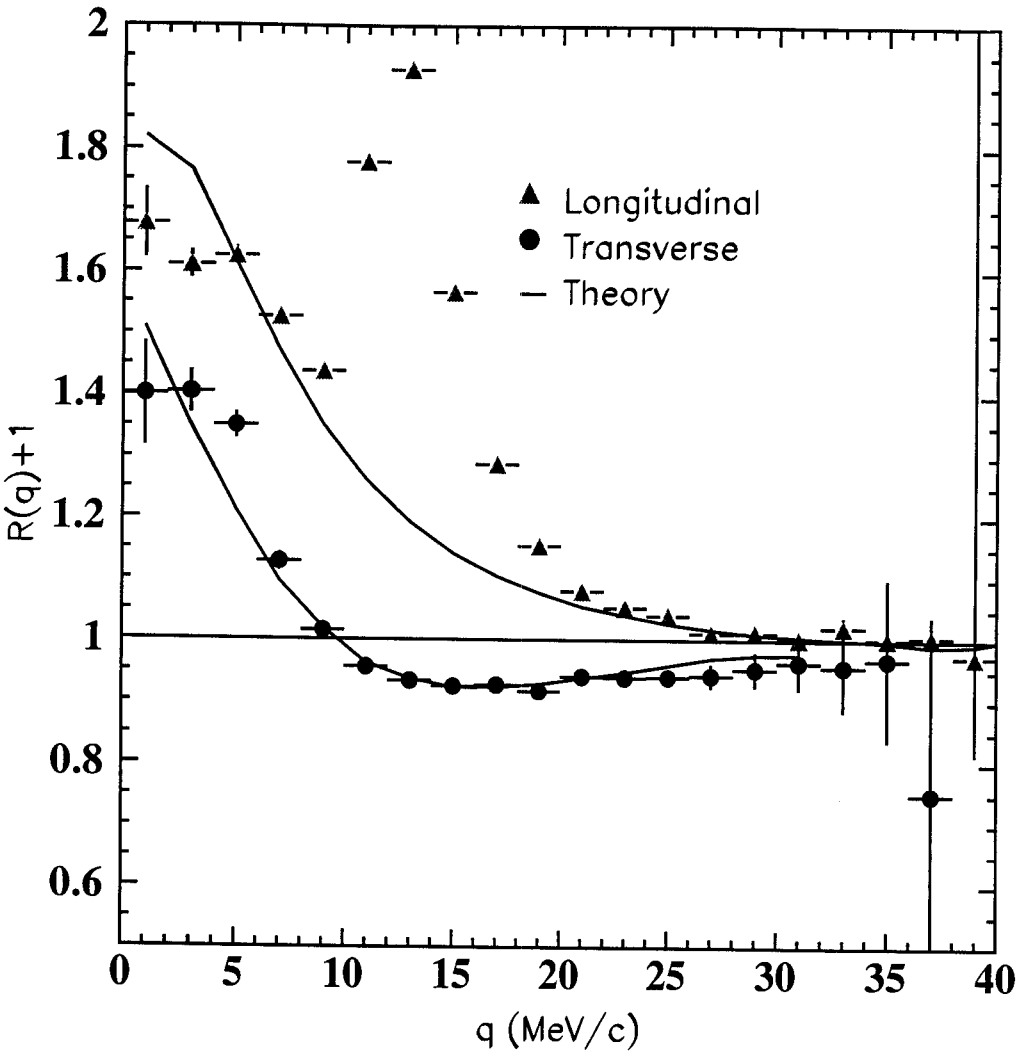

Figure 5.12 The longitudinal and transverse correlation functions from the GEANT simulation without crosstalk corrections. Longitudinal is selected by $\psi <$ 60° and transverse is selected by $\psi > 80°$. $|\tilde{P}| < 250$ MeV/c.

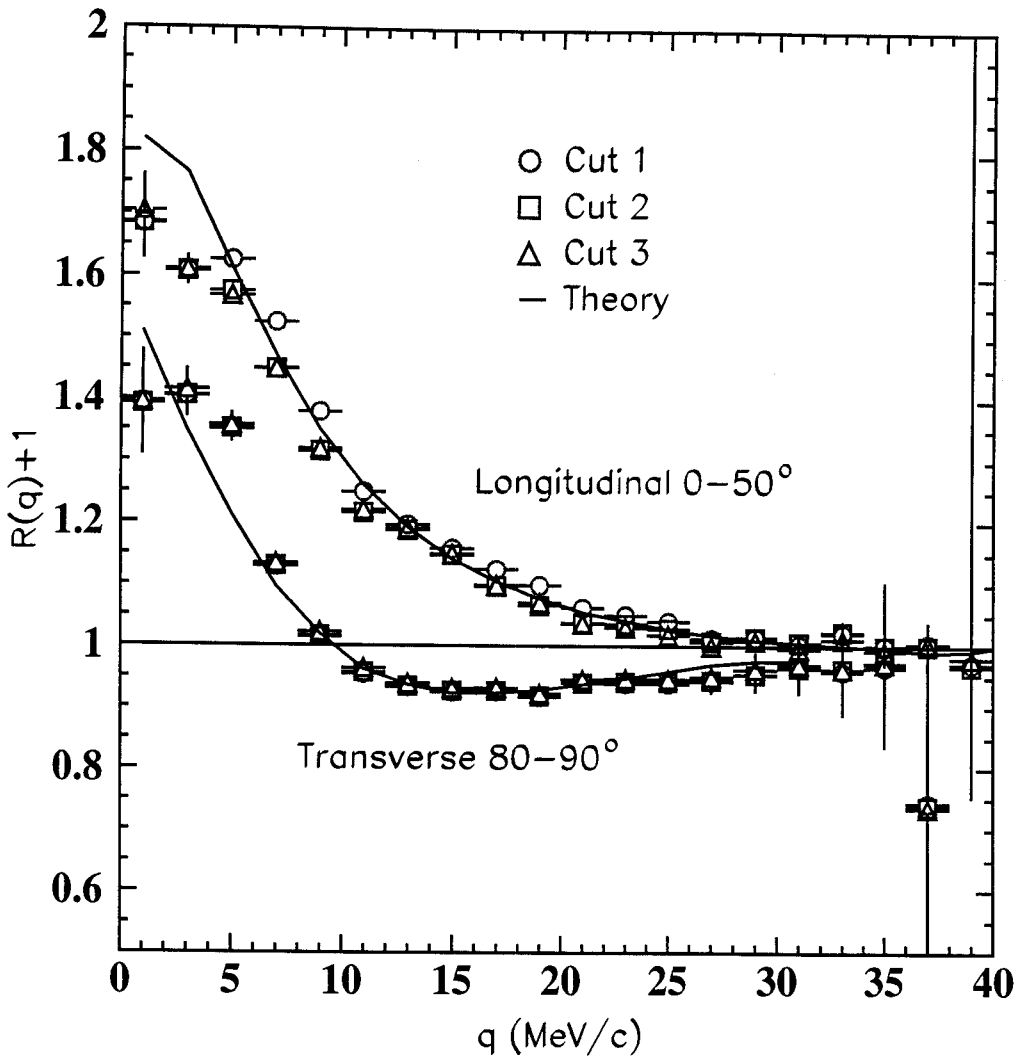

Figure 5.13 Longitudinal and transverse correlation functions from the GEANT simulation. The lines show the theory. The points represent the simulation after crosstalk cuts. $|\vec{P}| < 250$ MeV/c.

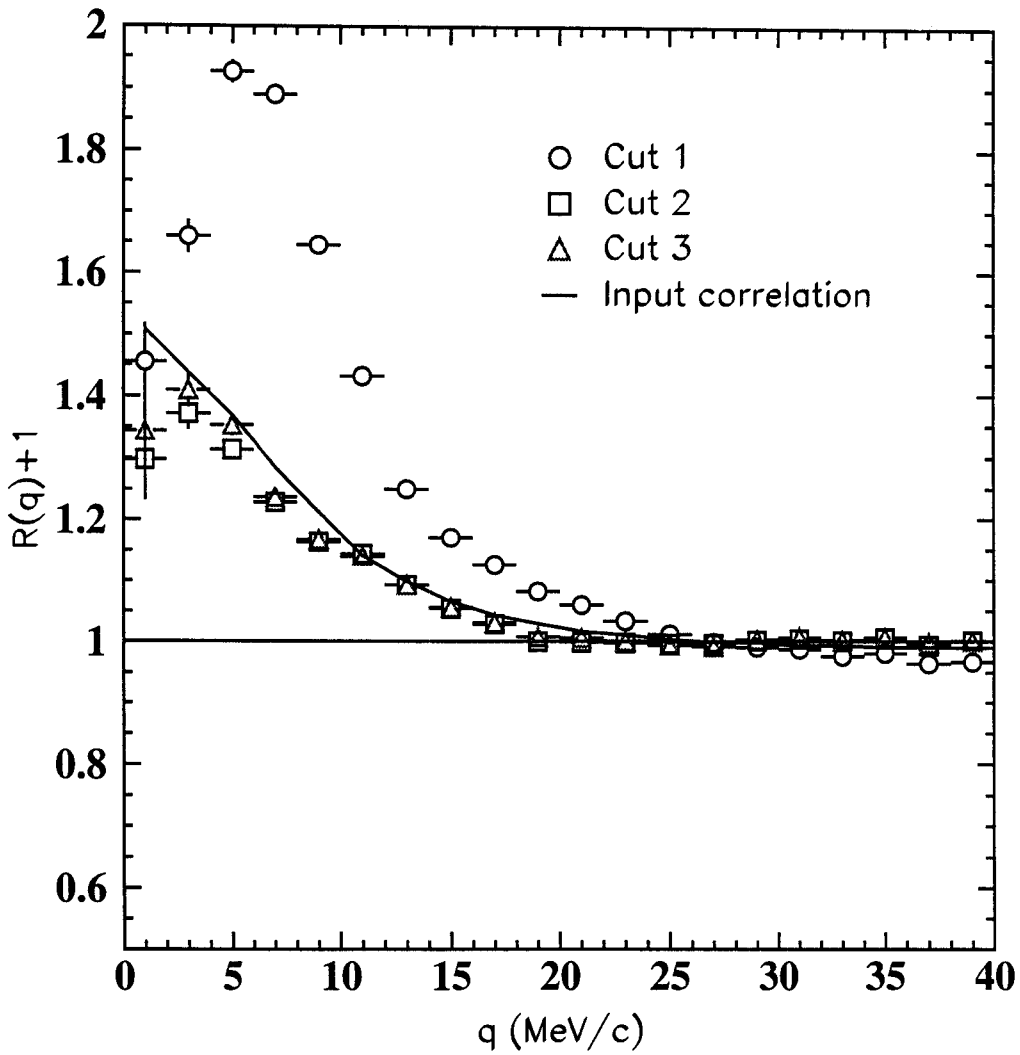

Figure 5.14 Total correlation function for high momentum pairs. $|\vec{P}| > 250$ MeV/c. The cuts are described in Table 5.4.

$|\vec{P}|$ >250 MeV/c. Cut 1 is no longer enough to remove crosstalk, and the correlation functions for the other cuts show more variation. The longitudinal and transverse cuts show a similar effect in Figure 5.15. Here the simulation does not match the theory as well as it did in the low total momentum case.

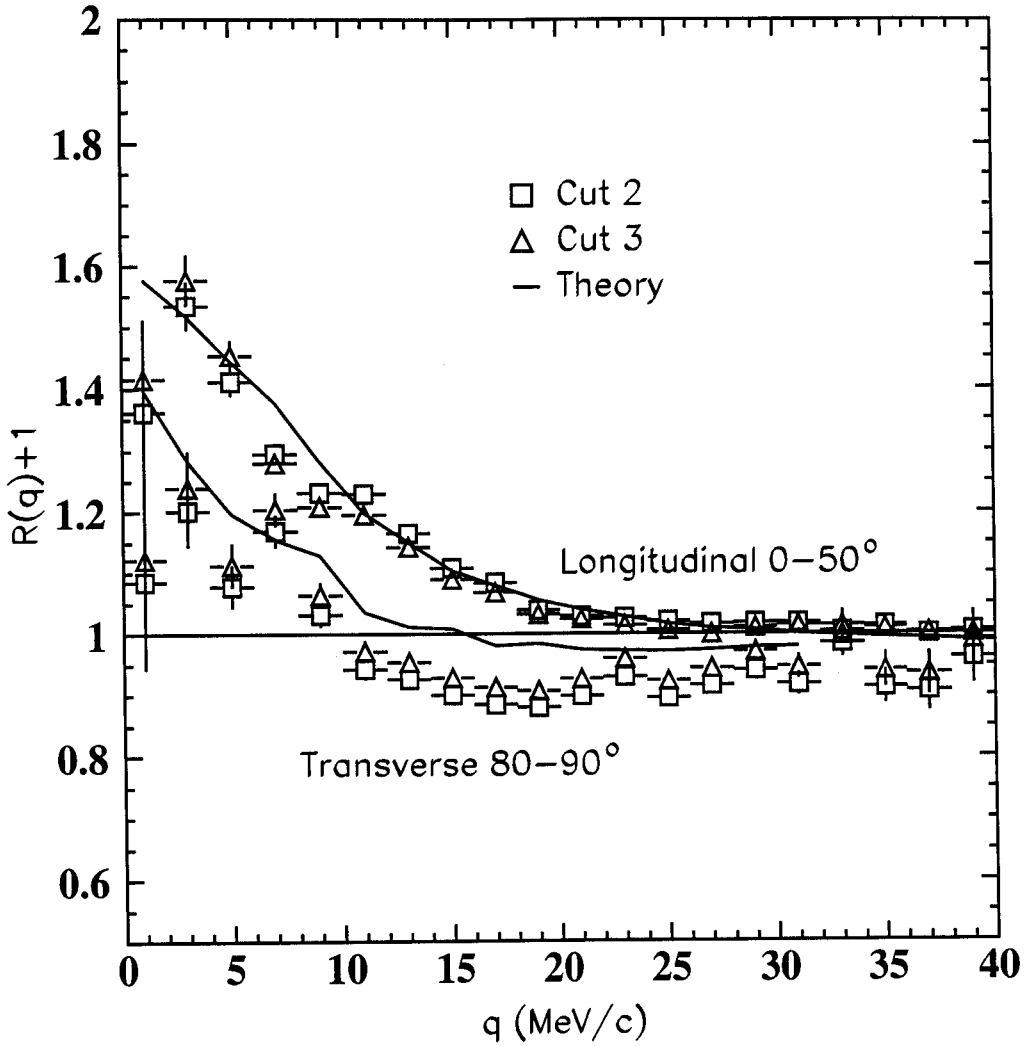

Figure 5.15 Longitudinal and transverse cuts for the high-momentum pairs.

$|\vec{P}| > 250$ MeV/c. The cuts are described in Table 5.4.

Chapter 6 - Two-Neutron Intensity Interferometry: Interpretation

Chapter 4 shows how the correlation function for the system $^{40}Ar + ^{165}Ho$ at E/A = 25 MeV was constructed and corrected for background effects. In order to interpret the experimental correlation function in terms of a source size and lifetime, it must be compared to a model. In this chapter, several models are used in order to understand how the neutron emission time from the correlation function compares to the predictions of an evaporative model.

6.1 Surface Emission Model

One simple model to compare to the correlation function is a source emitting particles with an exponential lifetime. Specifically, surface emission was used. Particles are emitted from the surface of a sphere of radius, r, with times chosen according to an exponential distribution $\exp(-t/\tau)$ described by a lifetime τ. The energy for each neutron is chosen by sampling the efficiency-corrected singles spectrum from the experiment. The energy selected for a neutron is assumed to be completely independent of its emission time.

The single-particle phase-space distribution produced by this model was filtered, made into a correlation function by the Koonin-Pratt formalism (Appendix) [Koon 77, Prat 87], and compared to data. These calculations were filtered using the simulations described in the previous chapter. A radius of 7 fm was chosen to correspond to total

fusion of the reacting nuclei ($r = 1.2\ A^{1/3}$, A = 205). The correlation functions predicted for various lifetimes were compared to the data (Figure 6.1). The best fit for this radius was a lifetime of 700 ± 200 fm/c. Since the angle-integrated correlation function does not distinguish size from lifetime, a variety of lifetimes and radii can produce a good fit (Figure 6.2). The points represent the best fit for that radius, while the error bars indicate the range of reasonable fits.

The directional cuts on the correlation functions were expected to distinguish the space and time dimensions. For a lifetime of 700 fm/c, a separation between longitudinal and transverse correlation functions is predicted by the simulations, but the data do not show a clear separation for the directional cuts (Figure 6.3). The explanation of the inconsistency between the data and the model may be that the model is too simplistic in describing the source.

6.2 Evaporative Model

In order to investigate the emission time expected, a more physical evaporative model was used. This model should provide a description of neutron emission from the compound nucleus formed in the reaction $^{40}Ar + {}^{165}Ho$ with E/A = 25 MeV. Specifically, a code which implements the statistical formalism for particle emission from Reference [Frie 83] was used. This model predicts the position, time, and energy for particles emitted from an excited source, specified by the initial number of protons and neutrons, the excitation energy, and the energy-level density.

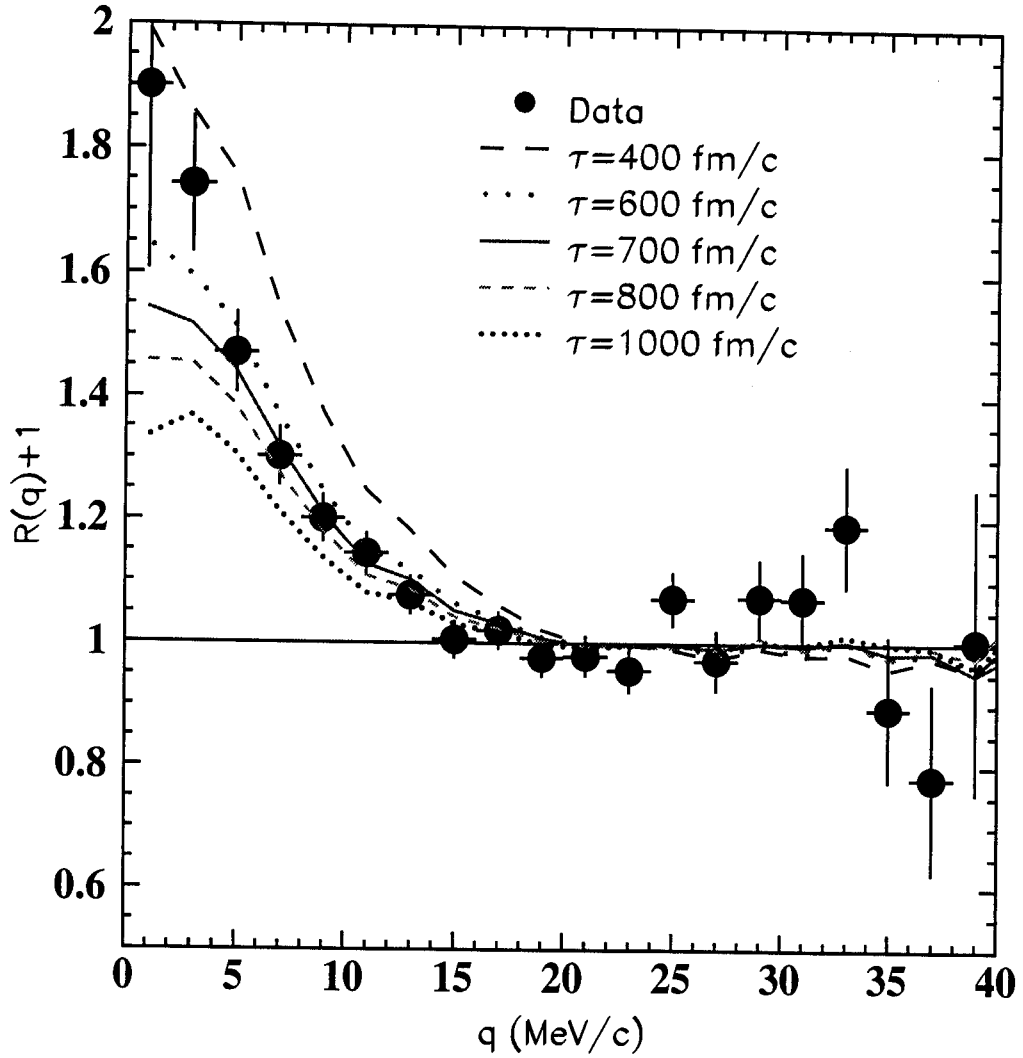

Figure 6.1 Fit of the total, filtered correlation function from a surface model, r = 7 fm, with different lifetimes.

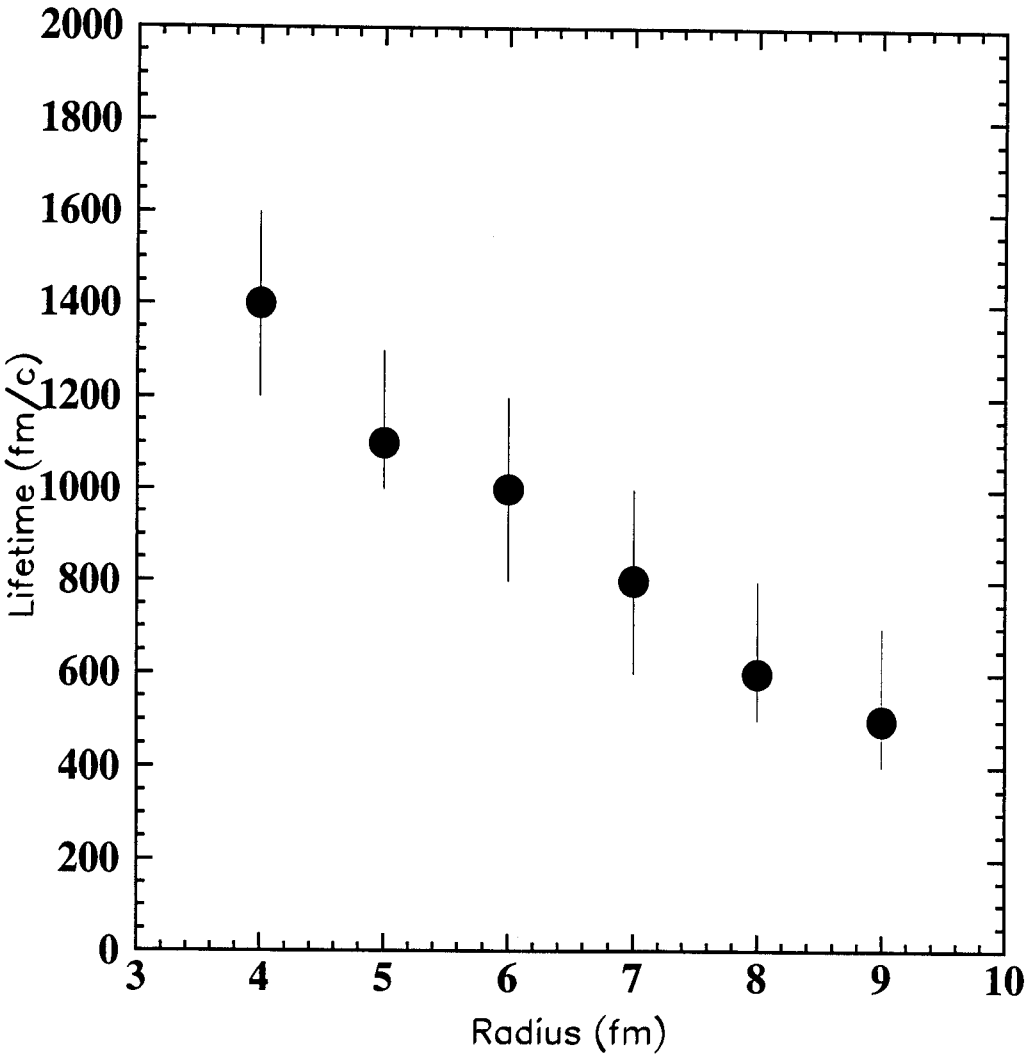

Figure 6.2 Best lifetime from the surface model for a given radius.

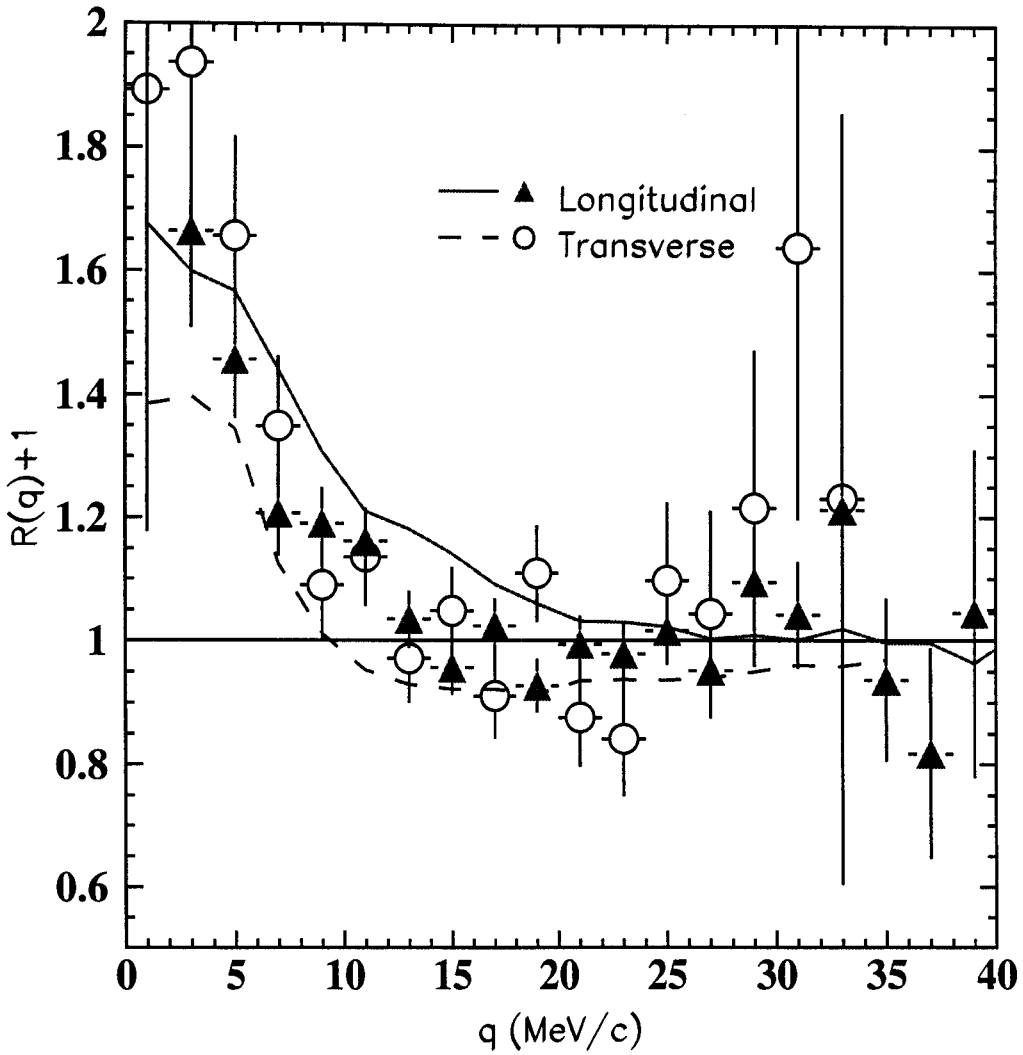

Figure 6.3 Correlation functions with longitudinal (Ψ = 0 - 60°) and transverse cuts (Ψ = 80 - 90°). The data (points) are compared to filtered calculations for surface emission from a sphere with a radius of 7 fm and a lifetime of 700 fm/c (lines).

The parameters for the statistical model were chosen as follows: First, the mass and charge of the compound nucleus were chosen to be the size of the total system, i.e., the effects of preequilibrium emission were assumed to have a small effect on the number of nucleons available to the compound source. Second, initial excitation energy and level-density parameter were determined. Since increasing the level density or decreasing the excitation energy changes the shape of the energy spectrum and correlation function in a similar way (Figure 6.4), the level-density parameter was fixed at a = A/10 and the excitation energy was adjusted.

The excitation energy is the amount of energy the compound system has initially. It determines the slope of the energy spectrum. The excitation energy calculated assuming total fusion was E*/A = 3.93 MeV. When the predicted energy spectrum was compared to the energy spectrum in the laboratory frame (Figure 6.5), the predicted energy spectrum was too shallow. (The model results were shifted into the laboratory frame by using the center-of-mass velocity of 0.045 c.) To fit the lower-energy part of the measured energy spectrum, the excitation energy was reduced to E*/A = 2.0 MeV.

Several factors might lower the excitation energy but do not completely account for the factor-of-two reduction. First, perhaps the energy-level density was not chosen properly. A larger level density would produce a steeper energy spectrum, but for this heavy system a = A/10 is already quite large. Another explanation might be incomplete fusion. For reactions at this energy, previous studies suggest that about 80% of the energy should be transferred to the compound nucleus with the remaining energy carried away by

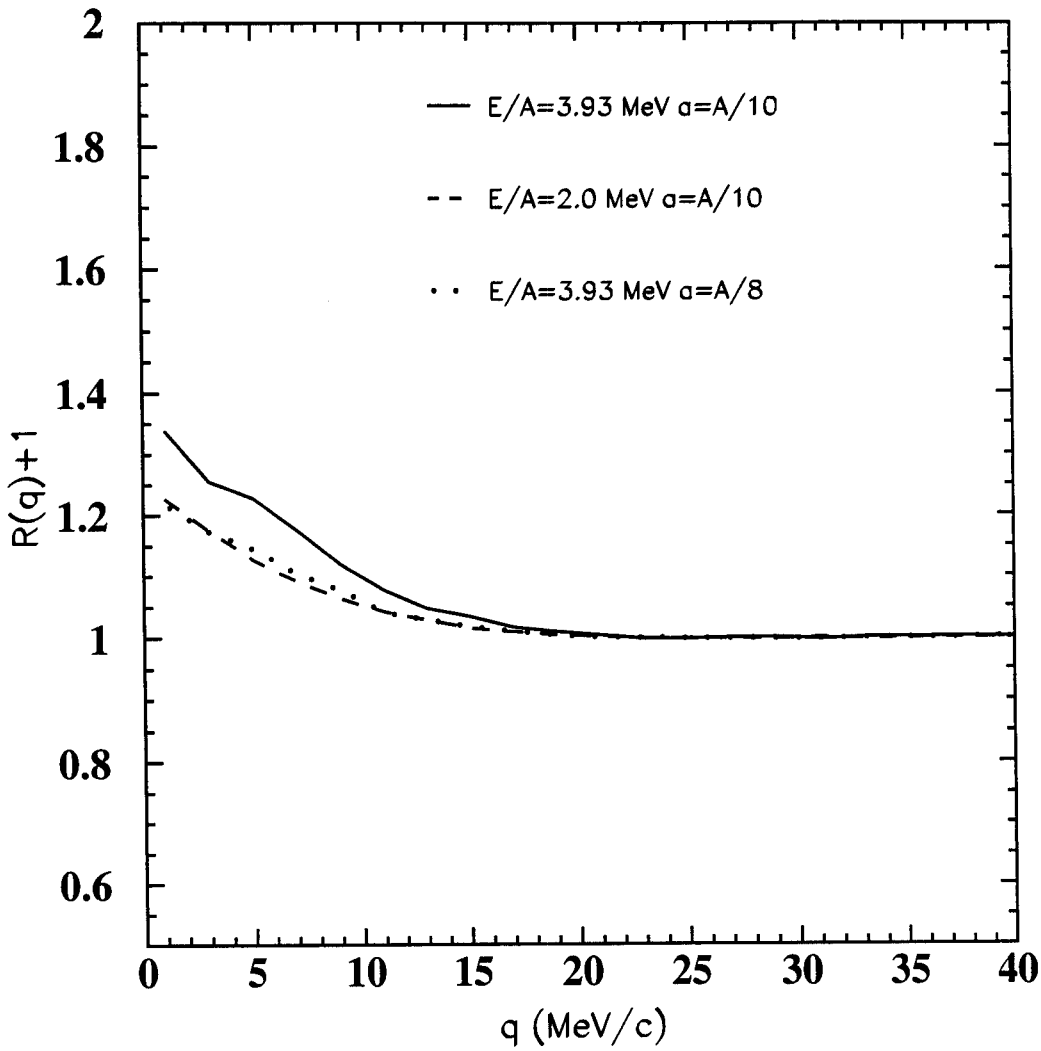

Figure 6.4 Evaporation-model calculations. The solid line is a calculation with the excitation energy of E*/A = 3.93 and a = A/10. For the dashed line the excitation energy is reduced to E*/A = 2.0. The dotted curve has the level density parameter increased to a = A/8 with the original excitation energy.

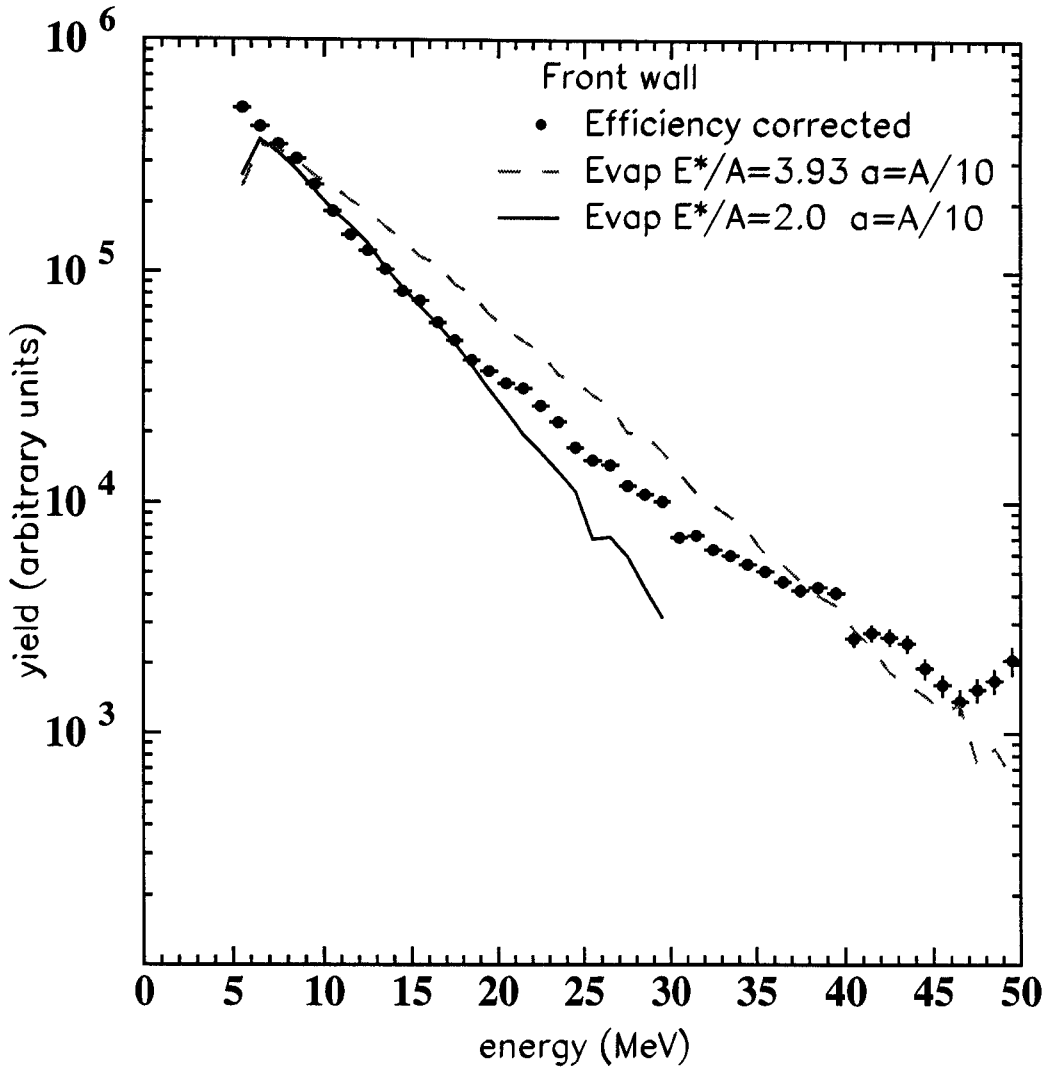

Figure 6.5 The measured energy spectrum compared to predicted energy spectra for two different excitation energies in the evaporation model [Frie 83]. The energy is plotted in the laboratory frame.

light preequilibrium particles [Viol 82, Nato 86]. Incomplete fusion could reduce the excitation energy by 20%.

This model, like the surface model, can be used to predict the correlation function. Here the results from the unfiltered theory are shown. (The simulation and theory results were already shown to be very similar in Section 5.2.4.) Figure 6.6 shows the comparison of this model with the data. For the excitation energy that fits the data, the calculated correlation function is much smaller than the measured one indicating that the model predicts too low an emission rate; in other words too large a lifetime of the source. The discrepancy between predicted and observed correlation functions cannot be attributed to the uncertainties in the initial excitation energy of the emitting source. Even for the extreme assumption of complete fusion with no preequilibrium emission the predicted lifetime is too long.

The correlation functions calculated from the evaporation model can be compared to the correlation functions produced by the surface model described in the last section. The lifetime parameters for the surface model that would make a correlation function of similar strength quantify the lifetime predicted by the evaporation model. For the lower excitation energy, which fits the energy spectrum, the lifetime determined by this comparison is 2000 fm/c for a radius of 7 fm. The correlation function at the higher excitation energy is comparable to a lifetime of 1200 fm/c. The strength of the correlation functions are compared between these two models because the dissimilarity of the shapes of the time spectra makes direct comparison difficult (Figure 6.7).

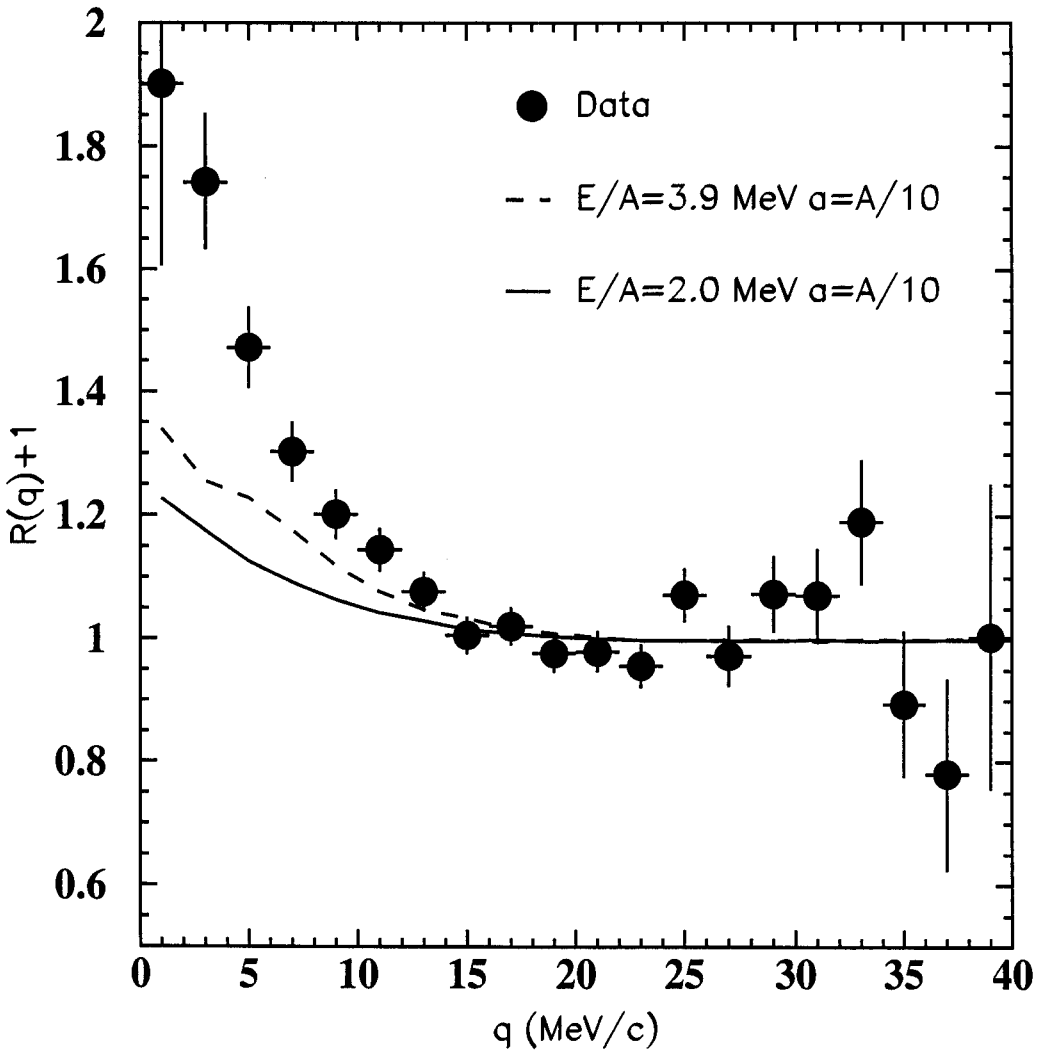

Figure 6.6 The measured correlation function compared to the evaporation-model predictions with two different excitation energies.

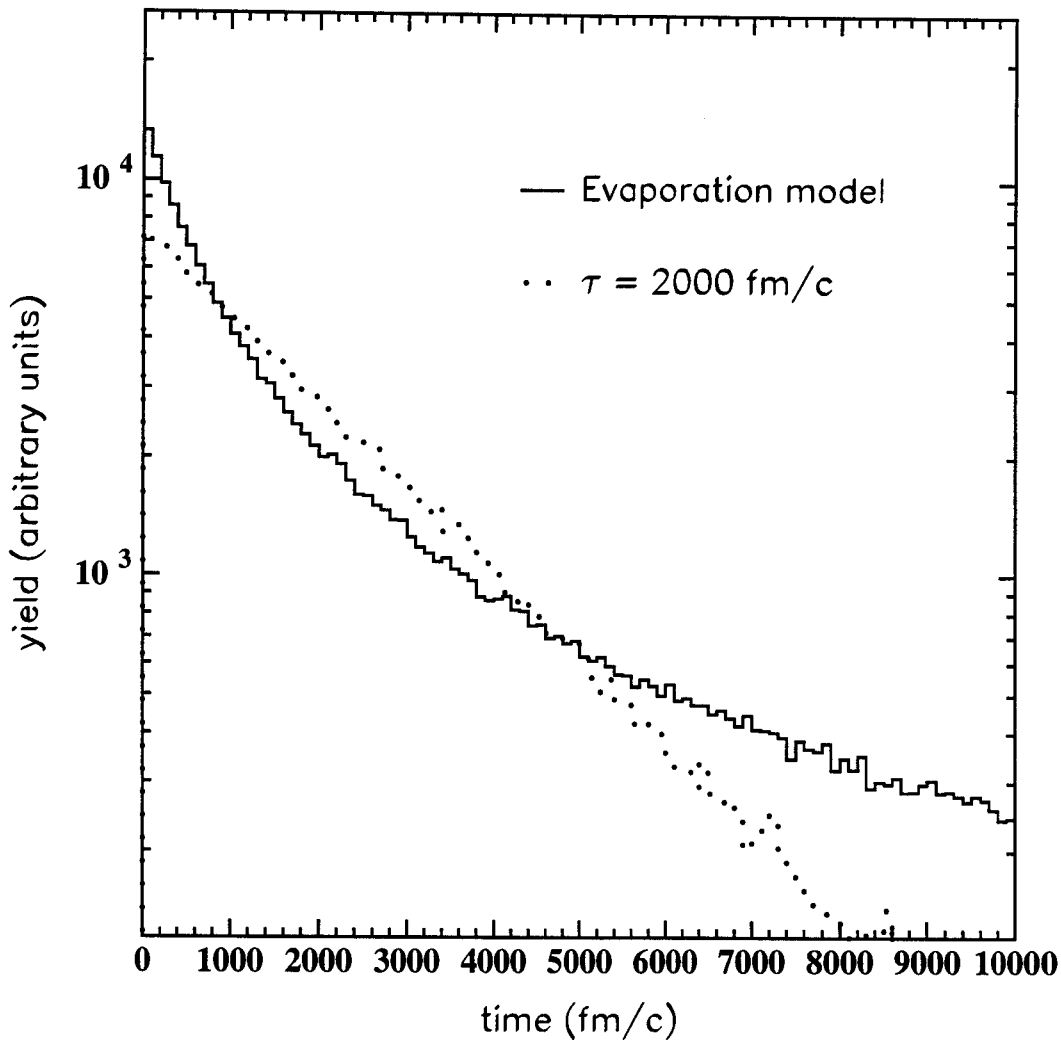

Figure 6.7 Time spectra from the evaporation model compared to the time spectrum for an exponential distribution with τ = 2000 fm/c.

The evaporative model is predicting longer lifetimes than are observed experimentally. One possible explanation is that the neutrons are not all coming from a compound source. Even though the neutrons were detected at 90°, it is possible that some of the neutrons are coming from preequilibrium emission, thus the measured time is a combination of a fast neutron component and the evaporation lifetime. This possibility is investigated in the next two sections.

6.3 Evaporation Model Plus Preequilibrium

In order to explore the effects of preequilibrium, a fast component was added to the evaporation model. The resulting hybrid model is made up of two independent sources of neutrons, each with its own temperature (energy-spectrum slope parameter) and lifetime. The experimental energy spectrum is fitted by two exponential distributions with temperatures T_p and T_c. The distribution with the lower temperature, T_c, corresponds to a compound source, while the distribution with the higher temperature, T_p, corresponds to preequilibrium emission. The ratio of neutrons of each type is energy dependent. In order to quantify the fraction of preequilibrium/total neutrons, f_p, the energy spectra are compared for energies 5 - 20 MeV.

$$f_p = \frac{\int_{5MeV}^{20MeV} N e^{-E/T_p} dE}{\int_{5MeV}^{20MeV} \left(e^{-E/T_c} + N e^{-E/T_p} \right) dE}.$$

The program to make correlation functions was modified in order to sample neutrons from these two distributions with the appropriate weights. The excitation energy

for the evaporation model was chosen to reproduce T_c. Its emission time and position are determined by the evaporation model. The energy for the preequilibrium particles is sampled from an exponential distribution with temperature, T_p. The emission points are sampled from the surface of a sphere with r = 7 fm, and the emission time was chosen, for simplicity, as $\tau_p = 0$.

Allowing for some systematic uncertainties, the decomposition of the energy spectrum into two components is not unique. By adjusting T_c and T_p, a range of weighting factors can be chosen (Figure 6.8). A fit with $f_p = 9\%$ has a similar χ^2 value to a fit with $f_p = 45\%$. Correlation functions were constructed for various weights with the appropriate temperatures (Figure 6.9). Assuming that the evaporation model is accurately determining the emission time of the compound source, the resulting correlation functions imply that about 25% of the neutrons may come from preequilibrium emission.

Using $\tau_p = 0$ provides a lower limit for the amount of preequilibrium necessary to reproduce the data. Since the preequilibrium time may be longer a larger fraction of preequilibrium would be necessary to reproduce the experimental correlation function. In the extreme case of all the neutrons coming from preequilibrium, this model would be identical to the surface model in Section 6.1 and a lifetime of τ_p = 700 fm/c would reproduce the correlation function.

In order to determine a more realistic value for the fraction of preequilibrium neutrons, calculations based on the Boltzman-Uehling-Uhlenbeck (BUU) equations [Baue 87, Li 91a, Baue 92] were used to predict the temperature for preequilibrium emission. The model was run for 200 fm/c, but the slope of the energy spectrum is fairly constant

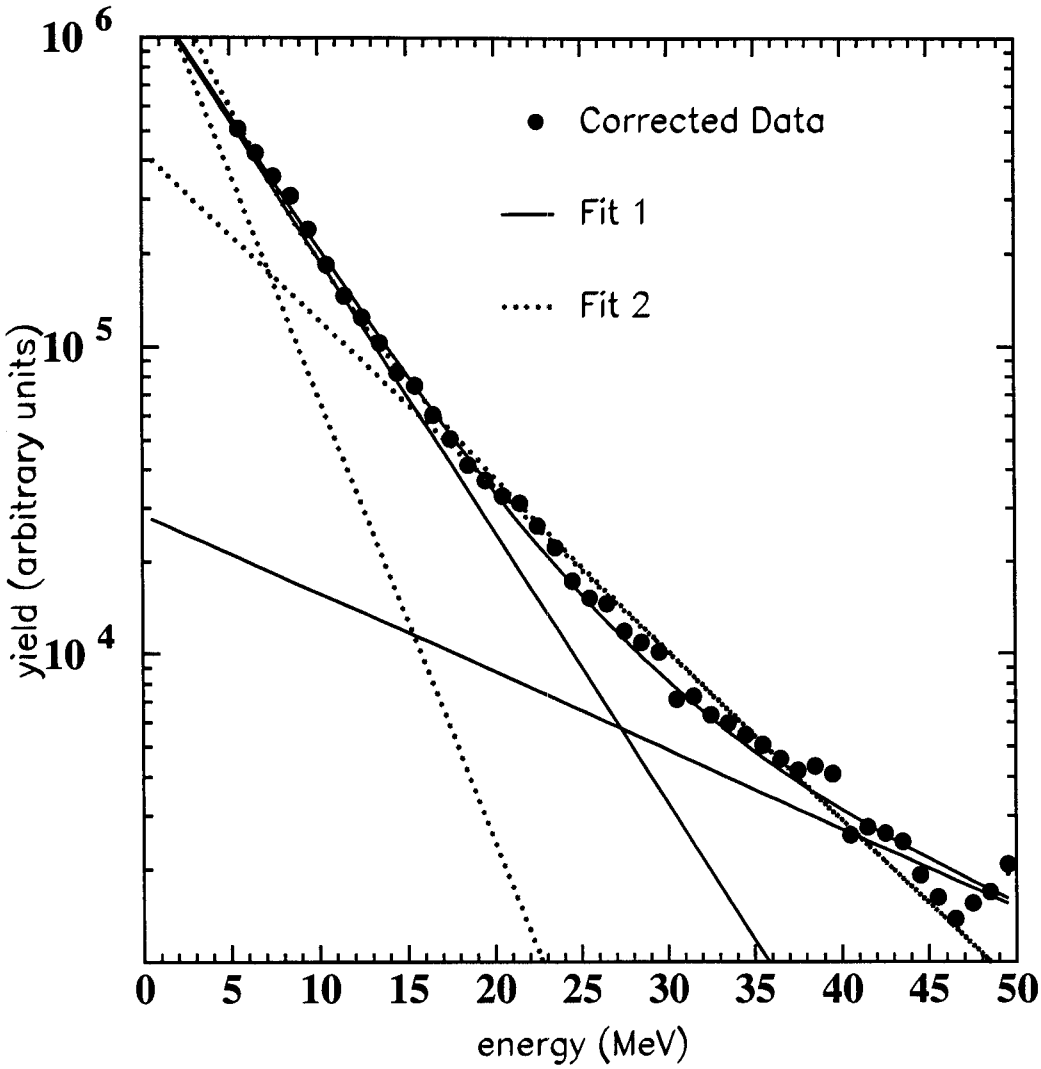

Figure 6.8 Two-component fits of the energy spectra. The lines with the steepest slopes correspond to the evaporation component; the lines with a more shallow slope correspond to the preequilibrium component; the sum for both fits lies close to the data points. Fit 1: T_c = 4.9 MeV, T_p = 17.0 MeV, and f_p = 9%. Fit 2: T_c = 3.0 MeV, T_p = 8.0 MeV, and f_p = 45%.

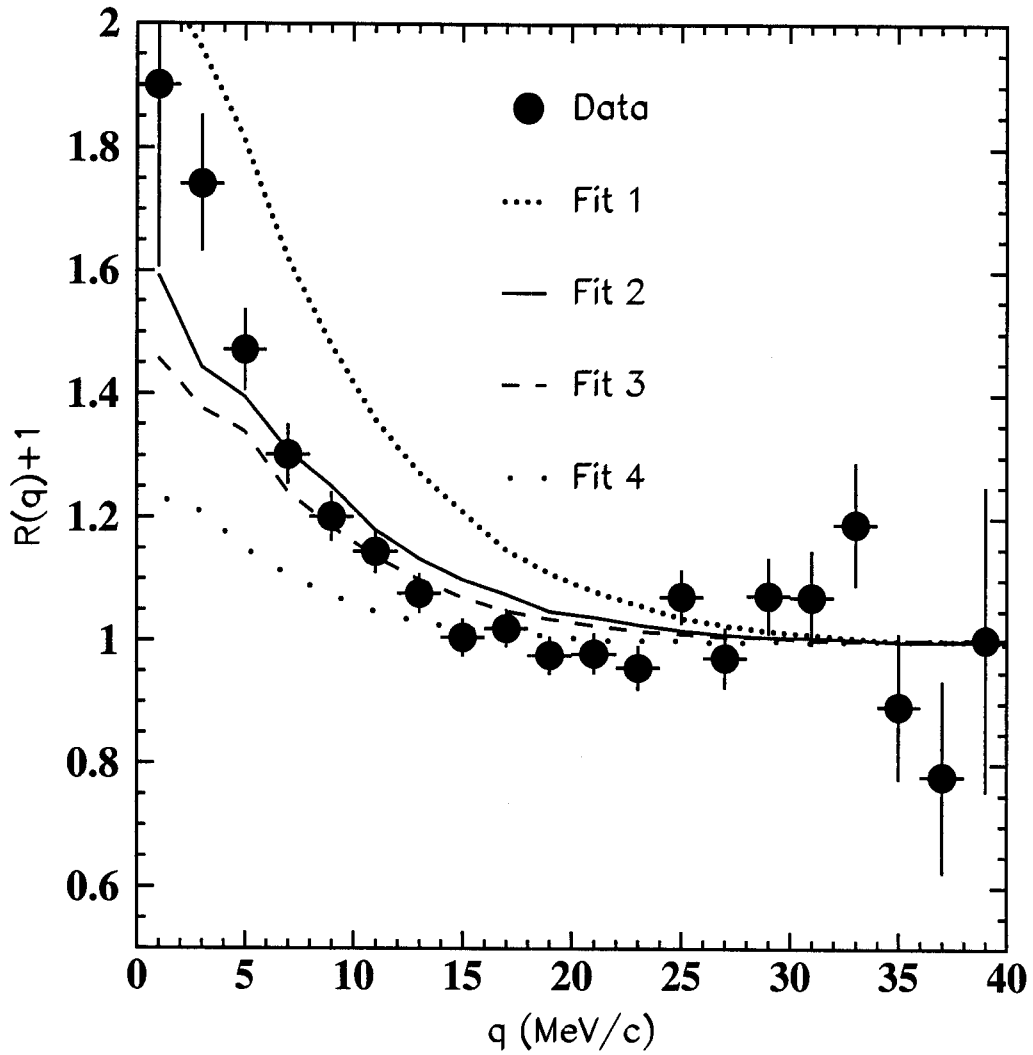

Figure 6.9 Correlation functions for various two-component fits with the evaporation-plus-preequilibrium model. Fit 1: f_p = 34%, Fit 2: f_p = 25%, Fit 3: f_p = 22%, Fit 4: f_p = 8%.

over this time, so the choice of cutoff is not important. The BUU results, with a geometrical average over impact parameters b = 1 - 5 fm, have an energy spectrum with a slope parameter corresponding to a temperature of about 12 MeV (Figure 6.10). When the temperature, T_p, is determined, T_c and f_p are determined by the slope of the energy spectrum. Using the preequilibrium temperature from the BUU calculations, the fraction of preequilibrium neutrons f_p = 18%. With τ_p = 0, the correlation function was constructed for this combination of sources (Figure 6.11). This correlation function is not as strong as that in the data, so a more realistic fraction of preequilibrium cannot bring the evaporation model into agreement with the data.

The preequilibrium neutron emission is not really instantaneous. To use a more realistic value for τ_p, the time distribution of neutrons from the BUU calculations was used as a reference. The neutron yield over time can be approximated by an exponential lifetime with τ_p = 50 fm/c (Figure 6.12). If the emission time of the preequilibrium component is chosen from this exponential distribution, the resulting correlation is somewhat reduced from the instantaneous value (Figure 6.11).

With either instantaneous emission or a lifetime τ_p = 50 fm/c for the preequilibrium component, the measured correlation function is still larger than that from the evaporation model with 18% of the neutrons from the preequilibrium component. Even with this hybrid approach the time scale in the evaporation model is too short.

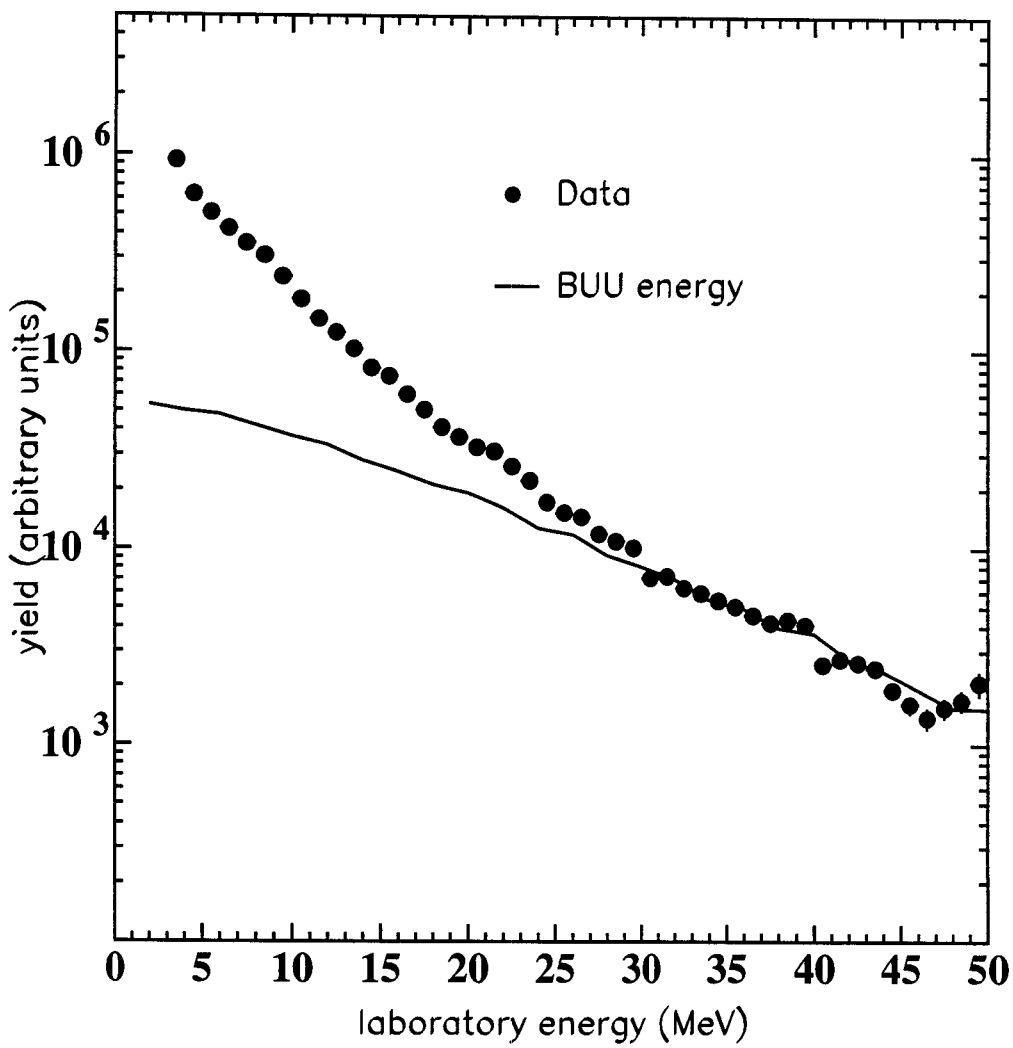

Figure 6.10 Energy spectra predicted by BUU calculations compared to the data.

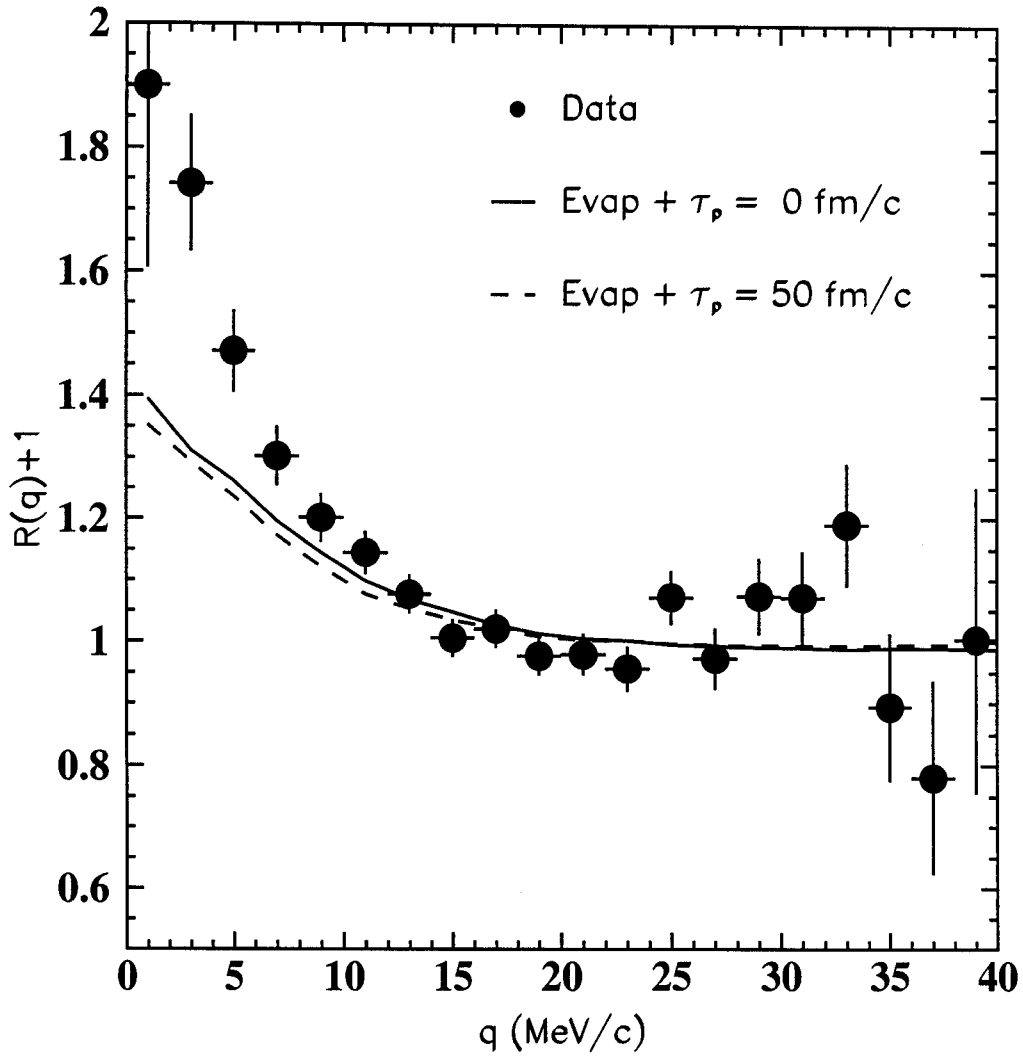

Figure 6.11 Comparing the correlation function from the data with a two-component model with preequilibrium fraction f_p = 18%. The low-energy component is from the evaporation model. The high-energy component has T_p = 12 MeV and τ_p = 0 or 50 fm/c (solid or dashed lines).

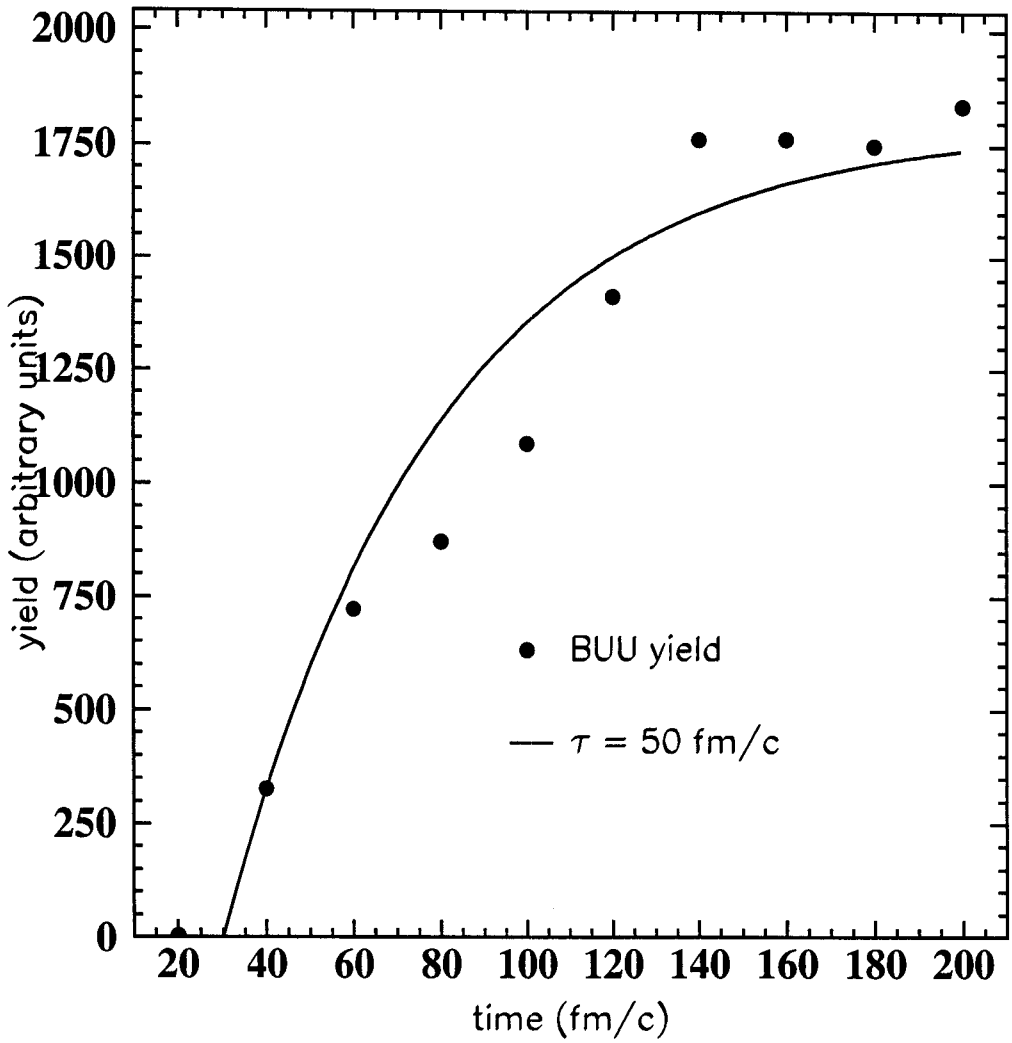

Figure 6.12 Yield of particles as a function of time from BUU calculations. The line is the yield from an exponential distribution with a lifetime of 50 fm/c.

6.4 Using Surface Emission with Two Components

In the previous section, the compound-source component of the model was fixed by a statistical evaporation model. Because the evaporation model predicts a lifetime which is too long to match the data, it is instructive to treat this lifetime τ_c as a free parameter. Again a two-component model is used, with temperatures, T_c and T_p, and weighting, f_p, selected to match the energy spectra. The two components have emission points from the surface of a sphere of radius 7 fm. The emission times for these components are sampled from two exponential distributions with lifetimes τ_p and τ_c.

By varying τ_c as a function of f_p, the best fits to the correlation function can be found (Figure 6.13). These fits were done with $\tau_p = 0$, instantaneous emission of the preequilibrium particles. The point plotted is the best fit as determined by a χ^2 test for the low-q region of the correlation functions, and the error bars include the range of reasonable fits. In this scenario it is possible to fit the correlation function for preequilibrium components up to about 30%. For larger contributions, the $\tau_p = 0$ preequilibrium component alone makes the correlation stronger than the data. At 18%, the fraction of preequilibrium that the BUU calculations predict, the best fit is with a lifetime of $\tau_c = 1000$ fm/c.

For the fraction of preequilibrium predicted by the BUU calculations, the model was also run with the preequilibrium time sampled from an exponential distribution with a lifetime, $\tau_p = 50$ fm/c (Figure 6.14). The longer lifetime for preequilibrium reduces the compound nucleus lifetime by about 100 fm/c.

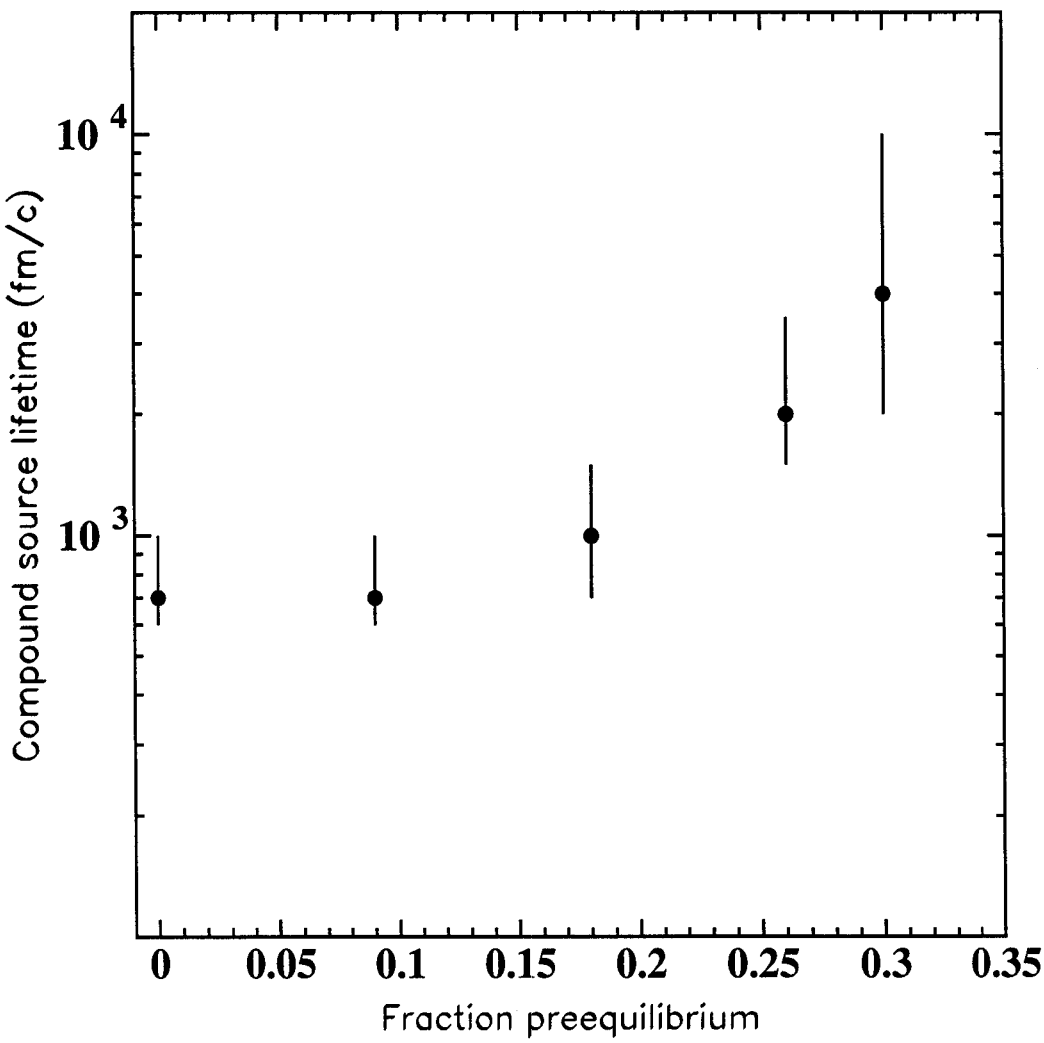

Figure 6.13 The best fit to the data for the compound-source lifetime, τ_c, for various values of f_p, assuming $\tau_p = 0$. The error bars represent the range of reasonable fits.

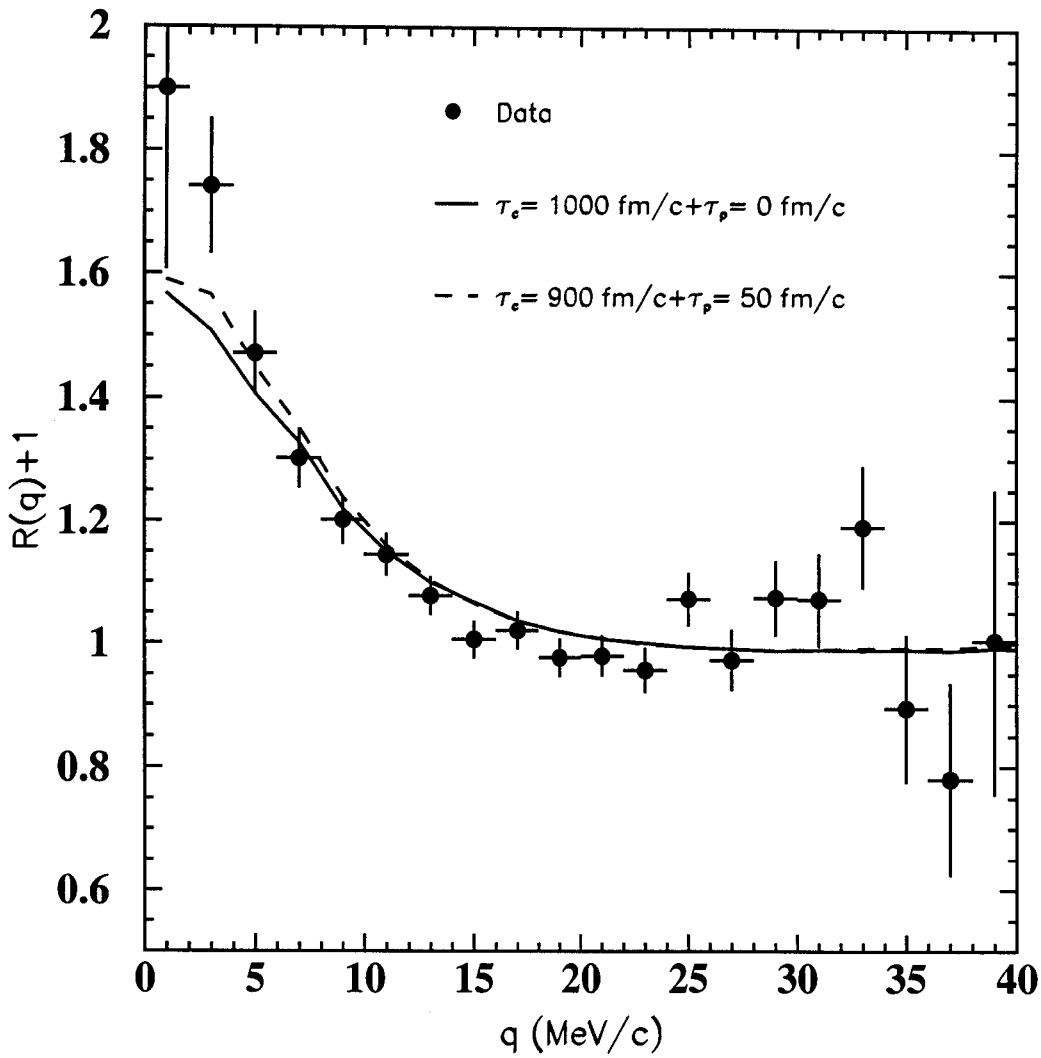

Figure 6.14 Two-component model with the time for both components sampled from exponential time distributions. The preequilibrium component has either τ_p = 0 and 50 fm/c while the compound component has τ_c = 1000 fm/c and τ_c = 900 fm/c, respectively. The preequilibrium/total fraction is f_p = 18%.

6.5 Preequilibrium and Time-Adjusted Evaporation Model

Another way to determine by how much the evaporation lifetime needs to be reduced is to adjust the emission time by scaling the time for each event, t_e. The new time, $t = s\ t_e$, is used as the compound-source component in the hybrid model described in Section 6.3. This technique retains a scaled correlation between time and energy for particle emission. Since the evaporation model predicts a different shape for the time distribution than a simple exponential distribution (Figure 6.7), this correlation must be different in the two models.

Again the two-component model is used with the low-energy component sampled from the evaporation model and $\tau_p = 0$ and $f_p = 18\%$. Using a scaling factor $s = 0.4$ brings the results into the best agreement with the data (Figure 6.15). With a longer preequilibrium time, τ_p, the scaling factor would have to be even smaller. The evaporation time seems to be a factor-of-two too long.

6.6 Summary and Outlook

Several observations result from this experiment measuring the two-neutron correlation function for $^{40}Ar + ^{165}Ho$ at E/A = 25 MeV. The data show a strong peak at q = 0 in the correlation function, but no clear separation of longitudinal and transverse correlation functions.

The measured total correlation function can be described by a source of radius 7 fm and an exponential lifetime of 700 fm/c. To compare this lifetime to the expectations for a compound nucleus, a statistical evaporative model was used. This model predicts a

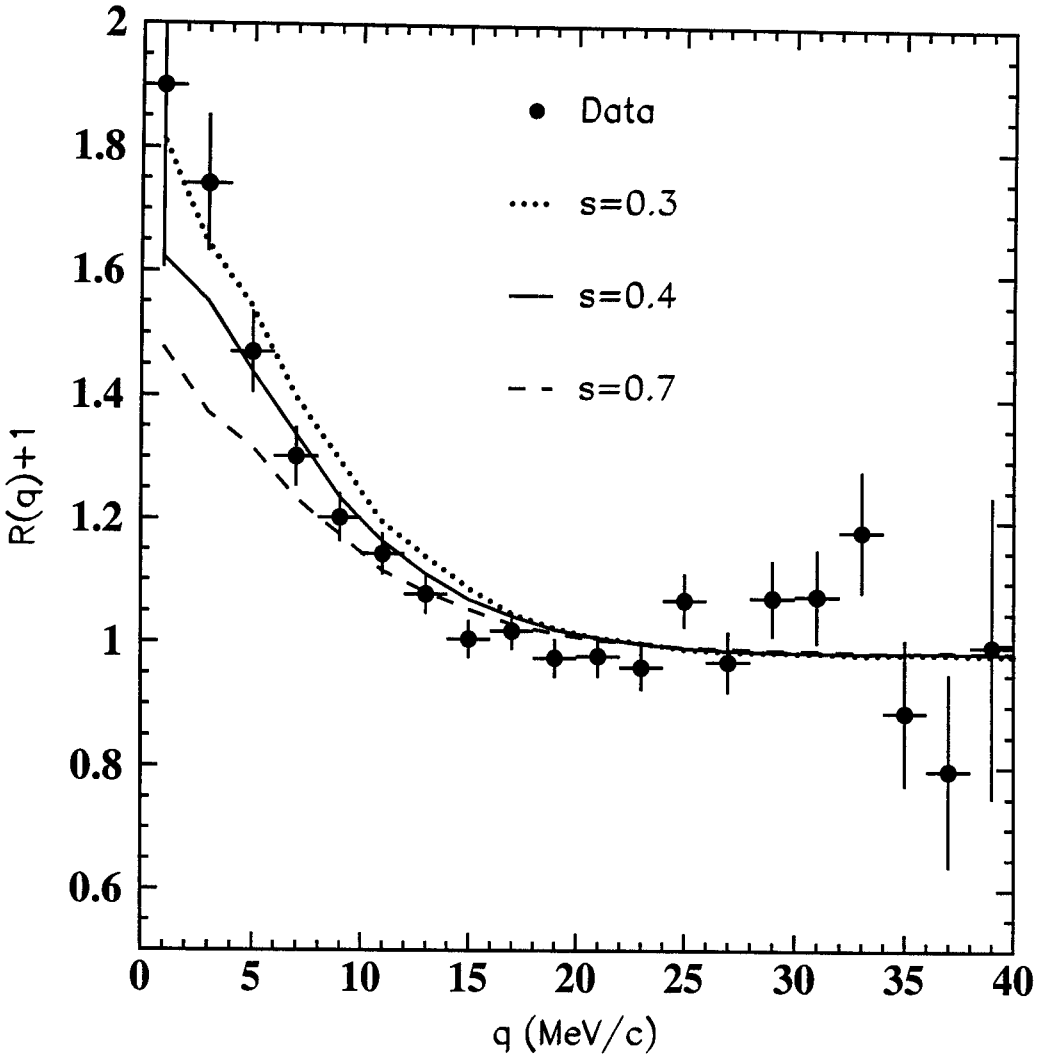

Figure 6.15 Two-component model, with the low-energy component taken from the evaporation model with each emission time scaled by a factor s. The preequilibrium component has $f_p = 18\%$ and $\tau_p = 0$.

correlation function that would be consistent with a surface-model parameterization of 2000 fm/c with a radius of 7 fm.

How preequilibrium emission changes the apparent lifetime of the correlation function was investigated by various hybrid models. Using the experimental energy spectrum as an additional constraint, it is found that the addition of 25% preequilibrium with $\tau_p = 0$ can enhance the correlation function from the evaporation model so that it fits the data. Longer lifetimes for the preequilibrium component require a larger fraction. Using the Boltzman-Uehling-Uhlenbeck model to predict the temperature of the preequilibrium component implies that 18% of the neutrons come from preequilibrium. With this ratio for instantaneous preequilibrium neutrons, the correlation function can be reproduced by a surface emission model with a lifetime of 1000 fm/c. If the emission time in the evaporation model is scaled by a factor of 0.4, it can also reproduce the experimental correlation function with 18% of the neutrons from instantaneous preequilibrium emission. All of these models suggest that the evaporation model predicts a lifetime that is too long by about a factor-of-two compared to the data

The lack of separation for longitudinal and transverse correlation functions is puzzling, as the lifetime from the total correlation function seems long enough that all the models predict a separation of longitudinal and transverse directional cuts. This lack of separation could be the result of a mixture of sources due to poor impact-parameter selection.

Future two-neutron intensity interferometery measurements could be improved in several ways. First, an experiment should be run at a lower beam energy where fewer or

no preequilibrium neutrons would be produced. Also it would be beneficial to restrict the class of events further by measuring a heavy residue in coincidence with the two neutrons. These two improvements should produce a cleaner source determination, perhaps resulting in a measurable difference between the angle-selected correlation functions. A technical improvement would be to perform the measurement in a larger room where there would be fewer background neutrons. Better statistics would also allow a more thorough analysis. To obtain better statistics, more solid-angle coverage would be necessary for either the trigger detector or the neutron detectors or both. As this experiment already ran for almost two weeks, just running longer would be a less attractive option. With these improvements two-neutron intensity interferometry could make a stronger statement about the lifetime of the compound source.

Chapter 7 - Conclusion

In this thesis, intensity interferometry was used to measure the size and lifetime of the emission zone in two intermediate-energy heavy-ion reactions. One reaction used two-proton intensity interferometry to investigate ^{16}O + ^{197}Au collisions at E/A = 200 MeV. The other reaction employed two-neutron intensity interferometry to measure ^{40}Ar + ^{165}Ho collisions at E/A = 25 MeV.

Two-proton correlation functions were measured for ^{16}O + ^{197}Au collisions at E/A = 200 MeV. When compared with BUU calculations [Baue 87, 92, Li 91a, 91b] the momentum-integrated correlation function agrees well with the data, but the dependence of the correlation function on the momentum of the particles is overpredicted by the theory. Several correlation functions measured in this energy region [Kund 93, Hand 95b] show a source that is larger or longer lived than the BUU model predicts. The BUU model takes into account the dynamics of the reaction but is missing some physics that would account for the longer emission times seen in the data. Protons from long-lived resonances are not included in this model and may account for at least part of the difference between theory and experiment [Hand 95b].

Two-neutron intensity interferometry was used to measure the reaction ^{40}Ar + ^{165}Ho at E/A = 25 MeV. Near-central collisions were selected and a correlation function constructed from coincident neutrons. The coincident neutrons were corrected for crosstalk and background scattering, and the crosstalk corrections were tested using two independent simulation codes. The neutrons used to construct the correlation function

were required to have energies greater than 5 MeV, in order to reduce background scattering. The simulations for $|\vec{P}| < 250$ MeV/c showed that the correlation function is not distorted by this crosstalk elimination method. However, the higher total-momentum pairs have a significant amount of crosstalk remaining.

For this beam energy, E/A = 25 MeV, incomplete fusion is expected with the formation of a compound nucleus. The results are compared to an evaporation model. For this reaction, the extracted lifetime is shorter than the model predicts. Emission from the surface of a 7 fm sphere with an exponential time distribution fits the data for a lifetime of 700 ± 200 fm/c. The correlation function from the evaporation model [Frie 83] is compared to the same surface model. The correlation function for the evaporation model, after accounting for preequilibrium emission as predicted by BUU, is comparable to the correlation function from this model with an exponential lifetime of 2000 ± 500 fm/c. The neutron data have larger uncertainties than the proton data and a measurement with more statistics and a stricter event selection would improve the experimental results. The data from this experiment are consistent with a lifetime about a factor-of-two shorter than the evaporation model predicts. This evaporation model is quite basic, so a more elaborate model might explain some of this difference. This evaporation model was chosen because it gives a reasonable approximation of evaporation without a large number of free parameters.

Checking the time scale in evaporative models has relevance to the interpretation of lifetimes from fission reactions. Many experiments have measured fission lifetimes as a way to understand dissipation in the nuclear medium. At least three different methods

have been used to measure the fission lifetime. One method is to measure the pre- and post-scission neutron multiplicities. The emission of each neutron requires a finite time and so the number of pre-fission neutrons is assumed to be related to the lifetime of the compound nucleus before fission [Hind 84]. For excitation energies from 45-90 MeV, fission lifetimes from 2 - $5x10^{-20}$ s = 6000-15,000 fm/c have been extracted using various models [Hind 85, Siwe 95, Andr 95]. The second method of measuring fission lifetimes is to measure the gamma multiplicity from giant dipole resonances [Paul 94]. Experiments using this technique for a source with an excitation energy of 64 MeV, predict time scales of $2.9x10^{-19}$ s (87,000 fm/c) [Buts 91]. The third method uses crystal blocking and predicts a lifetime greater than 10^{-19} s = 30,000 fm/c for excitation energies less than 250 MeV where the fusion time becomes longer with decreasing excitation energy [Morj 97].

Because the first two methods rely on statistical models to extract a lifetime from the measured quantities, using two-neutron intensity interferometery in this energy regime to confirm the time scale of these models is especially useful. The results presented in this thesis indicate that the evaporation model [Frie 83] is accurate to about a factor-of-two. Discrepancies in the fission lifetimes differ by factors of ten, which are not accounted for by uncertainties in the evaporation model.

The original question of how the heavy residue distorts the two-proton correlation function still remains. It would be interesting to compare two-proton and two-neutron intensity interferometry methods in this evaporative region. Unfortunately, no two-proton measurements are available for the $^{40}Ar + ^{165}Ho$ system.

APPENDIX

Appendix - The Koonin-Pratt Formalism

Most theories modeling nuclear reactions predict the one-particle phase-space distribution. In order to transform these into a correlation function, the Koonin-Pratt formalism is applied. This formalism has been derived elsewhere [Koon 77, Prat 84, Prat 87, Gong 91a]. Here the basic form and assumptions relevant to two-proton and two-neutron correlation functions are reviewed [Lisa 93b].

The basic formula relates the single-particle source function $g(\vec{r}, \vec{p}, t)$ to the correlation function, $1 + R(\vec{P}, \vec{q})$. The source function represents the probability that a particle of momentum $\vec{p}$ will be emitted at position $\vec{r}$, and time t. Then the correlation function can be written as a function of $\vec{P}$, the total momentum of the pair and $\vec{q}$, the invariant relative momentum:

$$1 + R(\vec{P}, \vec{q}) = \frac{P(\vec{p}_1, \vec{p}_2)}{P(\vec{p}_1)P(\vec{p}_2)}$$

$$= \frac{\int d^3\vec{r}_1 dt_1 d^3\vec{r}_2 dt_2 g(\vec{r}_1, \vec{P}/2, t_1) g(\vec{r}_2, \vec{P}/2, t_2) \left|\phi(\vec{q}, \vec{r}_1 - \vec{r}_2 - (^{(t_1 - t_2)}/_{2m}) \cdot \vec{P})\right|}{\int d^3\vec{r}_1 dt_1 g(\vec{r}_1, \vec{P}/2, t_1) \bullet \int d^3\vec{r}_2 dt_2 g(\vec{r}_2, \vec{P}/2, t_2)}.$$

In this equation $P(\vec{p}_1, \vec{p}_2)$ and $P(\vec{p})$ are the probabilities of measuring two particles and a single particle with the given momenta. The wave function $\phi(\vec{q}, \vec{r})$ depends only on the relative phase-space coordinates at the time of emission of the second particle.

Several assumptions enter into deriving this form for the theoretical correlation function. First, the particles are assumed to be emitted independently. All correlations are assumed to result from the final-state interaction and not from the actual emission process. This assumption is not completely valid since at least conservation laws link the emission of particles [Lync 82]. Other entrance-channel effects [Zhu 91] or correlations in the source [Bern 85, Alm 93, Kund 93] may also destroy the independence hypothesis.

The second assumption for this derivation is that the two particles interact only with each other not with the residue or other emitted particles. For neutrons this is especially appropriate, since no Coulomb interactions apply.

These assumptions allow the source-emission phase-space to be factored into the product of the single-particle source functions $g(\vec{r}, \vec{p}, t)$. The relative wave function, $\phi(\vec{q}, \vec{r})$, creates the correlation which destroys the factorability of the final probabilities:

$$P(\vec{p}_1, \vec{p}_2) \neq P(\vec{p}_1)P(\vec{p}_2).$$

The third assumption is that the source function does not vary greatly over a momentum region of order $|\vec{q}|$. This is appropriate for these heavy-ion collisions where the particle momenta are typically hundreds of MeV/c while the relative momenta of interest are less than 50 MeV/c.

The two-particle relative wave function, $\phi(\vec{q}, \vec{r})$, determines the theoretical correlation function. For applications of this theory in this thesis, the wave function is determined numerically by solving the Schrödinger equation for the $\ell = 0$ and $\ell = 1$ partial waves with the Coulomb and Reid soft-core potential [Reid 68]. In the case of neutrons the charge for the Coulomb potential is set to zero. The full wave function is then determined by

$$\left|\phi(\vec{q}, \vec{r})\right|^2 = \frac{1}{4}\left|\phi_s(\vec{q}, \vec{r})\right|^2 + \frac{3}{4}\left|\phi_t(\vec{q}, \vec{r})\right|^2$$

where $\phi_s(\vec{q}, \vec{r})$ and $\phi_t(\vec{q}, \vec{r})$ are the singlet and triplet two-neutron spatial wave functions, respectively. The weighting of this equation is determined by assuming a statistical distribution of spins.

BIBLIOGRAPHY

BIBLIOGRAPHY

[Alm 93] T. Alm, G. Röpke, and M. Schmidt, Phys. Lett. **B301**, 170 (1993).

[Andr 95] A.N. Andreyev, D.D. Bogdanov, V.I. Chepigin, A.P. Kabachenko, O.N. Malyshev, Yu.A. Muzichka, Yu.Ts. Oganessian, A.G. Popesko, B.I. Pustylnik, J. Rohác, R.N. Sagaidak, A.V. Taranenko, G.M. Ter-Akopian, A.V. Yeremin, Nucl. Phys. A **583**, 153 (1995).

[Awes 88] T.C. Awes, R.L. Ferguson, F.E. Obenshain, F. Plasil, G.R. Young, S. Pratt, Z.Chen, C.K. Gelbke, W.G. Lynch, J. Pochodzalla, and H.M. Xu, Phys. Rev.Lett. **61**, 2665 (1988).

[Baue 87] W.Bauer, Nucl. Phys. **A471**, 604 (1987).

[Baue 92] W. Bauer, C.K. Gelbke, and S. Pratt, Annu. Rev. Nucl. Part. Sci. **42**, 77 (1992).

[Bayu 87] Yu.D. Bayukov, P.V. Degtyarenko, Yu.V. Efremenko, V.B. Fedrorov, V.B. Gavrilov, N.A. Goryainov, Yu. G. Grinshuk, O.B. Gushchin, I.A. Klumov, G.A. Leksin, A.V. Stavinskky, V.P. Surin, S.M. Shuvalov, and B.B. Shvartsman, Phys. Let B **189**, 291 (1987).

[Bern 85] M.A. Bernstein, W.A. Friedman, W.G. Lynch, C.B. Chitwood, D.J. Fields, C.K. Gelbke, M.B. Tsang, T.C. Awes, R.L. Ferguson, F.E. Obenshain, F. Plasil, R.L. Robinson, and G.R. Young, Phys. Rev. Lett. **54**, 402 (1985).

[Bert 89] G.F. Bertsch, Nucl. Phys. A **498**, 173c (1989).

[Benr 93] F. Benrachi, B. Chambon, B. Cheynis, D. Drain, C. Pastor, H. Rossner, D. Hilscher, B. Gebauer, D. Husson, A. Giorni, D. Heuer, A. Lleres, P. Stassi, and J.B. Viano, Phys. Rev. C **48**, 2340 (1993).

[Boal 90] D.H. Boal, C.K. Gelbke, and B.K. Jennings, Rev. Mod. Phys. **62**, 553 (1990).

[Butl 70] G.W. Butler, A.M. Poskanzer, and D.A. Landis, NIM **89**, 189 (1970).

[Buts 91] R. Butsch, D.J. Hofman, C.P. Montoya, P.Paul, and M. Thoennessen, Phys. Rev. C **44**, 1515 (1991).

[Cebr 89] D.A. Cebra, W. Benenson, Y. Chen, E.Kashy, A. Pradhan, A. VanderMolen, G.D. Westfall, W.K. Wilson, D.J. Morrissey, R.S. Tickle, R. Korteling, R.L. Helmer, Phys. Lett B **227**, 336 (1989).

[Ceci 79] R.A. Cecil, B.D. Anderson, and R. Madey, NIM **161**, 439 (1979). Note that the parameters published here, do not fit the data from [Verb 68].

[Chen 87] Z. Chen, C.K. Gelbke, W.G. Gong, Y.D. Kim, W.G. Lynch, M.R. Maier, J.Pochodzalla, M.B. Tsang, F. Saint-Laurent, D. Ardouin, H. Delagrange, H.Doubre, J. Kasagi, A. Kyanowski, A. Péghaire, J. Péter, E. Rosato, G. Bizard,F. Lefébvres, B. Tamain, J. Québert, and Y.P. Viyogi, Phys. Rev. C **36**, 2297(1987).

[Chit 85] C.B. Chitwood, J. Aichelin, D.H. Boal, G. Bertsch, D.J. Fields, C.K. Gelbke, W.G. Lynch, M.B. Tsang, J. C. Shillcock, T.C. Awes, R.L. Ferguson, F.E. Obenshain, F. Plasil, R.L. Robinson, and G.R. Young, Phys Rev. Lett. **54**, 302 (1985).

[Chit 86] C.B. Chitwood, C.K. Gelbke, J. Pochodzalla, Z. Chen, D.J. Fields, W.G. Lynch, R. Morse, M.B. Tang, D.H. Boal, and J.C. Shillcock, Phys. Lett. B **172**, 27 (1986).

[Colo 95] N. Colonna, D.R. Bowman, L. Celano, G. D'Erasmo, E.M. Fiore, A. Pantaleo, V. Paticchio, G. Tagiente, and S. Pratt, Phys. Rev. Lett. **75**, 4190 (1995).

[Cron 93] M. Cronqvist, Ö. Skeppstedt, M. Berg, L.Carlén, R. Elmér, R. Ghetti, J. Helgesson, B. Jakobsson, B. Norén, A. Oskarsson, F. Merchez, D. Rebreyend, L. Westerberg, V. Avdeichikov, A. Bogdanov, O. Lozhkin, Yu. Murn, K. Nybø, E. Olberg and T.-F. Thorsteinsen, Phys. Letter B **317**, 505 (1993).

[DeYo 89] P.A. DeYoung, M.S. Cordon, Xiu qin Lu, R.L. McGrath, J. M. Alexander, D.M. de Castro Rizzo, and L.C. Vaz, Phys. Rev. C **39**, 128 (1989).

[DeYo 96] P.A. DeYoung, R. Bennink, T. Butler, W. Chung, C. Dykstra, G. Gilfoyle, J. Hinnefeld, M. Kaplan, J.J. Kolata, R.A. Kryger, J. Kugi, C. Mader, M. Nimchek, P. Santi, A. Snyder, Nuc Phys. A **597**, 127 (1996).

[Engl 74] J.B.A. England, *Techniques in Nuclear Structure Physics*, Halsted Press, New York (1974).

[Fox 88] D. Fox, D.A. Cebra, J. Karn, C. Parks, A. Pradhan, A. Vander Molen, J. van der Plicht, G.D. Westfall, W.K. Wilson, and R.S.Tickle, Phys. Rev. C **38**, 146 (1988).

[Frie 83] W.A. Friedman, W.G. Lynch Phys. Rev. C **28**, 16 (1983).

[Frie 88] W.A. Friedman, Phys. Rev. Lett. **60**, 2125 (1988).

[Frie 83] W.A. Friedman, W.G. Lynch Phys. Rev. C **42**, 667 (1990).

[Gaff 95] S.J. Gaff, C.K. Gelbke, W. Bauer, F.C. Daffin, T. Glasmacher, E. Gualtieri, K. Haglin, D.O. Handzy, S. Hannuschke, M.J. Huang, G.J. Kunde, R. Lacey, W.G.Lynch, L. Martin, C.P. Montoya, R. Pak, S. Pratt, N. Stone, M.B. Tsang, A.M.Vander Molen, G.D. Westfall, and J. Yee, Phys. Rev. C **52**, 2782 (1995).

[GEAN 93] GEANT Manual, CERN Program Library Long Writeup W5013. Found at WWW site: http://wwwinfo.cern.ch/asdoc/geant_html3/geantall.html.

[Ghet 93] R. Ghetti, L. Carlén, M. Cronqvist, B. Jakobsson, F. Merchez, B. Norén, D. Rebreyend, M. Rydehell, Ö. Skeppstedt and L. Westerberg, NIM **335**, 156 (1993).

[Gold 59] G. Goldhaber, W.B. Fowler, S. Goldhaber, T.F. Hoang, T.E. Kalogeropolous, and W.M. Powell, Phys. Rev. Lett., **3**, 181 (1959).

[Gold 60] G. Goldhaber, S. Goldhaber, W. Lee, and A. Pais, Phys. Rev. **120**, 300 (1960).

[Gong 88] W.G. Gong, Y.D. Kim, G. Poggi, Z. Chen, C.K. Gelbke, W.G. Lynch, M.R.Maier, T. Murakami, M.B. Tsang, H.M. Xu, and K. Kwiatkowski, Nucl.Instrum. Methods **A268**, 190 (1988).

[Gong 90a] W.G. Gong, N. Carlin, C.K. Gelbke, and R. Dayton, Nucl. Instrum. Methods **A287**, 639 (1990).

[Gong 90b] W.G. Gong, W. Bauer, C.K. Gelbke, N. Carlin, R.T. de Souza, Y.D. Kim,W.G. Lynch, T. Murakami, G. Poggi, D. Sanderson, M.B. Tsang, H.M. Xu,S. Pratt, D.E. Fields, K. Kwiatkowski, R. Planeta, V.E. Viola, Jr., and S.J. Yennello, Phys. Rev. Lett. **65**, 2114 (1990).

[Gong 91a] W.G. Gong, W. Bauer, C.K. Gelbke, and S. Pratt, Phys. Rev. C **43**, 781 (1991).

[Gong 91b] W.G. Gong, C.K. Gelbke, W. Bauer, N. Carlin, R.T. de Souza, Y.D. Kim,W.G. Lynch, T. Murakami, G. Poggi, D.P. Sanderson, M.B. Tsang,

H.M.Xu, D.E. Fields, K. Kwiatkowski, R. Planeta, V.E. Viola, Jr., S.J. Yennello,and S. Pratt, Phys. Rev. C **43**, 1804 (1991).

[Gong 92] W.G. Gong, Y.D. Kim, and C.K. Gelbke, Phys. Rev. C **45**, 863 (1992).

[Gong 93] W.G. Gong, P. Danielewicz, C.K. Gelbke, N. Carlin, R.T. de Souza, Y.D.Kim, W.G. Lynch, T. Murakami, G. Poggi, M.B. Tsang, H.M. Xu, S. Pratt,K. Kwiatkowski, V.E. Viola, Jr., S.J. Yennello, and J.C. Shillcock, Phys.Rev. C **47**, R429 (1993)

[Goul 64] F.S. Goulding, D.A. Landis, J. Cerny, and R.H. Pehl, NIM **31**, 1 (1964).

[Hari 85] P. Hariharan, *Optical Interferometry*, Academic Press, 1985.

[Hanb 56] R. Hanbury Brown and R.Q. Twiss, Nature (London) **178**, 1046 (1956).

[Hand 95a] D.O. Handzy, S.J. Gaff, W. Bauer, F.C. Daffin, C.K. Gelbke, and G.J. Kunde, Phys. Rev. C **51**, 2237 (1995).

[Hand 95b] D.O. Handzy, W. Bauer, F.C. Daffin, S.J. Gaff, C.K. Gelbke, T. Glasmacher,E. Gualtieri, S. Hannuschke, M.J. Huang, G.J. Kunde, R. Lacey, T. Li, M.A.Lisa, W.J. Llope, W.G. Lynch, L. Martin, C.P. Montoya, R. Pak, G.F.Peaslee, S. Pratt, C. Schwarz, N. Stone, A.M. Vander Molen, G.D. Westfall,J. Yee, and S.J. Yennello, Phys. Rev. Lett. **75**, 2916 (1995).

[Hand 95c] D.O.Handzy, Ph.D. thesis, Michigan State University, 1995.

[Hind 84] D.J. Hinde, R.J. Charity, G.S. Foote, J.R. Leigh, J.O. Newton, S. Ogaza, and A. Chatterjee, Phys. Rev Lett. **52** 986 (1984); **53**, 2275 (1984).

[Hind 85] D.J. Hinde, R.J. Carity, G.S. Foote, J.R. Leigh, J.O. Newton, S. Ogaza, and A. Chatterjee, Nucl. Phys. A **452**, 550 (1986).

[Hube 90] F. Hubert, R. Bimbot, and H. Gauvin, Atomic Data and Nuclear Data Tables, **46**, 1 (1990).

[Hugh 58] D.J. Hughes and R.B. Schwartz, *Neutron Cross Sections*, Brookhaven National Laboratory, Upton, NY (1958).

[Jako 91] B. Jakobsson, B. Norén, A. Oskarsson, M. Westenius, M. Cronqvist, S. Mattson, M. Rydehell, Ö. Skeppstedt, J.C. Gondrand, B. Khelfaoui, S. Kox, F. Merchez, C. Perrin, D. Rebreyend, L. Westerberg and S. Pratt, Phys. Rev. C **44**, R1238 (1991).

[Kim 89] Y.D. Kim, M.B. Tsang, C.K. Gelbke, W.G. Lynch, N. Carlin, Z. Chen, R. Fox, W.G. Gong, T. Murakami, T.K. Nayak, R.M. Ronningen, H.M. Xu,

F. Zhu, W. Bauer, L.G. Sobotka, D. Stracener, D.G. Sarantites, Z. Majka, and V. Abnante, H. Griffin, Phys. Rev. Lett **63**, 494 (1989).

[Koon 77] S.E. Koonin, Phys.Lett. **70B**, 43 (1977).

[Kund 93] G.J. Kunde, J. Pochodzalla, E. Berdermann, B. Berthier, C. Cerruti, C.KGelbke, J. Hubele, P. Kreutz, S. Leray, R. Lucas, U. Lynen, U. Milkau, C.Ngo, C.H. Pinkenburg, G. Raciti, H. Sann, and W. Trautmann, Phys. Rev. Lett. **70**, 2545 (1993).

[Li 91a] B.A. Li and W. Bauer, Phys. Rev. C **44**, 450 (1991).

[Li 91b] B.A. Li, W. Bauer, and G.F. Bertsch, Phys. Rev. C **44**, 2095 (1991).

[Lisa 91] M.A. Lisa, W.G. Gong, C.K. Gelbke, and W.G. Lynch, Phys. Rev. C **44**, 2865 (1991).

[Lisa 93] M.A. Lisa, C.K. Gelbke, W. Bauer, P. Decowski, W.G. Gong, E. Gualtieri, S.Hannuschke, R. Lacey, T. Li, W.G. Lynch, C.M. Mader, G.F. Peaslee, T.Reposeur, A.M. Vander Molen, G.D. Westfall, J. Yee, and S.J. Yennello,Phys. Rev. Lett. **70**, 3709 (1993).

[Lisa 93c] M.A. Lisa, C.K. Gelbke, P. Decowski, W.G. Gong, E. Gualtieri, S. Hannuschke, R. Lacey, T. Li, W.G. Lynch, G.F. Peaslee, S. Pratt, T. Reposeur, A.M. VanderMolen, G.D. Westfall, J. Yee, and S.J. Yennello, Phys. Rev. Lett. **71**, 2863 (1993).

[Lisa 93b] M.A. Lisa, Ph.D. thesis, Michigan State University, 1993.

[Lisa 94] M.A. Lisa, W.G. Gong, C.K. Gelbke, N. Carlin, R.T. de Souza, Y.D. Kim, W.G. Lynch, T. Murakami, G. Poggi, M.B. Tsang, and H. M. Xu, K. Kwiatkowski, V.E. Viola, Jr., and S.J. Yennello, Phys. Rev. C **49**, 2788 (1994).

[Lync 82] W.G. Lynch, L.W. Richardson, M.B. Tsang, R.E. Ellis, C.K. Gelbke, and R.E. Warner, Phys. Lett. **108B**, 274 (1982).

[Lync 83] W.G. Lynch, C.B. Chitwood, M.B. Tsang, D.J. Fields, D.R. Klesch, C.K.Gelbke, G.R. Young, T.C. Awes, R.L. Ferguson, F.E. Obenshain, F. Plasil,R.L. Robinson, and A.D. Panagiotou, Phys. Rev. Lett. **51**, 1850 (1983).

[Morj 97] M. Morjean, M. Chevallier, C. Cohen, D. Dauvergne, J. Dural, J. Galin, F. Goldenbaum, D. Jacquet, R. Kirsch, E. Lienard, B. Lott, A. Peghaire, Y. Perier, J.C. Poizat, G. Prevot, J. Remillieux, D. Schmaus, M.Toulemonde, Preprint Ganil P97 21 (1997).

[Nato 86] J.B. Natowitz, S. Leray, R. Lucas, C. Ngô, E. Tomasi, and C. Volant, Zeitschrift Für Physik A **325**, 467 (1986).

[Naya 92] T.K. Nayak, T. Murakami, W.G. Lynch, K.Swartz, D.J. Fields, C.K. Gelbke, Y.D. Kim, J. Pochodzalla, M.B. Tsang, H.M. Xu, and F. Zhu, Phys. Rev. C **45**, 132 (1992).

[Paul 94] P. Paul, M. Thoennessen, Ann. Rev. Nucl. Part. Sci. **44**, 65 (1994).

[Poch 85a] J. Pochodzalla, W.A. Friedman, C.K. Gelbke, W.G. Lynch, M. Maier, D. Ardouin, H. Delagrange, H. Doubre, C. Gregoire, A. Kyanowski, W. Mittig, A. Peghaire, J. Peter, F. Saint-Laurent, Y.P. Viyogi, B. Zwieglinski, G. Bizard, F. Lefebvres, B. Tamain, and J. Quebert, Phys. Lett. B **161**, 256 (1985).

[Poch 85b] J. Pochodzalla, W.A. Friedman, C.K. Gelbke, W.G. Lynch, M. Maier, D. Ardouin, H. Delagrange, H. Doubre, C. Gregoire, A . Kyanowski, W. Mittig, A. Peghaire, J. Peter, F. Saint-Laurent, Y.P. Vivogi, B. Zwieglinski, G. Bizard, F. Lefebvres, B. Tamain, and J. Quebert, Phys. Rev. Lett. **55**, 177 (1985).

[Poch 86] J. Pochodzalla, C.B. Chitwood, D.J. Fields, C.K. Gelbke, W. G. Lynch, M.B. Tsang, D.H. Boal, and J.C. Shillcock, 1986, Phys. Lett. B **174**, 36.

[Prat 84] Scott Pratt, Phys. Rev. Lett. **53**, 1219 (1984).

[Prat 87] S. Pratt and M.B. Tsang, Phys. Rev. C **36**, 2390 (1987).

[Prat 96] Scott Pratt private communications.

[Reid 68] R.V. Reid, Jr., Ann. Phys. (N.Y.) **50**, 411 (1968).

[Remi 86] B.A. Remington, Ph.D. Thesis, Department of Physics and Astronomy, Michigan State University (1986).

[Schw 94] E. Schwinn, U. Jahnke, J.L. Charvet, B. Cramer, H. Doubre, J. Fréhaut, J. Galin, B. Gatty, D. Guerreau, G. Ingold, D. Jacquet, D.X. Jiang, B. Lott, M, Morjean, C. Magnago, Y. Patin, J. Pouthas, E. Piasecki, A. Sokolow, Nucl. Phys. A **568**, 169 (1994).

[Siwe 95] K. Siwek-Wilczynski, R.H.. Siemssen and H.W. Wilschut, Phys. Rev. C **51**, 2054 (1995).

[Stee 83] W.H. Steel, *Interferometry*, Cambrige University Press, Cambrige (1983). Especially section 14.3.1.

[Troc 87] Trockel, R., U. Lynen, J. Pochodzalla, W. Trautmann, N. Brummund, E. Eckert, R. Glasow, K.D. Hildenbrand, K.H. Kampert, W.F.J. Muller, D. Pelte, H.J. Rabe, H. Sann, R. Santo, H. Stelzer, and R. Wada, Phys. Rev. Lett. **59**, 2844 (1987).

[Verb 68] V.V. Verbinski, W.R. Burrus, T.A. Love, W. Zobel, and N.W. Hill, R. Textor, Nucl. Instrum. and Methods **65**, 8 (1968).

[Viol 82] V.E. Viola, Jr., B.B. Black, K.L. Wolf, T.C. Awes, C.K. Gelbke, H. Breuer. Phys. Rev. C **26**, 178 (1982).

[Wang 97] J. Wang, A. Galonsky, J.J. Kruse, P.D. Zecher, F. Deák, Á. Horváth, Á. Kiss, Z. Seres, K.Ieki, and Y. Iwata NIM (1997), in press.

[West 85] G.D. Westfall, J.E. Yurkon, J. van der Plicht,Z.M. Koenig, B.V. Jacak, R.Fox, G.M. Crawley, M.R. Maier, and B.E. Hasselquist,Nucl. Instrum. Methods **A238**, 347 (1985).

[Zajc 84] W.A. Zajc, J.A. Bistirlich, R.R. Bossingham, H.R. Bowman, C.W. Clawson, K.M. Crowe, K.A. Frankel, J.G. Ingersoll, J.M. Kurck, C.J. Martoff, D.L. Murphy, J.O. Rasmussen, J.P. Sullivan, E. Yoo, O. Hashimoto, M. Koike, W.J. McDonald, J.P. Miller and P. Truöl, Phys. Rev. C **29**, 2173 (1984).

[Zech 96] P.D. Zecher, Ph.D. thesis, Michigan State Unieveristy, 1996.

[Zech 97] P.D. Zecher, A. Galonsky, J.J. Kruse, S.J. Gaff, J. Ottarson, J. Wang, F. Deák, Á. Horváth, Á. Kiss, Z. Seres, K. Ieki, Y. Iwata, and H. Schelin NIM (1997), in press.

[Zhu 91] F.Zhu, W.G. Lynch, T. Murakami, C.K. Gelbke, Y.D. Kim, T.K. Nayak, R.J. Pelak, M.B. Tsang, H.M. Xu, W.G. Gong, W. Bauer, K. Kwiatkowski, R. Planta, S. Rose, V.E. Viola, Jr., L.W. Woo, S. Yennello, and J.Zang, Phys. Rev. C **44**, R582 (1991).